Quantum Transport Characterizations in Selective-Area Grown InGaAs Nanowire Networks

Inauguraldissertation

zur

Erlangung der Würde eines Doktors der Philosophie

vorgelegt der

Philosophisch-Naturwissenschaftlichen Fakultät

der Universität Basel

von

Kristopher Cerveny

Basel, 2022

Originaldokumentgespeichert auf dem Dokumentenserver der Universität Basel
edoc.unibas.ch

Genehmigt von der Philosophisch-Nanturwissenschaftlichen Fakultät
auf Antrag von

Prof. Dr. Dominik M. Zumbühl

Prof. Dr. Jelena Klinovaja

Prof. Dr. Thomas Schäpers

Basel, den 21.06.2022

Prof. Dr. Marcel Mayor
Dekan

In sterquiliniis invenitur

Abstract

Selective-area-grown (also referred to as 'templated') semiconductor nanostructures have generated considerable research interest in recent years as potential vehicles for the investigation of fundamental quantum phenomena as well as towards scalable networks for deployment in future quantum computers. Such structures made from III-V semiconductors, which can play host to effects such as strong spin-orbit interaction and Fermi-level pinning of the conduction band at the interface, are of interest due to the fast spin precession as well as being potential vehicles for realization of non-trivial topological states of matter.

This nascent technology has relied on the bridging of growth techniques, nano-fabrication, low-temperature electronic transport studies, and compositional analysis during its development. The required expertise involved has resulted in fruitful collaborations between a number of research groups in different institutions, which has enabled steady progress. Devices have been fabricated on quasi-1D nanostructures comprised of InGaAs nanowires grown atop defect-free GaAs nanomembranes, first with bulk-doping of Si^{+} donors in the InGaAs wires in order to demonstrate a proof-of-principle for the system.

Later, devices utilizing modulation doping strategies in order to reduce impurity scattering - while still providing the necessary additional carriers for transport - have been realized, measured, and analysed. Devices with branched geometries have been produced and quantum intereference effects have been observed across the junctions. Important transport parameters such as mean free paths, coherence lengths and spin-orbit lengths have been extracted in order to characterize the structures and motivate the next steps along the evolution of the systems. Novel fabrication techniques have been developed and employed in order to investigate and control various aspects of the structures, including carrier density and electric fields across the wires.

1 Acknowledgements

It is fitting that I should begin with the acknowlegements section, as this work has been made possible with the help and support of many people over these past years. They deserve a significant portion of the credit for the quality of work carried out and the results. I have had the massive fortune to have people around me on a daily basis who patiently correct my errors, are willing to listen to ideas, discuss concepts in the depths as well as at the surface of things, while rarely taking themselves so seriously as to not be able to enjoy and appreciate what incredible opportunities we have in carrying out this research. Many have also provided input and corrections to this thesis, for which I am eternally grateful. All remaining mistakes are mine.

I have benefitted from an outstanding working environment over the past years. **Prof. Dr. Dominik M. Zumbühl** deserves major credit for cultivating this. Without Dominik, this thesis would not have been possible. From the group meetings to the one-on-one meetings, there has always been an opportunity to both learn and enjoy some light-hearted humor. The traditional yearly (barring restaurant closures due to pandemics) Christmas dinner has been a continual highlight. The group hikes, soaking up the immense beauty of the Swiss Alps, trying (and failing) to keep up with a leader, who has roamed them since he was a child, and then exhaustedly cherishing a few drinks in a SAC Hütte have been a wonderful addition in the past couple of years. The memories that have been created through conferences, dinners, and the odd lab-beer or two will never be forgotten. Throughout the years, he has managed to find an excellent balance between being there for input and advice when needed, and allowing the freedom to explore ideas, designs and measurements without micromanagement. I want to express heartfelt appreciation and gratitude for the opportunity that has been afforded to me.

The outstanding working environment has been comprised of some notable individuals over the years. **Dr. Pirmin Weigele** deserves first mention. Pirmin put up with me as I was first learning to use laboratory equipment. That includes virtually every device in the building for fabrication and measurement. I benefitted significantly from his structured approach to things. Aside from what he was able to teach me on a scientific level, the time spent working together and the discussions we had were very enriching, as we both learned to deal with different approaches. **Dr. Taras Patlatiuk** has been a boundless font of knowledge and expertise. His patience in explaining and helping to solve problems serves as an excellent role model, one that I try to emulate. Our many conversations over the years have always been interesting and his thoughts

are always valued, no matter what the topic is. **Dr. Christian Scheller** has also been ever-present in this research group. Your child-like curiosity is admirable and it's a joy to see how much he enjoys figuring things out, building them, repairing them, and even sacrificing some blood in the process. He's made me think on many occasions and have been able to explain lots of physics in an intuitive manner. **Dr. Mohammad Samani**, who has now went back to Canada, is an incredible scientist, and a wonderful human being. I am lucky to have spent a couple years with him as an office mate. He was always happily willing to demonstrate to me where I was being an idiot. I learned a huge amount from him in terms of programming, approaches to troublshooting, remaining calm and kind in adversity, and in listening to alternative points of views and taking as much good from them as possible. I am very happy for him to receive the opportunity to go back to where he feels at home in Vancouver, while at the same time selfishly wish he was still around.

I would like to thank my collaborators at EPFL as well. **Prof. Dr. Anna Fontcuberta i Morral**, who leads the group, has been a bastion of positivity and energy over the years we have worked together. It has always been a pleasure to see her at the QSIT Arosa meetings, during her visits to Basel or mine to Lausanne, in Zoom/Skype calls, and at the occasional conference. The conversations over meals during such occasions are always interesting and engaging. I genuinely feel quite lucky to have had the opportunity to work with someone like her. **Dr. Martin Friedl**, who began growing samples for us some years ago, was also very enjoyable to work with and to achieve a number great results together scientifically. Outside of the realm of science, our discussions on health, fitness, philosophy, machine learning, and life were even more valuable. For the past few years now, **Didem Dede** has taken over the growth. It has been great to get to know her these past years. She has always been available to answer my questions about growth possibilities and to discuss what we would like to achieve together. The motivation she has and careful work she does is noticed and appreciated.

Prof. Dr. Jelena Klinovaja also deserves mention. I appreciate her willingness to agree to be my second advisor, despite the project not having much overlap with her research. The conversations we have had over the years have been enjoyable and engaging when we have had the opportunity to talk at the occasional barbeque or Christmas dinner.

Other, current members of our research group also deserve appreciation and thanks.
Miguel Carballido and I have been studying together since our bachelor studies. The large

amount of interesting conversations that we have had has contributed significantly to the quality of life I've enjoyed in the past years in this research environment. He always puts helping others before himself, and has been able to convey a constant sense of play alongside an excellent manner of explaining things. For every color I don't wear, he will wear three, and the times that I've tormented him with philosphy at the wrong moment are dear to my heart. **Henok Weldeyesus** has also been a fixture for most of my time as a Phd student. He deserves thanks for his help with measurement set up issues and for informing me when the ^{3}He mixture is having problems. This is not, however, what is great about Henok. The best part, in my humble opinion, is the conversations that we manage to hold almost daily during a (sometimes) brief coffee break which rapidly deteriorate into complete nonsense, remain in a chaotic state for a few moments, and then resurface again into order and/or humor. **Omid Sharifi**, my friend from Iran, is, perhaps, the kindest individual I have yet met. He is always happy to help others, is always digging into a subject to understand it as deeply as possible and is continously impressed by how incredible physics can be. His sense of awe with the concepts and dilligence in work serves as a role model for many others. Our cultural discussions and tea exchanges have been highlights for me. **Pierre Chevalier Kwon** has been a great officemate in the past couple of years. He never allows me to take myself too seriously, which has helped me to play with the world around me regularly. The conversations have been interesting, ranging from absolute nonsense to deep philosophical topics, often inside of seconds. The laughs we have at each other's expense provide true value to my life. It is unlikely that the next person I have as a desk-neighbor will be able to compare. **Simon Svab** is often staying out of the limelight, yet always paying attention waiting to snipe with some sharp joke. Many times he has caught one or more of us off guard with this subtle sense of humor and it is appreciated. He is also the only one who asks for my input on heavy grip trainers. **Rafael Eggli** has been an excellent addition to the team in the past year or so. He brings a combination of skill, intelligence and thoughtfulness to table that few are able to. Our conversations over an extensive array of topics have often made me think and dive deeper into. Finally, **Aldo Tarascio** is the newest addition to our team here. After getting to know us a few weeks he has fit in wonderfully, providing different perspectives and (sometimes odd) additional humor and artwork to our office.

Last, but certainly not least, **Evelyne Grüninger** has been an enormous source of support for many years. She has been there to listen at the end of the day, whether it was a successful

one or not, more times than I can count. She has served as a role model in many aspects for many years. I am extremely lucky to be sharing this journey with her. Having her as an integral part of my life is a blessing.

Contents

1 Acknowledgements **5**

2 Introduction **13**

2.1 On the Nature of the Endeavor 13

2.2 Thesis Outline 14

3 Reflections on Motivation **15**

4 On Dimension **18**

4.1 Energy Scales 18

4.2 Length Scales 20

4.3 Topology 22

5 Growth **26**

6 Quantum Interference Effects **33**

6.1 Scattering Basics 33

6.2 Dirty and Clean Regimes 36

6.3 Universal Conductance Fluctuations 38

6.4 Weak Localization Formalism 42

6.5 Spin-Orbit Interaction 43

6.6 Weak Anti-Localization 46

6.7 Weak Anti-Localization Formalism 50

7 Nanofabrication **52**

8 Template-Assisted Scalable Nanowire Networks **58**

8.1 System Introduction 59

8.2 Nanomembranes as a Platform 62

8.3 Electrical Transport in the Mesoscopic Regime 64

8.4 Conclusion and Outlook 68

8.5 Methods 68

8.5.1 Substrate Preparation 68

8.5.2 Growth 69
8.5.3 (S)TEM 69
8.5.4 Contacting 69
8.5.5 Quantum Transport Model 69
8.5.6 GaAs Capping 70
8.5.7 APT 70
8.6 Supporting Information 70
8.6.1 Growth Details 70
8.6.2 Temperature Dependence of InAs 71
8.6.3 Width/Pitch Dependence of InAs 71
8.6.4 Raman Spectroscopy 72
8.6.5 Strain Simulations 73
8.6.6 Growth Model 74
8.6.7 TEM Compositional Line Scan 78
8.6.8 InAs Crystal Quality 79
8.6.9 Magnetotransport Model 80

9 Remote Doping of Scalable Nanowire Branches 83

9.1 Abstract 84
9.2 Introduction 85
9.3 Growth 86
9.4 Atom-Probe Tomography 89
9.5 Magnetotransport 90
9.6 Conclusion 94
9.7 Experimental Section 94
9.8 Supporting Information 96
9.8.1 1D Finite Element Simulations of Remote-Doping 96
9.8.2 X-ray Fluorescence Mapping 97
9.8.3 Magnetoconductance Modeling 98
9.8.4 Additional Magnetoconductance Measurements 99
9.8.5 Description of Analysed Samples 101
9.8.6 APT Analysis of Multiple NWs from the Same Growth Chip 102

10 Outlook and Summary **105**

10.1 Controlling Rashba Spin-Orbit Interaction: Principle Idea 105

10.2 Controlling Rashba Spin-Orbit Interaction: Device Architecture 106

10.3 Controlling Rashba Spin-Orbit Interaction: Preliminary Measurements and Discussion 107

10.4 Additional Outlook and Summary 111

11 Fabrication Recipes **114**

11.1 Devices from Template-Assisted Scalable Nanowire Networks 114

11.1.1 Phase 1: PMMA 114

11.1.2 Phase 2: E-beam Lithography for contacts and Development 114

11.1.3 Phase 3: Reactive Ion Etching 115

11.1.4 Phase 4: Ammonium Polysulfide (NH_4S_x) Etching + Ti/Au (or Ti/Pd) Evaporation 115

11.1.5 Alternative Phase 4a: Argon Milling Etch + Ti/Pd Evaporation 116

11.1.6 Phase 5: Metal Lift-off 117

11.2 Devices from Remote Doping of Scalable Nanowire Branches 117

11.2.1 Phase 1: PMMA 117

11.2.2 Phase 2: E-beam Lithography for contacts and Development 118

11.2.3 Phase 3: Reactive Ion Etching 119

11.2.4 Phase 4: Ammonium Polysulfide (NH_4S_x) Etching + Ti/Au (or Ti/Pd) Evaporation 119

11.2.5 Phase 5: Metal Lift-off 120

11.2.6 Phase 6: ALD window of HfO_2 120

11.2.7 Phase 7: Spinning PMMA, Lithography, and Metallization of Wrap-Around Gates 121

11.3 Devices with Split-Gate Architecture 122

11.3.1 Phase 1: PMMA 122

11.3.2 Phase 2: E-beam Lithography for contacts and Development 122

11.3.3 Phase 3: Reactive Ion Etching 123

11.3.4 Phase 4: Ammonium Polysulfide (NH_4S_x) Etching + Ti/Au (or Ti/Pd) Evaporation 123

11.3.5 Phase 5: Metal Lift-off 124
11.3.6 Phase 6: ALD window of HfO_2 124
11.3.7 Phase 8: Spinning PMMA and Lithography of First Split Gate 125
11.3.8 Phase 9: Second ALD Window of HfO_2 126
11.3.9 Phase 10: Spinning PMMA and Lithography of Second Split Gate 127
11.4 Glueing into Chip Carrier and Gold Bonding 127

References **128**

12 Curriculum Vitae **155**

2 Introduction

2.1 On the Nature of the Endeavor

Written evidence of the exploration of knowlege dates back thousands of years, and one could reasonably assume that the pursuit thereof predates the enscription by many times this. The ancient Greeks are, perhaps, best known for formalizing this pursuit. Progenitors of western thought, they laid a foundation for the nature of knowledge. It was the Greeks who came up with the term *φιλοσοφία* (philosophy), meaning 'love of knowledge or wisdom.' Plato, one of the most renowned Greeks, presented an allegory of the cave [1]. In this cave, people were chained in such a way that they could only look straight ahead to a wall onto which a fire cast shadows. These shadows they studied, developing sophisticated theories and explanations. It was suggested that, if one of the people was freed from the chains and lead out of the cave and into daylight, at first he would be blinded, his eyes unable to take in all the light. Only slowly might his vision adjust to ascertain a much deeper reality around him. In fact, if, after exposure to the light, he were later lead back into the cave, he would first find it difficult to articulate the shadows once again. Plato was actually a nickname he used, derived from the adjective *πλατύς*, meaning 'broad'. It is considered by some to refer to his chest and broad shoulders, since he was also an accomplished wrestler [2], indicating that he spent his time not only in theory, but also in practice. And so it is that theory must be subjected to the proving ground of experimental verification.

There are fundamental requisites for success in the investigation of novel, complex endeavors. As the parameter space grows, one is increasingly reliant on the ability to humble oneself. Expertise in a network of technical aspects must be gathered and synthesized, after which one must continually move forward with incomplete knowledge. With a flicker of curiosity, one ventures deep into the caverns of the unknown, patiently illuminating the mostly vacant chambers with the hope of discovering some long hidden treasure. There are phantasms, which dance enticingly when the light happens to land with the appropriate angle and intensity, only to vanish when the torch is sufficiently bright. Aspects of the structure are vast and it is by no means always immediately obvious which are relevant. Pitfalls are abundant, where one may be led down a winding, faintly glowing, narrow passage, only to discover it was fool's gold at the end. Some of the explorers emerge finally with little to nothing other than worn-out instruments. Some resur-

face with what appears to be treasure, yet later is found to be a mirage [3][5]. Lucky are those who stumble upon uncharted territory with great riches and have the correct tools to excavate and then extract the gems. The majority toil away for a few years, can contribute to a map of the space to variable degree and depart the catacombs with a modest portion of the fortune. Those who truly profit from the whole endeavor tend to be the ones who recognize that the proper wealth accrued is the wisdom of the process, the discarding of the ego, and the careful balance between patience to detail and knowing when to move on. Science can be recognized as a modern branch of philosophy constrained under a particular method.

In his *Tao Te Ching* [6], Lao Tzu claimed that it was the empty space inside the cup that gave it value. This can be interpreted to mean that it is constraint that provides the framework for meaning. A four-year scientific investigation is, both, incomprehensibly long and incomprehensibly short. A doctoral study begins with a sophisticated plan involving many moving parts, assumptions, and aspirations. It was Moltke the Elder, who said "No plan of operations extends with certainty beyond the first encounter with the enemy's main strength", and Mike Tyson, who paraphrased this wisdom with elegance suitable for nanofabrication, saying "Everyone's got a plan until they get hit". Machines break down, tweezers fail at crucial moments, chemicals are contaminated, pumps lose reliability, wire bonders smash holes into samples, and pandemics occur. Despite all this, concrete progress is made. Techniques are developed, samples are created, measurements are carried out, data analysis is executed, discussions take place, knowledge is gained, and results are shared with the world. Of equal importance to these advancements, one learns a tremendous amount about oneself, forms relationships with unique individuals, collaborates with groups of people from around the world, and suffers all the while through personal growth.

2.2 Thesis Outline

The focus of this thesis is primarily the work done in low-temperature quantum transport experiments in order to electrically characterize the key transport properties of devices fabricated on novel nanostructures. Thus, after some motivational aspects, it will begin with an introduction to the physics of (quasi-) one-dimensional (1D) structures. Second, there will be a brief dive into the growth techniques required for the systems investigated. Third, there is a deeper dive into the relevant quantum interference effects. This is followed by a section on the fabrication

techniques developed for these novel structures. After these introductory sections, there are two chapters representing the published works over the course of this doctorate. Then, an outlook and summary, including work-in-progress on a dual-gated architecture and preliminary findings on such a device is presented. Throughout, a few light-hearted remarks are added into footnotes to provide additional levity to the work.

3 Reflections on Motivation

When it comes to motivation for scientific research, the first natural question is *why?* The question itself makes an assumption that doesn't always hold up, that assumption being that there is a single, straightforward answer to the query. One aspect of research that is often neglected is that, whatever one thinks their research is at the start, isn't actually what it turns out to be in the end. Although there are different degrees of acceptance of this point, it is an important one, as science is the *method* for investigation and discernment, not simply the attempt to achieve whatever it is that one thinks one wants. Karl Popper made a profound point that has remained valid through the years. He said that there are only two types of theories: Those which are known to not be true, and those which have not yet been demonstrated to be false [247]. The essence of this statement lies in an asymmetry in knowledge, which is sometimes called 'The Problem of Induction' or 'The Black Swan Problem'. Logically, no number of positive confirmations of a theory can completely confirm it, while a single (confirmed) counterexample is sufficient to disprove it. This is not to make light of the ambitions of any particular project, but rather to highlight the beauty in the fact that the curiosity in and investigation into the unknown, by its very nature, needs to accept resultant data for what it is. The great Richard Feynman put it succinctly when he said "The first principle is that you must not fool yourself... and you are the easiest person to fool" [20].

With this in mind, there are many ideas and aspirations that motivate the development of novel semiconducting nanostructures. Perhaps the first topic that comes to mind for most is the lofty prospect of quantum computation. This concept has often been credited to Feynman back in 1982, [21] though had originally been presented in one form by Paul Benioff in 1980 [22]. Algorithms quickly followed, suggesting great utility in the concept [44][45][46][52]. Essentially, the idea is to leverage the properties of quantum systems, such as superposition and entanglement, in order to perform calculations. The enticing prospect of quantum computing is its predicted

ability to perform certain types of calculations much faster than the conventional (classical) computer [23]. Some of the applications forseen for a quantum computer are factorization of large integers [24][35], finding a specific item from a list of n items (so-called search problems) [25], simulation of quantum systems [26], machine learning [27], and helping with drug design [28][29]. With myriad reasons for the development of quantum computation, the next question becomes *how* [80]? If we consider for a moment that a classical computer is built upon an architecture of bits - essentially a transistor that can be in the on or off state (allowing for current to flow or not) mapping to a 0 or a 1 - then a quantum version of a computer could be made up of *qubits*, i.e. quantum bits. With qubits, the standard idea is to leverage a two-level system comprised of the states $|1\rangle$ and $|0\rangle$ (assumed to be eigenstates of the Pauli operator σ_z separated by an energy Δ from a continuum of states) which can, both, oscillate in a controlled manner between them as well as exist in a superposition of the two.

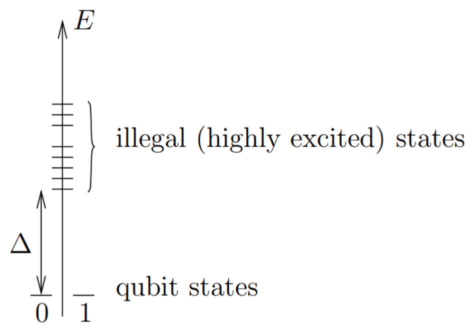

Figure 1: Spectrum of a physical qubit system with two accessible degenerate states, a gap Δ, and an unreachable continuum of higher energy states [48].

It is arguable whether or not the current quantum computers that exist are useful for practical matters, as they do not yet have large numbers of qubits, though concrete progress has been continually made [30][31][32][33][34]. There are many ways to create a two-level system and people argue over the merits of each of them. Nitrogen vacancy centers [36], trapped ions [37][38], superconducting circuits [39][40][41][42], spins in quantum dots [43][47], and (predicted) topological quasi-particles [48][49][50][51] each could serve as qubits and are active areas of interest.

Speed, reliability and scalability trade-offs exist amongst the various avenues for creating and controlling such a two-level system. Qubits rely on the coherence of the quantum state and there are three main timescales which need to be considered when assessing a qubit's viability. First, the relaxation time T_1 describes the transition from the excited state $|1\rangle$ to the ground state $|0\rangle$ due to interactions with the immediate environment. Second, the decoherence time

T_2 accounts for the decay of quantum mechanical superpositions and transitions of the sort $|1\rangle + |0\rangle \rightarrow \{|1\rangle, |0\rangle\}$. Third, one has the dephasing time T_2^*, which comes from the fact that it is typically required to measure over an ensemble, rather than a single system alone. T_2^* tends to decay faster than T_2 due to small deviations in oscillation frequencies from measurement to measurement that lead to destructive interference. In practice, T_1 tends to be much greater than T_2, thus decoherence is frequently the important parameter in a system when considering its viability [43].

It has been predicted that topological qubits would have particularly long coherence times and low-dimensional semiconducting structures with strong spin-orbit interaction under certain conditions could realize them [248]. On this topic, more to come. Suffice to say, the potential for novel nanostructures like those investigated over the course of this work to be stepping stones to topological qubits in the future is one major motivating factor. Adding to the promise of developing a system that might serve as a future building block for such a topological qubit is the scalability of this system. Any technology, in order for actual adoption, needs some reasonable form of scaling. A perfectly obvious point that can sometimes be neglected is that many processes and systems investigated in experimental science have no hope of scaling given current technological limitations.

This is not to say that there isn't merit in investigating non-scalable systems. On the contrary, one can learn a great deal from prototype systems in order to later implement them in similar - but more scalable - ways. On top of the remarkable ability humans have to adapt and swap implementation in such a way, many prototype systems also serve to answer questions about fundamental physical phenomena. The templated nature of the system we have been developing would eventually be able to be mass produced, which is a clear advantage over systems which can only serve as prototypes. Additionally, the process of creating these templated structures is free of gold catalysts, and could thus be more easily integrated into conventional silicon production lines, which is also attractive from the perspective of scalability and adoption.

As already mentioned, curiosity in a novel system is an important additional motivation. The growth technique employed in this work enables an enormous amount of possibilities for investigating theory and, potentially, discovering new physical phenomena. The prospect of building and exploring on-demand systems with different geometries and material stacks is enticing.

4 On Dimension

The concept of dimensionality is something that depends on perspective. Benoit Mandelbrot provided the world with, arguably, the most impressive investigation of dimension [7]. An object such as a common straw can serve as an example. From far enough away and with a particular resolution, it will appear as a zero-dimensional point. Zoom in a bit, and one has what looks like a one-dimensional line. Zooming in further, one notices that the structure seems three dimensional. Now, depending on the angle, approaching the object closer might make it appear as a 2D annulus. Coming even closer, the topography of the material will become clear and one would conclude again that it was, indeed, a 3D object. Zooming in even further to an atomic scale, one would then be confronted by the fact that this object was actually made up of atoms, appearing as a disjoint configuration of 1D points. It is with this in mind that we can conclude that the concept of dimension needs a fixed frame of reference to have meaning.

4.1 Energy Scales

In quantum transport we often talk about dimension in terms of energy scales where conduction or the signals of particular physics can occur. Our systems are investigated primarily under low temperatures. 'Low' means at liquid helium temperatures, i.e. around 4 K and below. One can easily calculate what is energetically forbidden via the relationship between energy and temperature. Using the Boltzmann constant, $k_B = 8.617 \times 10^{-5}$ eVK^{-1}, one can plug in the current temperature in degrees Kelvin to receive the energy in units of eV. Usefully, one has 87 μeV for 1 K. This serves as a straight-forward method for determining the physics that can be studied under particular temperatures. Many phenomena with energies below the system's thermal energy will tend to remain hidden. Systems which are adequately decoupled from their environment, such as a well-isolated double quantum dot, in contrast, can still showcase physics with smaller energy signatures than the temperature of the surrounding thermal bath. In order to measure electronic phenomena of extremely low energy scales in nanostructures, an enormous effort has been employed, resulting in measurements of record lows in electron temperatures in recent years [16][17][18].

A 3D 'bulk' conductor has no confinement on the charges, which can maneuver in any direction of the sample. For our purposes, this tends to be the least captivating case. Things begin to become more interesting with confinement. What is meant by 'confinement' is really that, in

order for charge carriers to travel in a particular dimension (our confinement), it would need an energy at a scale not reachable in the system under the experimental conditions. This sort of confinement, where propagation in one dimension is energetically forbidden, results in what are called two-dimensional electron gases aka 2DEGs (for the sake of this thesis, we will limit our scope to electrons, though the arguments generally also hold in the case of holes being the charge carriers). These can be imagined as conducting sheets, typically found at or near an interface between two materials. The dispersion relation for 2DEGs can be expressed as

$$E_{2D}(\mathbf{k}) = E_{0,z} + \frac{\hbar^2}{2m}(k_x^2 + k_y^2), \tag{1}$$

where $E_{0,z}$ is a constant offset energy expressing the confinement in the z-plane and $\hbar = 5.482 \times 10^{-16}$ eVs the reduced Planck constant.

If the system under investigation is confined in an additional dimension, we speak of a one-dimensional conductor. This can be accomplished by creating a narrow channel in a 2DEG or via a nanowire. In this case, our dispersion relation yields

$$E_{1D}(\mathbf{k}) = E_{0,x} + E_{0,z} + \frac{\hbar^2 k_y^2}{2m}, \tag{2}$$

for propagation along the y-axis.

In the event that a system has confinement in all three spatial directions, we speak of a zero-dimensional system aka a quantum dot. In the field of quantum transport this is frequently accomplished by using carefully placed capacitors ('gates') above a 2DEG or a nanowire to electrostatically confine the conducting electrons into a tiny space, hence the term dot. Here, we are left with discreet energy levels, which can be expressed accordingly as

$$E_{0D} = E_{n,x} + E_{n,z} + E_{n,y} = E_n, \tag{3}$$

where n represents the discrete energy states of the system.

4.2 Length Scales

Augmenting the concept of dimensional confinement through energy scales, we have some important length scales that enable further contextual refinement. First, we have the mean free path l_e, which is the average distance a carrier travels before experiencing a scattering event. The mean free path is also sometimes called the elastic scattering length. The size of l_e in a particular system will play a significant role in determining the phenomena present and measurable. Also of relevance is the phase coherence length l_φ, which is the average length a carrier travels before undergoing enough scattering events which transfer energy such that the quantum mechanical phase is randomized. l_φ is also called the inelastic scattering length. As long as energy is not exchanged during a scattering event, the phase coherence is conserved, which can manifest in a variety of phenomena. Importantly, in the systems studied here, l_φ tends to be much longer than l_e, meaning there can be many elastic scattering events before an inelastic scattering. The spin-orbit length l_{so} is another important parameter in semiconductor systems hosting spin-orbit interaction. l_{so} is the typical length an electron travels before its spin begins to significantly precess, often defined to be 1 radian. It is inversely proportional to the spin-orbit energy of the system E_{so}, such that a shorter l_{so} corresponds to a stronger spin-orbit interaction. The interplay between l_φ and l_{so} will be discussed in more depth in a section dedicated to spin-orbit interaction.

When considering a narrow conducting channel, such as a nanowire, so-called *semiclassical* approaches can typically be made. The Drude conductivity is a well-known semiclassical result [19]. It takes the quantum mechanical Fermi-Dirac statistics into account, while assuming the dynamics of the conduction electrons around the Fermi level remain classical. Despite the remarkable utility of this theory in many cases, at low temperatures corrections are needed which take l_e, l_φ, and l_{so} into account, which we will see later. A system is considered diffusive when l_e is much smaller than the width and length of the conducting channel.

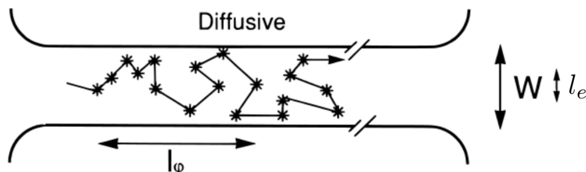

Figure 2: Schematic of a diffusive conducting channel of width W, with $l_e \ll W$ and $l_\varphi \lesssim W$. Asterisks denote scattering events. Graphic adapted from [8].

If, however, the mean free path of the system increases to larger than the width of the channel, though still remaining shorter than the length of the channel, one arrives at a so-called quasi-ballistic regime. Further elaboration on the quasi-ballistic regime will follow.

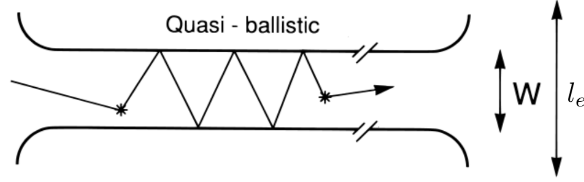

Figure 3: Schematic of a quasi-ballistic conducting channel of width W and length L, with $L > l_e > W$. Asterisks denote scattering events. Graphic adapted from [8].

With a mean free path larger than, both, the width and the length of the channel, one arrives in the ballistic regime. The ballistic regime is required to see purely quantum behavior such as quantized conduction. In many ways, systems in the ballistic regime play host to the most interesting and beautiful physics in the field of quantum transport. In the development of many systems, achieving this regime is a major milestone and highly challenging from a materials science as well as a fabrication standpoint.

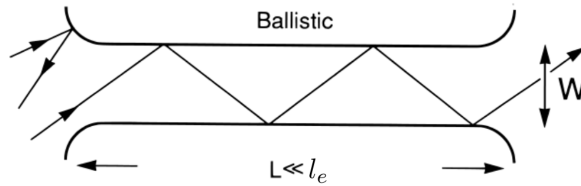

Figure 4: Schematic of a ballistic conducting channel of width W and length L, with $l_e(l) \gg W, L$. Graphic adapted from [8].

The systems investigated over the course of this doctorate fall into the category that has been coined 'quasi-one-dimensional'. The use of 'quasi' in this case suggests that the systems are not 1D (ballistic) in the sense that was previously mentioned. When we say quasi-1D, we mean systems in which the coherence length is larger than the width across the conducting channel, while the mean free path remains shorter than the channel length. One further criterion is that the Fermi wavelength, $\lambda_F = \frac{\hbar}{m^* v_F}$ (where m^* is the effective mass of the charge carriers and v_F is the Fermi velocity), remains much smaller than the channel width W. This results in diffusive systems, where there are many modes contributing to transport that scatter repeatedly along their paths between the source and drain of a sample. Despite the repeated scattering, the system can maintain a phase coherence over larger lengths under certain conditions. When

$l_e \ll W$, one falls into that which is often called the 'dirty metal' regime. This label is sometimes dropped in favor of using the perhaps-less-precise 'diffusive' regime to avoid a potentially negative connotation[1].

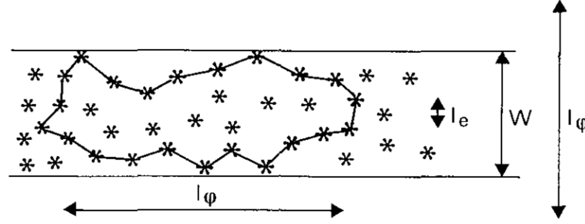

Figure 5: Schematic of a quasi-1D channel in the dirty limit of width W, with $l_e \ll W$ and $l_\varphi > W$. Asterisks denote scattering events. Graphic adapted from [9].

One can differentiate yet further to the case where l_e is comparable to the width of the channel and $l_\varphi \gg W$. This is a particular case of the quasi-ballistic regime, sometimes also called the 'clean' limit when dealing with quantum interference effects. This scenario requires, additionally, considerations about the type of scattering that the charge carriers undergo on the boundaries of the channel.

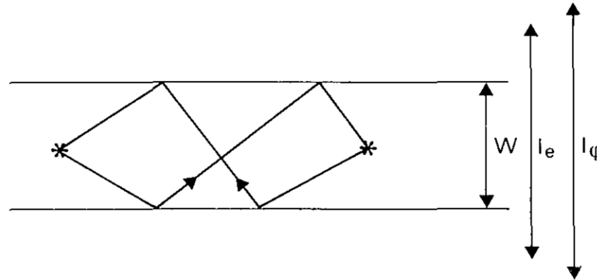

Figure 6: Schematic of a quasi-1D channel in the clean limit of width W, with $l_e \sim W$ and $l_\varphi > W$. Asterisks denote scattering events. Graphic adapted from [9].

The relevant quantum interference effects will be discussed in greater length in their own section.

4.3 Topology

Here, with an understanding of what we mean with dimension, we will return to the lofty idea of topological quantum computation. First, however, we need to define topology in our context. Essentially, the topology of a system can be thought of as what global properties it will maintain when it undergoes smooth, local deformations. A donut, or any torus, when undergoing

[1]The term 'dirty' could be embraced, however, as appropriate for the roll-your-sleeves-up work ethic necessary in the fabrication of these systems, and as a nod to the merit and virtue of accomplishing the grimy tasks in life that must be done. You tend to find what you most need to know where you least want to look.

sufficiently smooth, local deformity, can be molded into the form of a mug, and vice versa[2]. The topology remains conserved as long as it remains a genus one manifold; in common parlance, a structure with a single hole.

Figure 7: A mug smoothly deformed into the shape of a donut, illustrating their topological equivalence [249].

If quantum information could be encoded into the topological properties of a system, then the system would theoretically be highly robust against the serious problem of decoherence. Typically, decoherence is driven by small, local perturbations such as stray magnetic fields and electrostatic noise from nearby metallic gates. If the information was embedded in a topological state of matter, then only phenomena with energies larger than the topological gap could pose problems. Therefore, a topological qubit - a qubit where the degenerate ground state was dependent on the topology of the quantum mechanical system that it was embedded in - is desirable as this could offer a physical protection of the degeneracy. These aim to employ anyons, exotic quasiparticles which generalize the well-known statistics of fermions and bosons (hence *any*on). The interesting property of an anyon for these purposes is that the global wavefunction should acquire an arbitrary phase factor (as opposed to the restriction of bosons and fermions to being 0 and π, respectively) upon exchange of two or more of them, which is known as *braiding* [49]. This can be repesented in the form of a unitary matrix. Exchanges of these particles are non-Abelian, meaning that the order of exchange plays a role in determining the phase factor. Unlike operations with numbers, which are Abelian (or commutative), exchanges of anyons are akin to matrix multiplication, which is not generally Abelian. Another way one might think of this is that exchanges with these quasiparticles are path dependent.

Such quasiparticles could only exist in lower-dimensional systems. This has to do with the ability to smoothly deform a path of two identical particles. In three dimensions, one could always deform on path around the other without issue. This suggests that only bosons and fermions are able to exist as point particles, and exchanging them yields the well-known $+1$ and

[2]The author, a donut aficionado, finds topology extra exciting due to the near-certainty of allusions to donuts in all discussions and presentations surrounding it.

-1 phases. The wave functions are, therefore, required to satisfy

$$|\Psi_{3D}(\lambda_1)\rangle = |\Psi_{3D}(\lambda_2)\rangle = |\Psi_{3D}(0)\rangle \,, \tag{4}$$

where Ψ represents the wave functions and λ_i represent the paths for each particle. This also necessarily gives, upon circling another particle twice, $|\Psi_{3D}(\lambda_1)\rangle = \mathbf{R}_{3D}^2 |\Psi_{3D}(0)\rangle$, which, since the circular path can be contracted to a point, also yields $\mathbf{R}_{3D}^2 = 1$. This recovers the bosonic and fermionic statistics where $\mathbf{R}_{3D} = \pm 1$

By dropping down to two dimensions, one can already see that this is not possible and this hints at the different topology in the exchange of particles in three versus two (or fewer) dimensions.

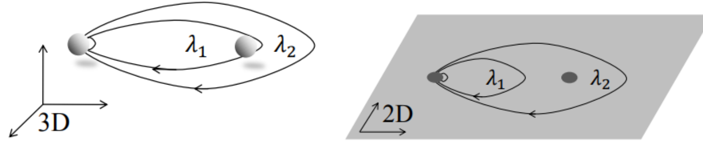

Figure 8: Exchange of two particles in 3D versus 2D [51]. In 3D the path of λ_2 can be smoothly lifted over that of λ_1 and contracted to a point, while in 2D, this evolution no longer remains a possibility.

Thus, in two dimensions, the initial state of the wave function isn't necessarily equivalent to the final state

$$|\Psi_{2D}(\lambda_2)\rangle \neq |\Psi_{2D}(\lambda_1)\rangle = |\Psi_{2D}(0)\rangle \,, \tag{5}$$

which results in squaring the exchange operator *not* needing to equal 1. This allows for the representation in a more general case as a complex phase or unitary matrix. Additionally, this implies that the order of the exhanges do matter, as the former strict requirement of $\mathbf{R}_{2D} = \mathbf{R}_{2D}^{-1}$ no longer holds. The remaining constraints on particle exchanges are derived from the mathematical braid group, from which the term 'braiding' received its moniker.

One major advantage of anyonic quantum computation would be a reduction in the quantum error correction architecture, which is the algorithmic means through which errors in quantum computation are treated [50]. A topologically-based quantum computer would be treating error correction, essentially, at the hardware level, providing strong resilience against perturbations

and control errors and, at the same time, making some complex quantum error correction schemes superfluous [51]. Alexei Kitaev was the first to realize that some quantum error surface codes could be considered akin to spin-lattice models, where the elementary excitations were anyons. The manipulation of these anyons would, then, be able to encode quantum states into the global properties of the system, rendering the local paths irrelevant. Topologically equivalent paths could then act as the same quantum gate. This insight is responsible for nudging a considerable portion of condensed matter research - material science, device engineering, and the accompanying theory - towards the investigation into anyonic particles in real systems.

Arguably the most sought-after anyon in the field of quantum transport is the Majorana fermion, often referred to as Majorana zero modes (MZM), or, simply, a Majorana. Such quasi-particles should be massless, chargeless, spinless, and should annihilate upon interaction with each other. They should always come in pairs, so each one corresponds in some sense to half of a fermion. It has been predicted that a p-wave superconductor with broken time-reversal symmetry should result in vortices, which could bind Majorana zero modes[252]. Some evidence for the existence of p-wave superconductors has been found in iron-based superconductors [253]. A method for synthesizing such a state was also proposed by Kitaev, where one leverages a 1D semiconductor with strong spin-orbit interaction, coupled to an s-wave superconductor in the presence of a magnetic field [255][270][271]. This proposal is helpful because we have ample evidence that all of these ingredients do exist. At the time of this writing, however, no topological qubit has been realized and no experiment has unambiguously demonstrated the existence of an anyon such as a Majorana fermion. Signatures of such particles have been measured [250][254], though considerable controversy exists around this subject [3][4][5][251].

In order to unambiguously demonstrate that the signatures are, indeed, what they are sometimes claimed to be, they must first be able to be braided. Without this, signatures consistent with Majoranas can arise from other, non-topological phenomena, such as disorder in the wire, Andreev bound states, or the Kondo effect [257]. We also can not rule out other currently unknown effects. Being as the recipe that Kitaev outlined requires 1D channels, when this is coupled to the fact that a Majorana should annihilate upon interaction with another one, it poses an additional challenge. Thus, in order for the possibility to braid, one needs a wire in a networked geometry, such as a X-, T-, or Y-shaped structure. In such a geometry, it could be possible to shuttle around two Majoranas using a sophisticated array of gates, without the two

interacting.

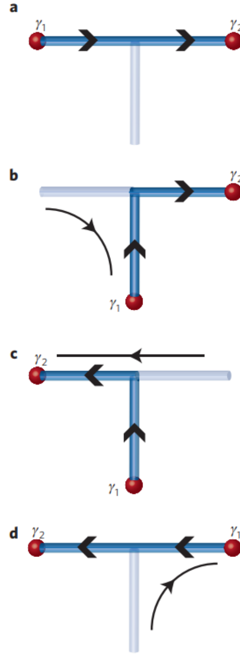

Figure 9: Schematic of a platform for braiding operations. Using the aforementioned technique for controlling and driving the MFs, one would have a platform for testing non-Abelian statistics. **a-d:** process to move γ_1 first down, enabling the movement of γ_2 across without annihilation, and then γ_1 back up and to the right, where $\gamma_{1,2}$ represent Majoranas [256].

Here, many gates would be employed to create, destroy and move the Majoranas around the device by tuning regions of the wire network into and out of the topological regime. This admittedly far-fetched idea adds additional emphasis to the ability to create networked architectures in selectively grown nanostructures and there has been a great deal of work done in researching various network architectures along these lines [258][259][260].

5 Growth

One of the motivations for this project is the development of novel nanostructures, created ('grown') inside the highly pristine environment of a molecular beam epitaxy chamber (MBE), which will be explained in detail in a following paragraph. For long-term viability of a process, a key element is scalability. A further desirable property is the ability to engineer the geometry of the structure. The two aspects of templating and scalability are central to the motivation for work carried out in this thesis. These have served as driving forces in the development of these promising new structures created with epitaxial growth.

Now, one might ask what is meant by epitaxial growth. *Epitaxy* has Greek roots: $\varepsilon\pi i$,

meaning ‘on top’, and $\tau\alpha\xi\eta\varsigma$, meaning ‘ordered arrangement’. So, epitaxial growth is the careful placement of ordered atomic layers on top of a substrate or crystal. This layer-by-layer placement is the reason that people in the field typically call it ‘growth’. Once atoms arrive at the surface of the sample, there are a number of processes which can occur. Adsorption occurs when the atoms reach the surface and attach themselves. Once on the surface, the atoms will typically be mobile and can diffuse around by an average distance and time determined by the conditions specific to the growth. The thermodynamics and kinetics regulating this diffusion will then determine the likelihood that an atom will add to step-like edge growth or form into a cluster. The desired processes for a particular growth will vary depending on what sort of structure is intended.

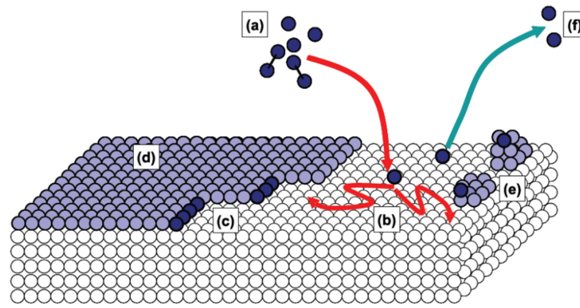

Figure 10: Schematic of epitaxial growth. (a-f) adsorption, diffusion, step-edge growth, atomic terraces, nucleation of clusters, desorption respectively. Graphic taken from [12].

An MBE is probably the most pristine environment that exists. It consists of a main chamber, which is under extremely high vacuum ($\sim$1 $\times$ 10^{-10} Torr), in which the temperature can - depending on the particular machine design - be set between -30 and 1850 °C [10][11]. This main chamber is where the growth takes place. In order to get the sample into the growth chamber, it is first placed into a load locked section of less high vacuum. After this, it is brought into a separate de-gassing chamber, where it is heated for between two and four hours, depending on the type of substrate, for the purpose of removing any contaminants that might be lying on the surface of the wafer. After degassing, it is then brought into the main chamber. Attached to the main chamber are a number of ultra-pure material sources. In the case of the work carried out in this thesis, the relevant materials are Galium (Ga), Arsenic (As), Indium (In) and Silicon (Si). The source materials are heated to temperatures where they undergo phase transitions to gas and can be released in a carefully controlled manner. The flux of the material released in this manner is modulated by the temperature that the particular source is heated to, with higher temperatures achieving a larger flux. The extremely high vacuum conditions of the growth

chamber result in the atoms of the material traveling in ballistic paths to the rotating sample, facillitating maximally uniform growth. Cooling cells line the walls of the growth chamber to prevent the rest of the MBE from heating up significantly during the growth processes. A beam flux monitor attached to a mechanical arm exists for the purpose of calibrating the material flux rates at various temperatures. This calibration is done typically every 3-4 months. An additional calibration tool, the reflectance high-energy electron diffraction (RHEED), which is more cumbersome and at the same time more accurate, is carried out once per year. This directly measures the monolayer growth rate by firing electrons towards the sample at a small angle which are collected on a phosphorescent screen on the opposite side of the chamber, allowing for visualisation.

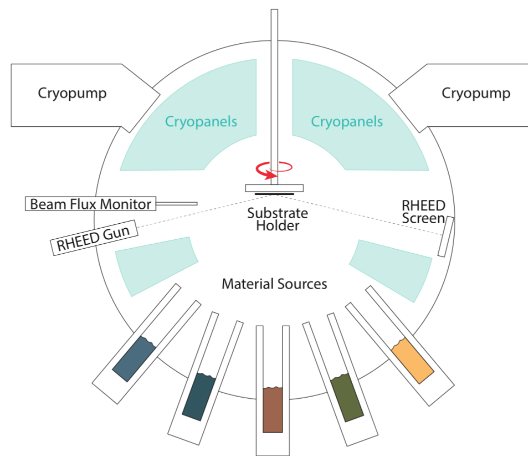

Figure 11: Schematic of a typical MBE growth chamber. Graphic taken from [13].

In order to achieve the novel structures which are investigated in this thesis, the epitaxial growth process must be carefully controlled. Since the work carried out over the course of this doctorate is focused on the electronic properties of the finished product, a very deep dive into the highly complex field of growth dynamics is outside the scope of this thesis. Still, a number of considerations ought to be expanded upon in order to provide a high-level understanding of the difficulties facing modern material scientists.

In epitaxial growth, which is a crystallization process, it is the thermodynamics of the incident adsorbing atoms onto the crystal that determine the specifics of the growth. The evolution of the growth is driven by minimizing the Gibbs free energy of the system. When the energy is able to be minimized, the system is said to be in thermodynamic equillibrium. In other words, the key is that the atoms will assemble into a particular solid structure when this is energetically favorable.

When the incident atoms are the same as the substrate, it is called homoepitaxy, which tends to be a simpler case. If, however, the incident atoms are of different species compared the the substrate, one speaks of heteroepitaxy, which can be considerably more challenging. One major reason for the additional difficulty in heteroepitaxy is the difference in the crystal lattice constant - the spacing between the atoms in the ideal crystal - in the different materials. The larger the lattice constant mismatch of different materials, the more strain imposed on the interface between them, and the more likely it becomes for defects to manifest.

Another consideration when approaching epitaxial growth is whether the desired structure is two- or three-dimensional. Moving from two to three dimensions increases the complexity of the problem significantly. The growth becomes a collection of dynamic, competing processes in three dimensions. The first important difference is the incident angle on each facet of the three-dimensional structure. The angle will determine the atomic flux impinging on the structure. In addition to this, now the mobility of the diffusion of adatoms between different facets must be taken into account. This will depend on the chemical potential variation between each facet as well as the facet-dependent lifetime of adatoms, those atoms adsorbed to the surface. This facet-dependent adatom lifetime is, effectively, the growth rate of each side of a structure. All of this is determined empirically, which can create a staggeringly large parameter space.

In most cases, there will be ranges in parameter space which yield the desired structures. However, the lives of growers have still more obstacles. Once a reasonably accurate parameter space range is discovered, one must contend with defects. The first driver of defects, lattice mismatch ϵ, has already been briefly mentioned. This is quantified as

$$\epsilon = \frac{a_d - a_s}{a_s}, \tag{6}$$

where a_d is the deposited material lattice constance and a_s is the substrate lattice constant. A larger ϵ results in more difficulty growing one material onto another without defects. In order to get an idea of the lattice mismatch between various materials, the following map is of use:

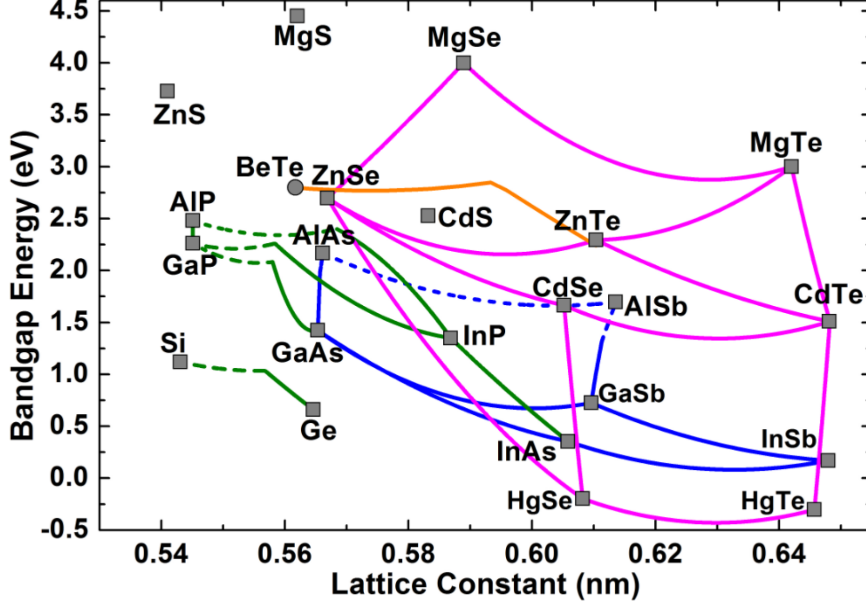

Figure 12: Lattice constants vs. band gaps of various semiconductor materials. Graphic taken from [14].

Lattice mismatches result in elastic and plastic deformations. Elastic deformations, on the one hand, occur when the material strains across the first few layers at the interface, gradually relaxing to the bulk spacing between atoms in the crystal lattice. This is typically the preferred interfacial deformation. Plastic deformations, on the other hand, result in a defect at the interface, often as a skipped atom.

The other main issue with regards to defects in MBE growth are so-called polarity mismatches. These occur, of course, exclusively in polar materials, such as III-V semiconductors used in our structures. In order to understand polarity mismatches, first we need to consider that in the case of a crystal of a III-V material, either the group III (type A) or the group V (type B) material will be on top. If there is a layer of growth merging from more than one site and these two sites have opposite polarities, there is a polarity mismatch, and an anti-phase boundary (APB) defect is created. The formation of APB defects can be significantly mitigated if the nanostructure is grown from a single nucleus.

Although in any real system there will always be defects, minimizing these is crucial in order to be able to fabricate devices which host the most interesting and exciting phenomena. In the field of quantum transport, where one can imagine electron carriers traversing a channel in a semiconductor material, each defect will act as a potential scattering center. The more scattering centers, the more chaotic the trajectories of the electrons become and the more diffusive their behavior turns. So, in order to investigate some of the purely quantum behaviors that electrons

can manifest, it is necessary to engineer the growth of nanostructures with as few defects as possible.

Not only is the creation of nanostructures with minimal defects highly desirable, the scalability is important for anything that could serve as a building block for useful technology. The ubiquity of semiconductors in the life of modern man requires no great introduction. According to the Semiconductor Industry Association [15], global semiconductor sales are currently around 500 billion USD per year and are projected to continue growing. Any nanostructure that would be integrated into an industrial scale must, therefore, be reproducible and scalable. This suggests that there is considerable interest in developing systems with scalable properties. The structures investigated and developed over the course of this thesis try to leverage this demand for scalability. Two later chapters, showcasing the published results, go into great depth on many of the technical details present in our system. Here, an additional brief explanation is given, in order to tie the previous ideas together.

The creation of the structures we have worked with begins with a GaAs wafer. The wafer is cleaned and tungsten alignment markers are initially placed to enable easier device fabrication. A SiO_2 mask is deposited on the surface. After this, an e-beam resist is spun, followed by lithography of a pattern executed on a wafer scale. Importantly, the design can be tailored to suit the needs of the device (with a few restrictions), and this can be easily changed as necessary. The pattern defines a network and array of channels. An etching procedure is then done to selectively remove the SiO_2 mask in the desired locations (the templated channels). Following this, some more cleaning is carried out, as the wafer is prepared to be placed into the MBE chamber. Below is a schematic of the process preparing the wafer for the membrane growth:

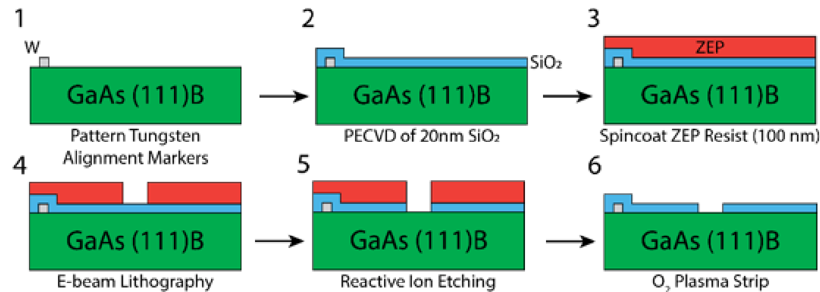

Figure 13: Six-step process to prepare the GaAs wafer for membrane growth. 1.) Cleaning and deposition of W alignment markers 2.) Deposition of SiO_2 mask 3.) Spinning of e-beam resist 4.) e-beam lithography 5.) Etching to selectively remove the SiO_2 6.) O_2 plasma stripping to remove resist traces.

The growth process is then initiated after degassing in the MBE and achieving the proper

vacuum conditions. The GaAs wafer acts as the nucleus for the growth of defect-free GaAs nanomembranes. As mentioned previously, the fact that a GaAs substrate serves as the nucleus for GaAs nanostructures results in considerably fewer APB defects.

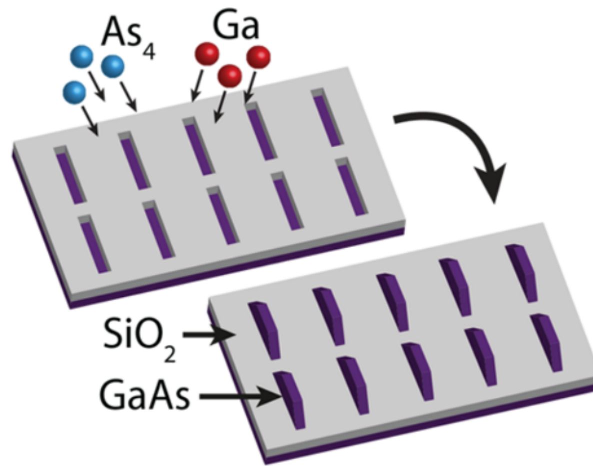

Figure 14: Schematic of a pre-patterned growth mask in the MBE growing GaAs nanomembranes [163].

After the membranes are grown, with the wafer still inside, the MBE conditions are changed to facillitate the growth of In(Ga)As nanowires on top of the GaAs membranes. The lattice mismatch between GaAs and In(Ga)As results in a strain, which drives growth of the In(Ga)As preferentially on the top of the membranes rather than on their side facets or on the SiO_2 mask.

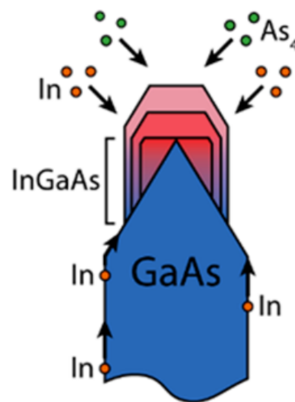

Figure 15: Schematic of a cross-section of an InGaAs nanowire grown on top of a GaAs nanomembrane [163].

Depending on the requirements, Si donor atoms can be integrated into the process during the nanowire or nanomembrane growth [108][163]. The different dopant strategies are explored in more detail in Chapter 8 and 9. In principle, the concept is flexible and multiple pathways for further evolution exist. Notably, there is the prospect of growing a second GaAs (or Al_2O_3) layer on top of the nanowire as an additional insulating barrier, followed by a second In(Ga)As wire

directly above the first. This could result in networks of parallel nanowires in close proximity, which could then serve as a platform to investigate exotic phenomena related to 1D-1D tunneling behavior [261][262][263][88][89].

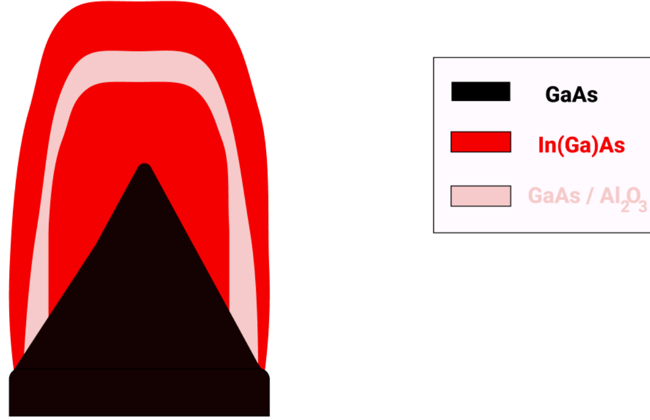

Figure 16: Schematic of a cross-section of a stacked pair of In(Ga)As nanowires, separated by a thin insulating layer of GaAs or Al_2O_3 grown on top of a GaAs nanomembrane.

6 Quantum Interference Effects

6.1 Scattering Basics

In order to understand quantum interference effects in diffusive systems, particularly in the systems investigated over the course of this work, a number of things must be considered. Central to this is the sort of scattering that the conduction electrons undergo. Additionally, the coherence length, l_φ, plays an imporant role. For the time being, spin-orbit interaction will be neglected in order to build up the concepts and only later will the role this plays be introduced.

Another manner, in which the phase coherence of the carriers can be considered, is through the phase coherence time, also called the inelastic scattering time τ_φ. Taking the quantum mechanical nature of our carriers into account, all possible paths through the system are realized via partial waves. We can consider the probability $P(\mathbf{r}, \mathbf{r}', t)$ of a particle to move from point $\mathbf{r}$ to $\mathbf{r}'$ in time t, which is the absolute value squared of the sum of probability amplitudes A_i [124]:

$$P(\mathbf{r}, \mathbf{r}', t) = \left| \sum_i A_i \right|^2 = \sum_i |A_i|^2 + \sum_{i = \neq j} A_i A_j^*. \tag{7}$$

The first part of right side of this equation is the classical diffusion probability, while the second

part accounts for quantum interference. Since in diffusive systems there are many scattering events occuring as the particles move in random walks through the channel, some of the paths will loop back around on themselves. One way to conceptualize this is to consider electrons moving on a slightly downhill trajectory from the source to the drain electrodes (i.e. the general direction of diffusion). Scattering centers are randomly distributed across this channel. Inside time τ_φ, when an electron scatters off of one of these, its momentum is randomized, while its energy - and, thus, phase - remains conserved. The looped trajectories are those where $\mathbf{r} = \mathbf{r}'$ and they remain correlated inside of τ_φ (i.e. $A^+ = A^- = A$).

Of all possible paths taken inside τ_φ, we need to pay especially close attention to those which arrive back at a point they have already visited. It will be seen that these paths, in particular, will account for quantum mechanical corrections to classical Drude conduction. Identical states occuring at the same location is forbidden generally by the Pauli principle. Therefore, as long as spin degeneracy is not broken somehow, a path and it's time-reversed partner are also forbidden. So, looped paths and their time-reversals result in increased back scattering. In other words, these paths constructively self-interfere and the result is an increasing resistance, or conversely, decreasing conduction. This coherent backscattering is what is called *weak localization* [95][3]. Here, we have

$$\left|A^+ + A^-\right|^2 = 4\left|A\right|^2, \tag{8}$$

which is twice the classical result. This is one case where there are macroscopically observable consequences of the quantum mechanical superposition principle. Now, only paths which can maintain their phase coherence across such loops can contribute to the coherent backscattering, so the area of these enclosed loops will be bounded above by an order of $\sim l_\varphi^2$. This takes the assumption that the motion between scattering events is ballistic and that the scattering events themselves are elastic in nature, meaning that they conserve energy and only randomize momenta. The approximate length between these scattering events is the mean free path, l_e. This can also be understood in terms of the elastic scattering time τ_e. Each scattering event will

[3]In weak localization, it is almost as if the carrier, upon traversing a loop and ending up where it began, has a *déjà vu* moment, resulting in a minor identity crisis. In this regard, Wolfgang Pauli may be considered as the first psychoanalyst specializing in spin $\frac{1}{2}$ particles. Carriers undergoing identity crises, it might be said, tend to contribute less to conduction.

occur with probability $\frac{dt}{d\tau_e}$ in the small time dt.

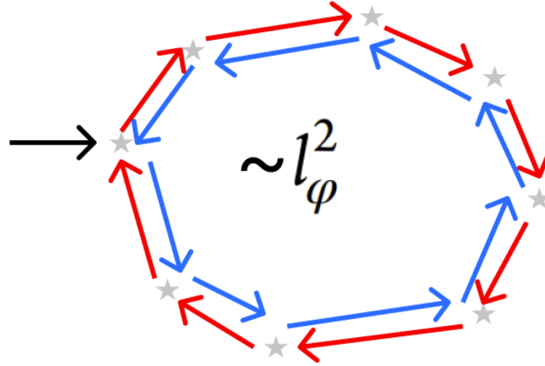

Figure 17: A carrier's path and its time reversal in a loop resulting in coherent backscattering. Grey stars indicate scattering events. Red and blue arrows are the time reversed paths. The enclosed loop has an area less than $\sim l_\varphi^2$

We note here that there is a more mathematically rigorous method for calculating the weak-localization correction to the conductance using the equilibrium Green's function theory, which allows for the treatment of dephasing and magnetic fields quantitatively. The mathematics of this are beyond the scope of this thesis, though we want to introduce two terms here from this formalism. The main corrections that come out of this can be expressed with two types of Feynman diagrams, namely diffusons and cooperons [269]. Diffusons, on the one hand, modify the diffusion constant, taking into account the angular dependence of scattering. Cooperons, on the other hand, account for the weak localization corrections themselves.

For the moment we will restrict our discussion to electron motion in a plane, such as in a 2DEG or a one-dimensional channel. Here, it is also worthwhile to briefly consider the nature of possible scatterings which determine τ_φ. There are two main contributors; that of electron-electron interactions, which have large energy transfers, and Nyquist scatterings, which contain small energy tranfers. The electron-electron contribution to dephasing rate can be written as [127]

$$\tau_{\varphi,e-e}^{-1} = \frac{\pi}{4}\frac{(k_BT)^2}{\hbar E_F}\ln\left(\frac{E_F}{k_BT}\right), \tag{9}$$

for $k_BT \ll E_F$. There is an intuitive argument for $\tau_{\varphi,e-e} \propto T^2$. Only electrons which are k_BT distance around the Fermi surface will contribute to transport. Then, an electron will scatter from one occupied state to an unoccupied state, thus a contribution propotional to $(k_BT)^2$.

Nyquist scattering causes phase breaking as a result of multiple quasi-elastic electron-electron scatterings and is expected to play a smaller role as the mean free path of particles grows larger. It is proportional to the dimension d of the sample as $\tau_{\varphi,N}^{-1} \propto T^{2/(4-d)}$ [128] and in a disordered 2DEG is given by [129]

$$\tau_{\varphi,N}^{-1} = \frac{k_B T}{2\pi\hbar} \frac{\lambda_F}{l_e} \ln\left(\frac{\pi l_e}{\lambda_F}\right). \tag{10}$$

At the end of the day, we are mostly concerned with the total scattering rate, which will be determined by the sum of these, $\tau_{\varphi}^{-1} \approx \tau_{\varphi,N}^{-1} + \tau_{\varphi,e-e}^{-1}$ [130][131]. Keeping in mind that we are doing measurements at low temperatures, we expect the dephasing rate to be mainly determined by the T^2 dependence of $\tau_{\varphi,e-e}^{-1}$

Since the coherent backscattering occurs as a result of the time-reversed paths being identical, one can explore what happens when this time-reversal symmetry is broken. Experimentally, this is typically accomplished via the use of a magnetic field. The application of a magnetic field results in the well-known cyclotron motion, which acts to destroy this weak localization effect. With the magnetic field B_z applied perpendicular to the plane of electronic motion, the phase coherence will be lost after the magnetic dephasing time $\tau_B \sim \frac{\hbar}{eB_z D}$, with $D = \frac{1}{d} v_F l_e$ being the diffusion constant in d dimensions. From the inverse proportionality of τ_B and B_z, we observe that a larger magnetic field causes this dephasing to occur quicker. This can be thought of as a shrinking of the area inside of which the trajectories can contribute to coherent backscattering in lock-step with increasing magnetic field. On the time scale τ_B, the flux $B_z D \tau_B \approx \frac{\hbar}{e}$ is enclosed, corresponding to a phase difference of order 1 between a path and its time reversal.

6.2 Dirty and Clean Regimes

Ultimately, τ_B depends on three lengths relative to each other: the magnetic length, $l_m = \sqrt{\frac{\hbar}{eB}}$, W, and l_e (considering the case where $l_\varphi > W$). As briefly mentioned previously, in the so-called dirty regime with $l_e \ll W \ll l_m$, the boundaries play a minimal role in the physics, only restricting diffusive motion in their respective directions. Therefore, one can modify this enclosed flux to $B_z W \sqrt{D\tau_{B,dirty}}$, where $\tau_{B,dirty} = \frac{l_m^4}{DW^2} = \frac{3\hbar^2}{(eB_z W)^2 D}$[95][97]. The enclosed flux on a given timescale is reduced due to the lateral compression of the backscattered trajectories. Here, the quantum mechanical phase difference between scatters (where carriers travel a distance $\sim l_e \ll l_\varphi$) is much smaller than 1, resulting in the total phase shift $\phi(t)$ having a Gaussian

distribution. This becomes clear if one considers the average of the phase factor over all closed classical trajectories, implying

$$\langle e^{i\phi(t)} \rangle = exp[-\frac{1}{2}\langle \phi^2(t) \rangle]. \tag{11}$$

When l_e begins to grow larger relative to the width W of the conducting channel, the boundary scatterings begin to become meaningful. Boundary scattering can be considered specular or diffusive. The type of which modifies τ_B by particular constants C_i, where i depends on the type of scattering, the applied magnetic field range, as well as whether the sample is in a thin film or narrow channel geometry. Up through the late 1980s, these were calculated from first principles and a few basic assumptions [95][125][126]. In reality, some systems likely have a combination of diffuse and specular scattering at the boundaries (such as the structures studied in this thesis), so, taking the exact value of any of these constants at face value in a particular analysis is best treated with caution. Fortunately enough, the constants don't tend to differ on their order of magnitude, so the results of using the theory for extracting values for l_φ and l_{so} are not markedly affected and the differences in the constants often fall roughly within the uncertainty of the fits[4]. When considering all of the mechanisms that go into the weak localization formalism in a forthcoming section, it becomes clear why these constants play a minor role in parameter extraction in the measured data. When l_e is large enough for boundary scattering to matter, the potential for flux cancellation occurs, reducing the total amount of backscattered paths.

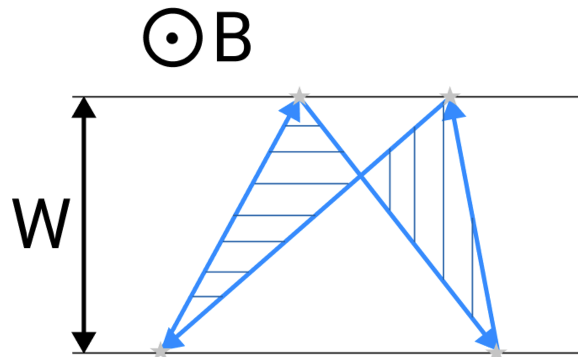

Figure 18: A closed electron path via boundary scattering resulting in flux cancellation when the two areas enclosed are exactly equal.

Samples where $l_e \gtrsim W$ are often referred to as 'pure metals', despite the fact that it is often semiconductors which are subjected to this treatment contemporarily. These can be broken down

[4]Here, the author would like to take the opportunity to express his sympathy with those who rigorously derived the constants, acts that were far from trivial.

into two regimes, depending on the magnetic field applied. For the first, pure metal in a weak field, one has $l_e \gg W$, $l_m \gg \sqrt{Wl_e}$. In this case, one gets $\tau_{B,clean,weak} = \frac{C_1 l_m^4}{W^3 v_F}$ [95]. Under this condition, the maximum phase increment between two scatters is still much less than 1, so the Gaussian approximation holds. The second regime, pure metal in a strong field, one still has $l_e \gg W$ but now $l_m \ll \sqrt{Wl_e}$. This yields $\tau_{B,clean,strong} = \frac{C_2 \tau_e l_m^2}{W^2}$. Here, phase changes of order unity can occur between collisions, which means that the Gaussian approximation no longer holds. For our purposes, it is sufficient to understand that a long derivation to calculate the average phase factor has been carried out and the result is valid. For a complete derivation see Appendix B in Beenakker and van Houten [95].

One might also point out that in real samples, the channel width W will typically have small spatial variations δ. Fortunately, these can be neglected in the weak field regime completely, as they will be approximately $(\frac{\delta}{W})^2$, thus, truly small perturbations. In the strong field regime, however, there is a larger correction, $(\frac{\delta}{W})^2 \frac{Wl_e}{l_m^2}$, meaning the fluctuations can only be neglected when $l_m = \sqrt{\frac{\hbar}{eB}} > W$ [95].

6.3 Universal Conductance Fluctuations

Another important phenomenon occuring in low-dimensional systems exhibiting quantum mechical behavior is that of UCF (universal conductance fluctuations)). These are sample-specific, repeatable deviations in conductance as a function of various system parameters. One can think of the particular impurity distribution of a many-mode conductor resulting in long-range correlations, which are superimposed onto the measured conductance. These result in a variance in conduction, often denoted by δG. They are usually not classically relevant (where we define 'classical' as $l_\varphi < l_e$), as δG will be smaller than the average conductance $\langle G \rangle$ by a factor of $\sqrt{\frac{l_e}{L}}$ [124]. Since l_φ is very small at high temperatures, UCF show up only at lower temperatures where the coherence length will be reduced less by phonons. The assumption underlying this is that the conducting channel can be broken down into $\frac{L}{l_e} \gg 1$ *independently* fluctuating segments, where quantum mechanical correlations manage to persist much longer than l_e. When $l_\varphi \sim L$, there will be significant sample-to-sample fluctuations. This was initially fleshed out by a number of theorists, finding that $\delta G \approx \frac{e^2}{h}$ at zero temperature [132][133][134] (thus, assuming l_φ to be infinite). This can be understood with a relatively simple argument. If we begin with

the well-known Drude conductivity for a single spin and valley,

$$G = \frac{W}{L}\frac{e^2}{h}\frac{k_F l_e}{2} = \frac{e^2 \pi l_e}{2hL} N, \tag{12}$$

where $N = \frac{k_F W}{\pi}$ is the number of transverse modes occupied at E_F in a conductor of width W. Current goes from the source (S) to the drain (D) electrodes and crosses a disordered region where only elastic scattering takes place. The two reservoirs are assumed to be in thermal equilibrium and to completely randomize the phase of the carriers via inelastic scattering. Thus, there is no phase coherence between the modes as they arrive at the disordered region.

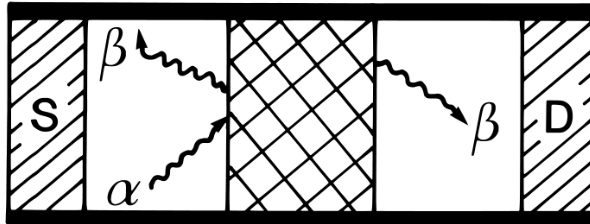

Figure 19: Schematic of a conducting channel with carriers traveling from source (S) to drain (D) traversing a disordered region. α represents incoming channels and β channels either backscattered or transmitted. Graphic taken from [124].

Each mode is a quantum channel and when $L \gg l_e$, each will have on average the same transmission probability $\frac{\pi l_e}{2L}$. If we take a look at the Landauer formula [135],

$$G = \frac{e^2}{h} \sum_{\alpha,\beta=1}^{N} |t_{\alpha\beta}|^2, \tag{13}$$

the ensemble averaged probability will be independent of α and β, requiring $\langle |t_{\alpha\beta}|^2 \rangle = \frac{\pi l_e}{2NL}$. Then, the magnitude of the conductance fluctuations will be determined by its variance Var(G) $\equiv \langle (G - \langle G \rangle)^2 \rangle$. This is, in general, difficult because different pairs of outgoing channels can not be ignored. A particular sequence of scattering events could be (and likely is) shared by many different channels due to the sample-specific impurity distribution. Reflectance probability $|r_{\alpha\beta}|^2$, however, can reasonably be assumed to be uncorrelated as long as reflection is dominated by a small amount of scattering events. In this case, utilizing the fact that the sum of all modes is simply those reflected plus those making it through, we can instead write $\sum_{\alpha,\beta=1}^{N} |t_{\alpha\beta}|^2 = N - \sum_{\alpha,\beta=1}^{N} |r_{\alpha\beta}|^2$, and we end up with Var(G) $\approx (\frac{e^2}{h})^2$, yielding a root-mean-square in the

conductance fluctuations $\delta G = \sqrt{\text{Var}(G)} = \frac{e^2}{h}$.

Here, one can be forgiven for pointing out that one is never measuring an actual sample at 0 K in temperature. This is important, because the assumption of $l_\varphi = \sqrt{D\tau_\varphi}$ being infinite is no longer valid, thus, the magnitude of δG is reduced by the thermal averaging manifest in a finite thermal length $l_T = \sqrt{\frac{hD}{k_B T}}$. For regimes where $l_\varphi \ll l_T$, the thermal averaging effects can be neglected. In the intermediate regimes it becomes of interest to compare τ_φ to $\frac{h}{k_B T}$. The interference effects due to weak localization and UCF differ from one another in this regard. Weak localization only depends on temperature through $\tau_\varphi(T)$ and does not suffer from this thermal averaging. This is a result of differences between diffusons and cooperons. Diffusons consist of paths with many different lengths that get averaged, which will smear with temperature. Cooperons, however, are paths which return to their point of origin, so the forward and backward paths necessarily have the same length and will not thermally smear. One further fact of note is that UCF should have a cut-off field B_{cut}, where the cyclotron orbit $r_c = \frac{m^* v}{eB}$ becomes smaller than l_e and W [136]. At applied magnetic fields larger than B_{cut} one would expect to no longer see this effect. It is at this point where we can notice that there should be a relationship between UCF, the coherence length, and the thermal length of a particular system. We will return to this consideration soon.

Experimentally, UCF can be studied by means of changing system parameters such as E_F and B sufficiently [132], or by modulating the confinement potential via the use of electrostatic gates. A large enough change in one of these is equivalent to changing the impurity distribution of the system. This essentially means that one can use experimental knobs such as an applied magnetic field, an increased source-drain bias, or electrostatic gating to measure different members of the ensemble inside the same sample. The conduction $G(E_F + \Delta E_F)$ and/or $G(B + \Delta B)$ is uncorrelated with $G(E_F)$ and/or $G(B)$ if $\Delta E_F/\Delta B$ are larger than a correlation energy E_c or field B_c. The correlation energy can be defined as $E_c \approx \frac{\hbar\pi^2 D}{L^2}$, which roughly corresponds to the inverse time it takes for a particle to diffuse across the sample in the direction of current [134]. The correlation energy and field can be obtained experimentally through the use of an autocorrelation function, which is a measure for the correlation between points in an ordered list. It is often written (in the case of the correlation field) $F(\Delta B) = \langle \delta G(B + \Delta B)\delta G(B)\rangle$. Here the brackets indicate taking an ensemble average. In our case, it will be a correlation measure, for example, of $\delta G(B_i)$ with $\delta G(B_{i+1})$, $\delta G(B_{i+2})$,..., $\delta G(B_{i+n})$, where $\delta G(B)$ is the conduction at a

particular value of magnetic field after subtracting a background. One defines the correlation of $\delta G(B_i)$ with itself as 1 and expects to see the correlation move towards 0 (meaning completely uncorrelated) after sufficiently many steps. One then defines B_c via the magnetic field value when taking the full-width at half-maximum, $F(B_c) = \frac{1}{2}(F(0))$.

With the knowledge that one can obtain a correlation field B_c in a particular sample, we return to the relationship between UCF and the coherence length. At a given temperature, the coherence length can be related to the correlation field as [138][139]

$$l_\varphi = \frac{\Phi_0}{B_c W}\gamma = \frac{h}{eB_c W}\gamma, \tag{14}$$

where γ is a constant that depends on the regime studied. $\gamma \approx 0.95$ in the dirty metal regime and, for cases where $l_e > W$, is modified slightly to $\gamma = 0.95\frac{l_e}{W}$. It is worth pointing out here that this was originally derived for a 1D channel geometry and may lose some accuracy in nanowires where there is three-dimensional diffusive motion. In practice, however, the coherence length obtained in such a manner has agreed well with those obtained from other means [139][140][141]. Here, we have a method for directly determining l_φ, though it may potentially be limited by the channel length, so it will tend to give a lower bound. If one has access to B_c at different temperatures, it is also possible to use this result to calculate the theoretically expected values for the root-mean-square of the conductance fluctuations δG_{rms} [138]:

$$\delta G_{rms} = K\frac{e^2}{h}\left(\frac{l_\varphi}{L}\right)^{3/2}\left[1 + \frac{9}{2\pi}\left(\frac{l_\varphi}{l_T}\right)^2\right]^{-1/2}, \tag{15}$$

where K is a constant depending on a number of system parameters that can be extracted empirically from fits to data. Determination of δG is important because UCF can and do mask the signals of other quantum interference effects such as weak localization and antilocalization. The correlation between conductance fluctuations should vanish when a change in E_F exceeds E_c. This can be accomplished, for example, by electrostatic gating or applying a source-drain voltage. When $l_\varphi < L$, E_c can by determined via the relationship [134]:

$$E_c \approx \frac{\hbar D}{l_\varphi^2}. \tag{16}$$

With this determined one can then average the data over a larger window[139][274] and then subtract this as a background. Over a large enough averaging window this should suppress the conductance fluctuations, leaving the signatures of weak (anti)localization in tact.

It has been theoretically predicted that the coherence length of electrons traveling in a quasi-1D channel should follow $l_\varphi \propto T^{-1/3}$ [142], as long as the assumption holds that quasi-elastic scatterings with small energy transfers dominate. This follows directly from the relationship $l_\varphi = \sqrt{D\tau_\varphi}$, with $\tau_\varphi \propto T^{-2/3}$. There are, however, some experiments in nanowires which have demonstrated deviations from this temperature dependence, as well as a saturation of l_φ below a threshold of ~1 K [123][139][143]. Another knob that one has experimental access to is often the application of a gate voltage V_g in order to tune the density of the carriers in a nanowire. It has been predicted that the coherence length should change linearly with the applied gate voltage due to a decrease in electron-electron scattering rate with increasing Fermi energy [144], and this has also been experimentally demonstrated [139].

6.4 Weak Localization Formalism

The devices studied in this thesis are considered quasi-1D. When the mean free path of a sample is sufficiently small (i.e. in the dirty metal regime), the weak localization correction $\Delta G(B)$ to the conductance can be well expressed using the formalism for a 1D channel geometry according to the Al'tsuler-Aronov theory [137][111]:

$$\Delta G(B) = \frac{-2e^2}{\pi\hbar}\frac{D}{L}\int_0^\infty dt C(t) e^{-t/\tau_\varphi} e^{-t/\tau_B}, \tag{17}$$

where $C(t)$ is the return probability for an electron in time t. Here, we see that the exponential terms with the dephasing times τ_φ and τ_B set thresholds for the degree that ΔG will be decreased due to the constructive interference of weak localization. They assume that electron momenta are randomized elastically by disorder/impurities in the sample. This formalism is a means to account for the fact that the quantum return probability to a given starting point after a particular time t differs from the classical return probability because of quantum interference. From this it follows that the quantum correction to the classical conduction will be a time integral over the quantum mechanical return probability $C(t)$ [145]. The various dephasing times τ_i can

also be generally expressed in terms of lengths l_i via the expression $l_i = \sqrt{D\tau_i}$. This previous integral can be solved and yields

$$\Delta G(B) = \frac{-e^2}{\pi\hbar}\frac{\sqrt{D}}{L}\left(\frac{1}{\tau_\varphi}+\frac{1}{\tau_B}\right)^{-1/2}. \tag{18}$$

In situations where the mean free path becomes comparable or larger than the width of the channel, the aforementioned flux cancellation due to boundary scattering must be taken into account as well. This is, essentially, a reduction in the effective area of the wire. If one takes this as well as short time correlations into account, one instead has [95]

$$\Delta G(B) = \frac{-e^2}{\pi\hbar}\frac{\sqrt{D}}{L}\left[\left(\frac{1}{\tau_\varphi}+\frac{1}{\tau_B}\right)^{-1/2} - \left(\frac{1}{\tau_\varphi}+\frac{1}{\tau_e}+\frac{1}{\tau_B}\right)^{-1/2}\right]. \tag{19}$$

Here, we note that the model converges to the previous Al'tshuler-Aronov model for the case where $\tau_\varphi \gg \tau_e$.

6.5 Spin-Orbit Interaction

It is at this point that we will consider how spin-orbit interaction can fit into the picture we are building. First, it is best to establish what spin-orbit interaction is, after which we can explore how it might play a role in quantum intereference effects. Spin-orbit interaction, generally speaking, is a relativistic effect where the spin degree of freedom in a particle couples to its orbital motion inside a changing potential environment. It is an effective magnetic field $\mathbf{B}_{so}$ that an electron experiences. It can be expressed through a Lorentz transformation of the electric field of an atomic nucleus into the rest frame of the electron (when $v \ll c$):

$$\mathbf{B}_{so} = -\frac{1}{c^2}\mathbf{v}\times\mathbf{E}, \tag{20}$$

where c is the speed of light. If one uses a quantum mechanical description with more rigor, the Dirac equation can be expanded to order $\left(\frac{v}{c}\right)^2$ [149]:

$$H_{so} = \frac{\hbar}{4m_0^2c^2}\sigma\cdot\mathbf{p}\times(\Delta V_0), \tag{21}$$

where m_0 is the bare electron mass, σ is the Pauli spin vector, $\mathbf{p}$ is the momentum, and V_0 corresponds to the Coulomb potential of the atomic nucleus. Of note is the fact that the momentum of a particle with spin (such as a spin-$\frac{1}{2}$ electron) couples to the changing potential environment. Keeping this in mind, we see that applying an electric field to a system should modulate $\mathbf{B}_{so}$ that an electron experiences. Being as we are not primarily concerned with atomic physics, we want to ask what this means for solid-state systems. When considering the bulk in such systems, the dominant contribution to the spin-orbit term comes from the electron's motion in the bare Coulomb potential in the innermost region of the atomic nuclei[146].

It has been found that broken symmetry contributes significantly to spin-orbit interaction in semiconductors, specifically bulk inversion asymmetry (Dresselhaus [148] type) and structural inversion asymmetry (Rashba [147] type), both of which are present in semiconductors with zinc blende crystal structure.

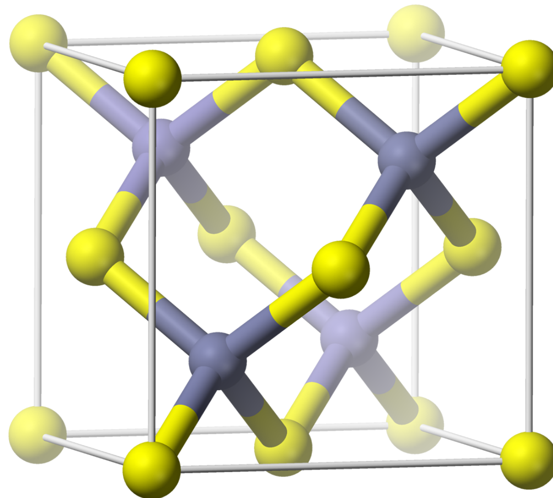

Figure 20: Schematic of a zinc blende crystal structure. Notably, there is no inversion center. Image use under creative commons license.

Such symmetry breakings influence the well-known Kramer's theorem. Leaving spin-orbit interaction aside for a moment, Kramer's theorem states that particles with half-integer spin that obey time reversal symmetry will have a degenerate energy level. If we consider the simple case of a parabolic dispersion relation, that means $E_\downarrow(\mathbf{k}) = E_\uparrow(\mathbf{k})$.

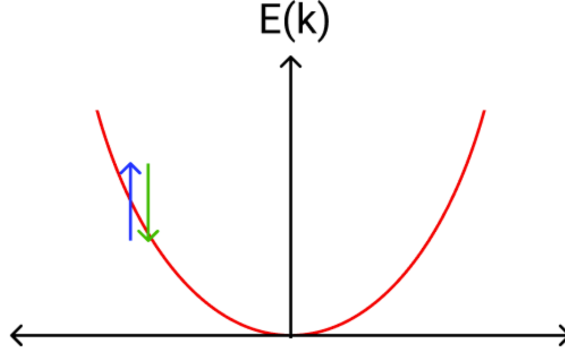

Figure 21: Parabolic dispersion relation of a spin-degenerate conduction band.

Now, returning to cases with spin-orbit interaction, if we consider systems with one of these symmetry breakings, one no longer has this degeneracy between spin up and spin down. Kramer's theorem still holds, however, and time reversal symmetry remains, so one has $E_{\downarrow}(\mathbf{k}) = E_{\uparrow}(-\mathbf{k})$. This splits the degenerate parabola in the previous graph and yields the following dispersion relation:

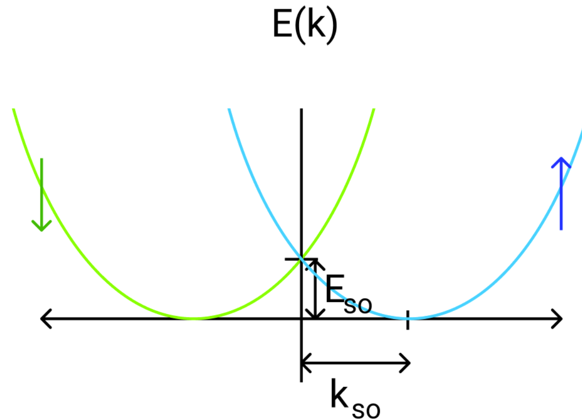

Figure 22: Parabolic dispersion relation of a (Rashba/Dresselhaus) spin-orbit split conduction band. $\mathbf{k}_{so}$ is the spin-orbit momentum and E_{so} is the spin-orbit energy.

Here, we see that the two spin states have different energy. Essentially, our spin-degenerate parabola splits into two shifted parabolas. Additionally, we see that at zero momentum we have an energy which is associated with the total spin-orbit interaction that the carriers in the conduction band experience. The stronger the spin-orbit interaction present in a system, the more the parabolas will shift and the higher the energy at which they cross will be.

Rashba spin-orbit interaction is the dominant type present in the systems investigated in this thesis. Thus, we will leave Dresselhaus aside for the most part, while pointing out that there have been theoretical investigations into the potential for Dresselhaus to make a significant

contribution, if the radius of our nanowires becomes sufficiently small [150]. The structural inversion asymmetry leading to Rashba-type spin-orbit interaction manifests in nanostructures due to electric fields built into the structure. These are often due to gradients in the bandgap at the interface between materials, surface effects, or the presence of ionized dopants. In homogenous InAs and InN nanostructures, the Fermi level of the conduction band is pinned at the surface, which results in the carriers experiencing a large electric field, thus strong Rashba spin-orbit interaction [141][139][151][140][143]. $In_xGa_{1-x}As$ structures with $x \geq 0.8$ have also been shown to exhibit this same pinning effect.

Assuming an isotropic $\mathbf{k}$, the energy associated with the Rashba effect in our systems can be approximated as $E_{so} = \alpha k_F$, where $\alpha = \alpha_0 + \alpha_{mat}\mathbf{E}$ is the Rashba parameter. Further, α_0 is a sample specific offset due to things such as dopant distribution and geometry, α_{mat} is a material specific constant, and $\mathbf{E}$ an external electric field that might be applied to the system. As an electron travels ballistically (between scattering, for example), it is the strength of the spin-orbit interaction which governs the speed with which its spin precesses. Stronger α corresponds to faster spin precession.

Coming back to the external electric field, it is this that could allow for manipulation of the spin-orbit interaction in a system [153][154][155]. This α parameter ties into another parameter we have previously mentioned, the spin-orbit length l_{so} and the two can be related as $l_{so} = \frac{\hbar}{2m^*\alpha}$. Thus, we see that stronger spin-orbit interaction in a system corresponds to smaller l_{so}. This is also sometimes called the spin precession length, because it can be thought of as the length a carrier travels on average before the spin has rotated by 1 radian.

6.6 Weak Anti-Localization

Now, equipped with the knowledge that spin-orbit interaction in a system acts as an effective magnetic field on the carriers, we can investigate what occurs to the weak localization phenomenon that we discussed earlier in the presence of strong spin-orbit interaction. Since we understand that a magnetic field destroys the constructive interference that otherwise yields increased back-scattering, it is natural to expect that the presence of an inherent magnetic field $\mathbf{B_{so}}$ should limit this constructive backscattering. In fact, if the spin degeneracy is broken, the Pauli principle doesn't play a role, and one can expect that most of the back-scattering due to constructive interference should vanish.

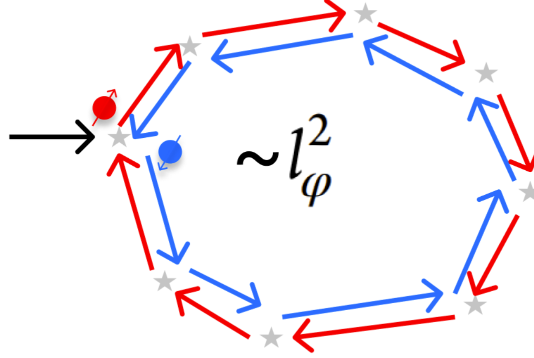

Figure 23: Schematic of a looped path where spin degeneracy has been broken. Paths and their time-reversed partners no longer have the same state, so no constructive interference will take place, resulting in fewer backscatterings.

One can imagine the electrons undergoing repeated disorder-induced scatterings, which randomize their momenta. The spin-orbit interaction then results in a randomization of the spin, which is known as D'yakanov-Perel spin relaxation [156] and is schematically represented below.

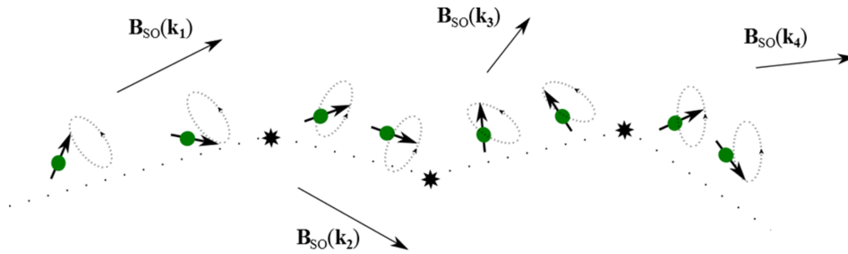

Figure 24: Schematic of an electron path along repeated scatterings, randomizing the spin.

As the electrons move from one scattering center to another, the spins precess around $\mathbf{k}$. To be precise, Rashba spin-orbit interaction causes spin precession perpendicular to $\mathbf{k}$, while Dresselhaus induces it counterclockwise as one moves in k-space [272][273]. This is taking the linear Dresselhaus spin-orbit interaction into account and neglecting the cubic contribution.

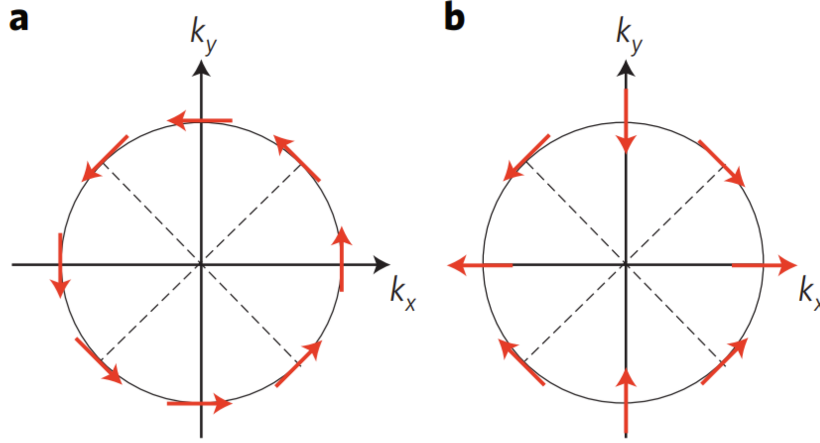

Figure 25: Spin precession with respect to **k** for Rashba (**a**) and (linear) Dresselhaus (**b**). Graphic taken from [273].

Therefore, the randomization of the momenta of carriers undergoing repeated scatterings also serves to randomize their spin. This actually *reduces* the return probability, which manifests as an *increase* in conduction at $\mathbf{B} = 0$. This increase in conduction at $\mathbf{B} = 0$ is called *weak anti-localization*. It can be thought of as destructive interference as opposed to the constructive interference of weak localization. The application of a magnetic field then acts to remove this destructive interference and typically results in a decrease in conduction just outside of $\mathbf{B} = 0$. Eventually, in systems with medium strength spin-orbit interaction, with a larger applied magnetic field the conductance tends to grow again and settle at the classical Drude conductance (ignoring UCF). It is as if a small increase in conduction at $\mathbf{B} = 0$ is embedded in a larger scale weak localization behavior.

There is a simple picture, first presented by Gerd Bergmann [275], to arrive at the increase in conduction due to spin-orbit interaction in diffusive systems. One begins with the acknowledgement that it has been demonstrated that spin-$\frac{1}{2}$ particles must rotate by 4π in order to transfer the spin function into itself [276]. Rotation by 2π will reverse the sign of the spin state. If we consider the initial spin state, $\mathbf{s}$, of a conducting electron undergoing multiple scatterings, the resultant final spin state, $\mathbf{s}'$, is $\mathbf{s}' = \mathbf{R}\mathbf{s}$, with $\mathbf{R}$ a rotation operator. Then, the time-reversed partner of $\mathbf{s}'$, $\mathbf{s}''$, can be represented by $\mathbf{s}'' = \mathbf{R}^{-1}\mathbf{s}$, where $\mathbf{R}^{-1}$ has the same scatterings as $\mathbf{R}$ but in opposite order. This is represented schematically in the diagram below.

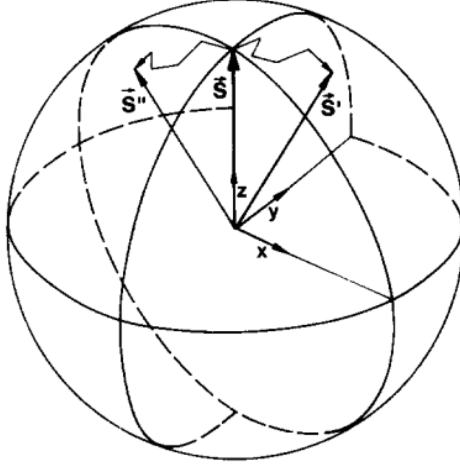

Figure 26: Spin precession of state $\mathbf{s}$ undergoing multiple scatters and ending up in state $\mathbf{s}'$ or $\mathbf{s}''$ for its time-reversed path. Graphic taken from [275].

In the case of strong spin-orbit interaction on the one hand, $\mathbf{s}'$ has lost its knowledge of its original spin orientation, with its resultant orientation statistical. On the other hand, $\mathbf{s}''$ should have experienced exactly the opposite rotation in its orientation. When the relative orientation between $\mathbf{s}'$ and $\mathbf{s}''$ is 2π, the amplitudes will be destructive.

We can go a bit deeper than the simplified picture and additionally consider that our carriers are going to be broken into spin singlets ($|0,0\rangle = \frac{1}{\sqrt{2}}(\uparrow\downarrow - \downarrow\uparrow)$ with spin $S = 0$) and triplets ($|1,1\rangle = \uparrow\uparrow$; $|1,0\rangle = \frac{1}{\sqrt{2}}(\uparrow\downarrow + \downarrow\uparrow)$; $|1,-1\rangle = \downarrow\downarrow$ with spin $S = 1$). These four states and their respective eigenvalues are responsible for the quantum corrections in a system hosting spin-orbit interaction. The antisymmetric nature of the singlet state upon the exchange of an incident and scattered spin generates a minus sign, which results in a positive contribution to conduction. It is this positive contribution that yields the antilocalization behavior. Meanwhile, the triplet states are symmetric under such exchanges, which contribute negatively to conduction. It is these that make up the weak localization behavior [277][278]. Strong spin-orbit interaction should specifically suppress the triplet contribution to Cooperon and diffuson channels, thus should reduce the variance in conduction by a factor of four (going from four interfering channels to, effectively, one) [145] when there is no external magnetic field applied. The randomization of the spins and the resultant spin relaxation due to the D'yakanov-Perel mechanism suppresses interference of time-reversed paths in triplet configurations, leaving the singlet interference unchanged.

6.7 Weak Anti-Localization Formalism

At this point we can consider the addition of spin-orbit effects on the formalism for $\Delta G(B)$. It was in the 1980s that the influence of spin-orbit interaction on weak localization was studied in 2DEG systems [157][159][160][161][162]. If we fast forward to 1992, Kurdak et al. expanded upon the Al'tshuler-Aronov theory to include spin-orbit interaction in the case of narrow channels in 2DEGs[158]. This narrow channel geometry assumes diffusive Brownian motion in a plane, with no possible motion out of the plane. They included an additional term to the integral over the return probabilities that accounts for spin precession in a system:

$$\Delta G(B) = \frac{-2e^2}{\pi\hbar}\frac{D}{L}\int_0^\infty dtC(t)e^{-t/\tau_\varphi}\left[\frac{1}{2}\left(3e^{-4t/3\tau_{so}} - 1\right)e^{-t/\tau_B}\right], \tag{22}$$

assuming an isotopic τ_{so}. The $\frac{1}{2}$ comes from the convention that all expressions refer to one spin degree of freedom. Here, two interesting features have been added to the integral. First, the -1 represents the spin singlet state. The remaining term, $3e^{-4t/\tau_{so}}$, accounts for the spin triplet states. In the event of strong spin-orbit interaction, i.e. if τ_{so} is very small, one receives a factor of $-\frac{1}{2}$, which yields the increased conduction in weak anti-localization due to the spin-orbit interaction in the system. The above equation can be solved and one is left with

$$\begin{aligned}\Delta G(B) = \frac{-2e^2\sqrt{D}}{\pi\hbar L}\Bigg[&\frac{3}{2}\left(\frac{1}{\tau_\varphi} + \frac{4}{3\tau_{so}} + \frac{1}{\tau_B}\right)^{-1/2} - \frac{1}{2}\left(\frac{1}{\tau_\varphi} + \frac{1}{\tau_B}\right)^{-1/2} \\ &- \frac{3}{2}\left(\frac{1}{\tau_\varphi} + \frac{4}{3\tau_{so}} + \frac{1}{\tau_e} + \frac{1}{\tau_B}\right)^{-1/2} + \frac{1}{2}\left(\frac{1}{\tau_\varphi} + \frac{1}{\tau_e} + \frac{1}{\tau_B}\right)^{-1/2}\Bigg]. \end{aligned} \tag{23}$$

These days, most experimentalists are expressing this quantum mechanical correction to the classical conduction in terms of the associated length scales, l_i, instead of the time scales τ_i. One reason is that the mean free path, l_e, and coherence length, l_φ, can often be obtained by other measurements on the system. This results in the following:

$$\Delta G = -\frac{e^2}{hL}\left[3\left(\frac{1}{l_\varphi^2}+\frac{4}{3l_{so}^2}+\frac{1}{l_B^2}\right)^{-1/2} - \left(\frac{1}{l_\varphi^2}+\frac{1}{l_B^2}\right)^{-1/2} \right.$$
$$\left. - 3\left(\frac{1}{l_\varphi^2}+\frac{4}{3l_{so}^2}+\frac{1}{l_e^2}+\frac{1}{l_B^2}\right)^{-1/2} + \left(\frac{1}{l_\varphi^2}+\frac{1}{l_e^2}+\frac{1}{l_B^2}\right)^{-1/2}\right]. \quad (24)$$

In order to give a visual picture of the transition from weak localization into weak antilocalization, the following simulation has been carried out using typical (fixed) parameters for L, W, l_φ, l_e, while varying l_{so}. The fixed values are taken to correspond approximately to those obtained in the work presented in chapter 9.

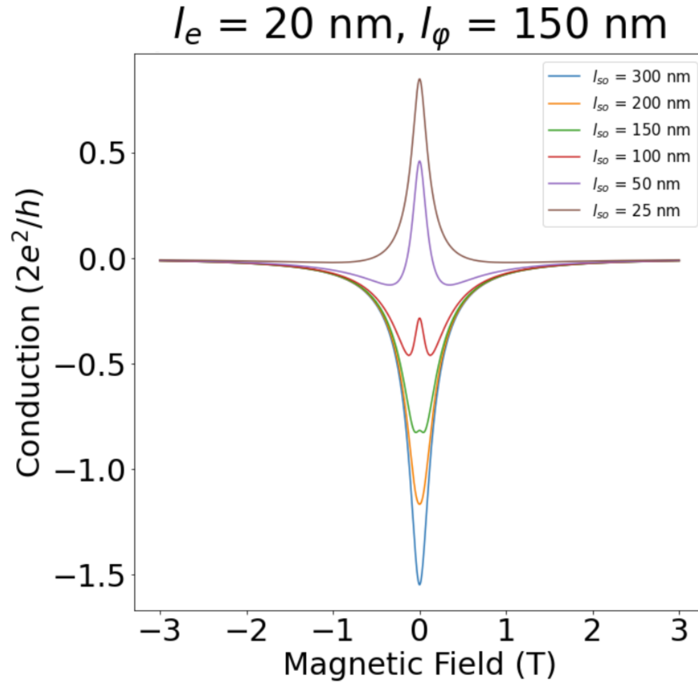

Figure 27: Simulation of transition from weak localization to weak anti-localization with changing l_{so}. Here, L = 500 nm, W = 80 nm, l_e = 20 nm, and l_φ = 150 nm are kept fixed.

With a larger l_{so} - i.e. smaller spin-orbit interaction - we see a pronounced decrease in conduction, a characteristic of weak localization. As l_{so} decreases in size, corresponding to increased spin-orbit interaction, we see the onset of a local maximum in G. This is eventually followed by a pronounced increase and a global maximum.

7 Nanofabrication

Nanofabrication on these novel structures has a few additional challenges when compared with more conventional nanowire device preparation. Detailed fabrication recipes can be found in a later section; this section will serve to qualitatively explain the non-standard processes that needed to be employed for engineering devices. After the growth of the samples is carried out by the material scientists that we collaborate with, triangular chips with three samples each arrive at our institution. The fabrication of the samples themselves have a few particularities compared to standard device fabrication methods. The first thing of note is that the GaAs [111] substrates have a three-fold crystal symmetry. This is in some ways a benefit (see Chapter 9) we exploit, though in others an additional obstacle. One aspect of this symmetry results in the wafers cleaving into triangular, rather than squared directions. This is, in principle, not a major issue when handling the chips with tweezers, though it does increase the likelihood that a sample may slip out from the grip. Careful efforts are taken to mitigate this and, over time, one becomes adept in quickly picking up and moving the samples in and out of time-sensitive processes.

The structures have a large aspect ratio. Typically, the nanomembranes grow to around 300 nm, on top of which the nanowires grow roughly 50 nm higher. This results in a handful of aspects that require particular attention. E-beam lithography requires a much higher resist than typically applied in nanowire fabrication ($\gtrsim$ 500 nm), since the resist needs to be larger than the height of the structures for lithography and, later, liftoff. After lithography, development, and surface passivation, metallization also needs to be treated carefully. The high aspect ratio makes it such that planar evaporation of metal fails to adequately cover the side walls of the membranes. As a result, we employ a dual-angle approach to metal deposition. First, the sample is tilted at an angle of $\sim 20°$ in one direction with respect to the nanomembranes and the metal is deposited. Second, without breaking the vacuum, the sample is tilted $\sim 20°$ in the opposite direction, whereupon the second metal layer is deposited to ensure continual coverage up and down both sides. In order to be absolutely certain that there are no breaks in the metallization, a thin third planar (untilted) layer can also be deposited.

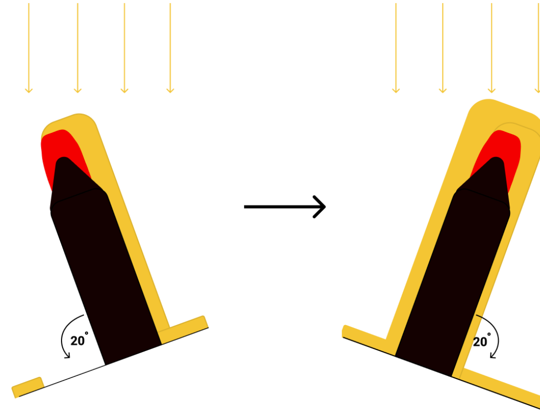

Figure 28: Cross-sectional schematic of two-step angle evaporation process to ensure full side wall coverage. Left: first layer deposited with membranes tilted at $\sim 20^{\circ}$ in one direction. Right: second layer deposited with a tilt of $\sim 20^{\circ}$ in the opposite direction. Black is the nanomembrane, red is the In(Ga)As nanowire, gold is the metal.

In contrast to conventionally-grown nanowires, which can be deposited onto a doped substrate with an insulating layer above that can act as a global back gate, the selective-area grown structures studied here cannot currently be grown from a doped substrate without the entire chip conducting. Therefore, in order to electrostatically control the electron density in the wires, top gate architectures needed to be developed. In order to do this, an insulating dielectric layer had to be applied to the samples first. This is done using an in-house atomic layer deposition (ALD) machine. HfO_2 has been used as the dielectric for all the devices investigated in this work. One reason is that HfO_2 is a high-k dielectric, which should result in a strong gate capacitances without leakage. Additionally, it was known to be the cleanest material using our in-house ALD machine. Therefore, it was determined that it was the best available candidate. HfO_2 is an extremely durable material and is difficult to etch, with no standard labratory etchant selective to it. As a result of this, the HfO_2 needed to be selectively deposited to cover the contacted nanostructures, without covering the areas of the chip where contact pads were placed. It was found that it was impossible to wire-bond onto the pads if the HfO_2 was deposited above them. Therefore, an ALD window scheme needed to be developed that enabled the selective deposition. This was done using a tall (~ 1 μm) two-layer resist stack (see Fabrication Recipe chapter for exact details), followed by e-beam lithography to open up a window where the structures requiring the insulating dielectric sat. Then, the ALD process with HfO_2 was carried out; the tall resist stack allowed for a reproducible liftoff process, leaving the HfO_2 only where it was desired.

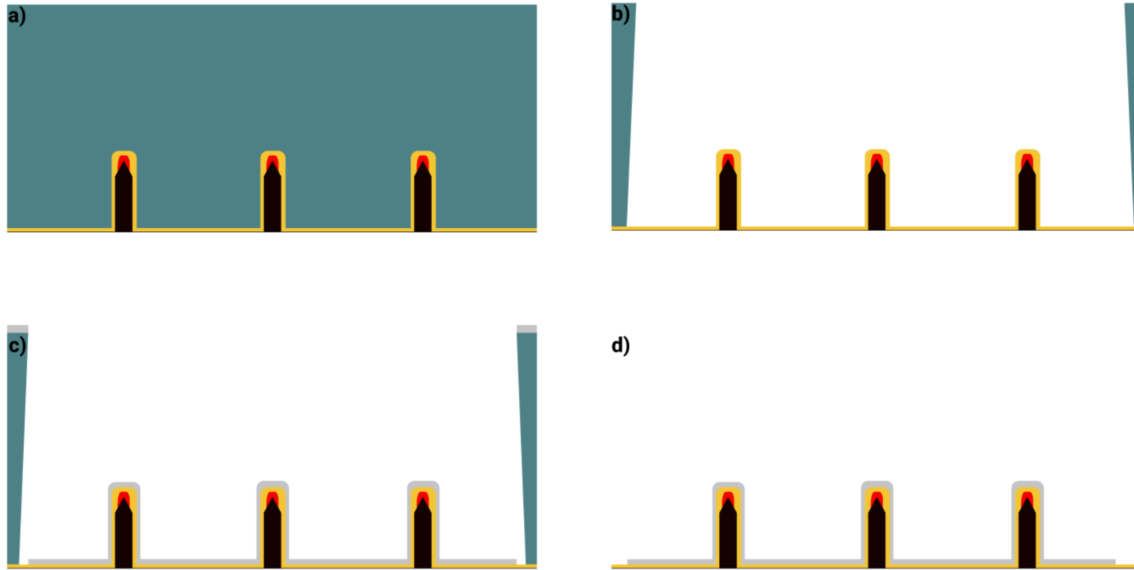

Figure 29: Cross-sectional schematic of selective ALD deposition process onto contacted wires. a) $\sim 1\ \mu$m resist stack. b) e-beam lithography to open up the selective window. c) ALD of HfO_2. d) Lift-off process leaving HfO_2 selectively covering contacted nanowires. Black are the nanomembranes, red is the In(Ga)As nanowires, gold are the metal contacts, teal is the e-beam resist stack, grey is the HfO_2 dielectric.

After the HfO_2 window is deposited, top gates can be patterned with e-beam lithography. The metallization is then carried out in a similar dual-angle evaporation step. This results in top gates, which wrap around the sides and top of the nanowires. The result of this wrap-around top gate is that we are able to tune the carrier density in the nanowires without applying a significant electric field across the wire itself [163]. This is expounded upon in more detail in the Outlook and Summary chapter.

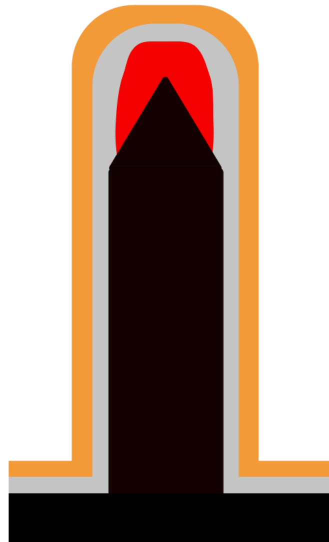

Figure 30: Cross-sectional schematic of wrap-around top gate. Black are the nanomembranes, red is the In(Ga)As nanowires, orange is the top gate, and grey is the HfO_2 dielectric.

As mentioned in the previous chapter, if one would like to influence Rashba spin-orbit interaction, it is necessary to apply and control an electric field across the wire. For this purpose, a split-gate prototype architecture was designed and implemented. Such a split-gate should allow for the modulation of the carrier density as well as the electric field applied across the wire independently. In order to create devices like this a more complex fabrication process where the large aspect ratio of the structures was leveraged. The start of the split-gate fabrication process is carried out in the same manner as the wrap-around gate devices. Contacts are lithographically defined and a dual-angle metallization is done. At that point, selective deposition of HfO_2 is done using the process outlined above. Next, another round of e-beam lithography is carried out to define the placement of the first gate layer. Next, when the devices are placed into the metal evaporator, metallization is done, this time from *one* angle only. This utilizes the angle combined with the height of the nanostructure to shield the opposite side of the nanowire from metal deposition.

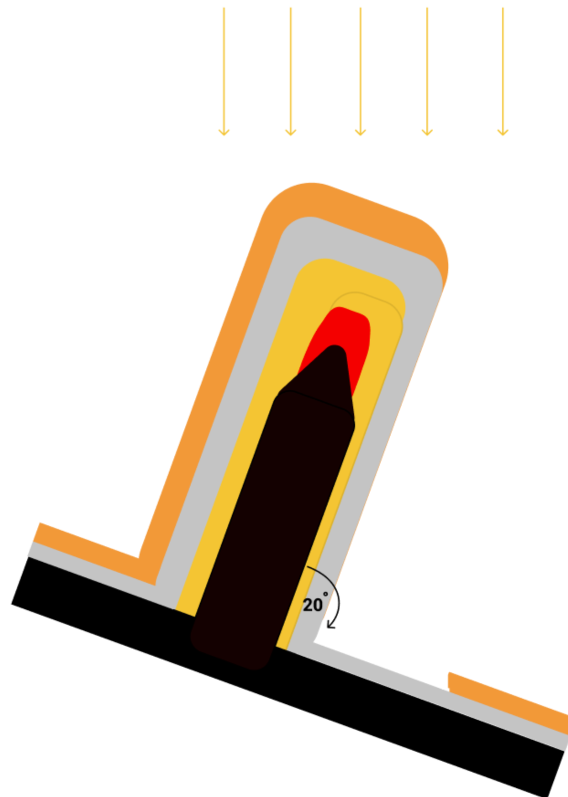

Figure 31: Cross-sectional schematic of first gate in split-gate architecture. Black are the nanomembranes, red is the In(Ga)As nanowires, gold are the metal contacts, orange is the gate, and grey is the HfO_2 dielectric.

After this first top gate layer is deposited, another HfO_2 layer is applied selectively using the same process outlined above. Then, the second top gate is lithographically defined, whereupon

the second gate is placed by doing the tilted metallization, this time at the other angle only.

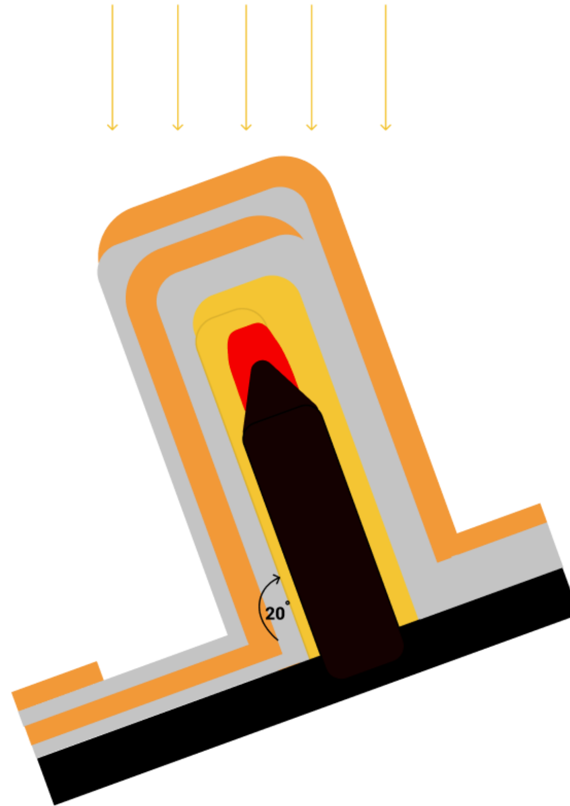

Figure 32: Cross-sectional schematic of second gate in split-gate architecture. Black are the nanomembranes, red is the In(Ga)As nanowires, gold is the metal contact, orange are the gates, and grey is the HfO_2 dielectric.

At the end of this process, we are left with two gates that can enable the tuning of carrier density and electric field across the nanowire independently. It should be noted that the gates are applied across the entirety of the wire, including where the contacts are placed. It was found that the leakage current from the gates to the contacts was negligible when the HfO_2 layers were $\gtrsim$ 16 nm. Below, is a schematic without the contact layer in order to illustrate the concept of tuning density and electric field in the wire independently.

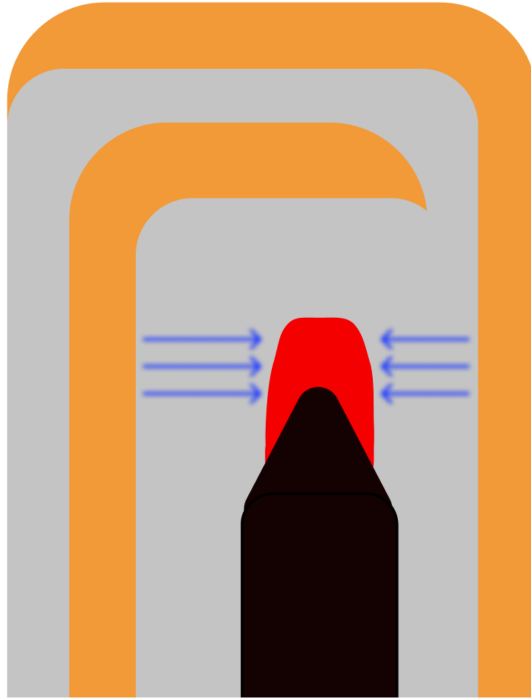

Figure 33: Cross-sectional schematic of finished split-gate architecture. Black are the nanomembranes, red is the In(Ga)As nanowires, orange are the gates, grey is the HfO_2 dielectric, and blue arrows represent the application of an electric field.

In demonstrating that these novel nanostructures can be fabricated into a fin field-effect transistor (FinFET) device architecture is another aspect that speaks to the viability of future scalable systems. FinFETs are the industry standard for semiconductor chip design, driving the great majority of all electronic devices currently on the market [164][165][166][167].

8 Template-Assisted Scalable Nanowire Networks

M. Friedl[1], K. Cerveny[2], P. Weigele[2], G. Tütüncüoglu[1], S. Marti-Sanchez[3], C. Huang[4], T. Patlatiuk[2], H. Potts[1], Z. Sun[4], M. O. Hill[4], L. Güniat[1], W. Kim[1], M. Zamani[1], V. G. Dubrovskii[5], J. Arbiol[3,6], L. J. Lauhon[4], D. M. Zumbühl[1], and A. Fontcuberta i Morral[1]

[1] Laboratoire des Matériaux Semiconducteurs, École Polytechnique Fédérale de Lausanne, EPFL, 1015 Lausanne, Swizterland

[2] Department of Physics, University of Basel, Klingelbergstrasse 82, CH-4056 Basel, Switzerland

[3] Catalan Institute of Nanoscience and Nanotechnology (ICN2), CSIC and BIST, Campus UAB, Bellaterra, 08193 Barcelona, Catalonia Spain

[4] Department of Materials Science and Engineering, Northwestern University, Evanston, Illinois 60208, United States

[5] ITMO University, Kronverkskiy pr. 49, 197101 St. Petersburg, Russia

[6] ICREA, Pg. Lluís Companys 23, 08010 Barcelona, Catalonia, Spain

This chapter was published in *Nano Lett.* **18**, 2666-2671 (2018).

8.1 System Introduction

In the past few years, much progress has been made toward fabricating and scaling up qubit density to build universal quantum computing systems that could potentially outperform classical computers by quantum schemes [47][81][82][83][84]. The ideal qubit should combine long coherence times, fast qubit manipulation, and small size, while maintaining scalability to many-qubit systems. Long coherence times are fundamentally challenging to achieve in various qubit systems due to the presence of numerous forms of environmental noise, requiring operating temperatures in the range of a hundred millikelvin [85][86]. A system, which has been proposed to be much more robust against such perturbations, is the topological qubit [87]. This type of qubit, for example, composed of MFs or MPFs [88][89], would have the inherent property of being topologically protected and would, thus, exhibit exceptionally long coherence times. Signatures of MF states have been observed experimentally in, among other systems, III-V semiconductor NWs in close proximity to an s-wave superconductor [90][91], while a few other groups have reported anomalous MF signatures in similar systems [92][93][94]. In general, these studies have focused on using III-V materials, such as InAs and InSb, due to their high spin-orbit coupling strength and g factor [95]. Current efforts are focused on performing the first manipulations of MFs to further verify theoretical predictions, for which low-disorder, connected 1D branches are required. Gold-free and defect-free NW branches made of a high purity, high spin-orbit III-V material would be an ideal platform for manipulating MFs. Excellent progress has been made toward this goal with reports on the growth of monocrystalline gold-assisted InSb NW branches, which display a weak antilocalization due to the large spin-orbit interaction of the material, as well as a hard superconducting gap. Scalability is another important aspect of any future computation system, and on this front, the Riel group has recently demonstrated patternable ballistic InAs NW crosses through template-assisted growth on silicon [96].

Despite recent progress, a few challenges still exist with current methods to produce branched structures. The fabrication of NW networks and intersections has been explored for many years for classical computing by overlapping individual wires [97][98][99]. For MF applications, the stringent requirement of maintaining coherent transport across the intersection means that, currently, the most popular NW cross structures rely on the intersection of two gold-catalyzed NWs grown along two different <111> B directions, leading to an interface-free junction [100][101][102][103][104]. After growth, free-standing crosses are obtained, which then need

to be transferred onto a separate substrate for further device fabrication, limiting the ultimate scalability. A scalable scheme would instead enable the NW growth and intersections to be realized directly on the final device substrate. At the same time, for future device integration, the use of gold seeds poses a problem for compatibility with CMOS technologies [105]. Here, we demonstrate a new approach to grow gold-free branched In(Ga)As NWs at the wafer scale by using GaAs NMs as templates.

Defect-free GaAs NMs of exceptional quality constitute the ideal templates for further In(Ga)As NW growth [106][107]. Such structures have been successfully grown by, both, metal-organic chemical vapor deposition (MOCVD) and molecular beam epitaxy (MBE) using a gold-free selective area approach [80]. The NMs are patternable at the wafer scale and can, additionally, be fabricated in the form of Y-shaped structures by growing along the three <11-2> directions on GaAs (111) B substrates. When the growth of these GaAs NMs is followed by InAs, the InAs accumulates at the top of the NMs, forming In(Ga)As NWs along the NM vertex, as depicted schematically below.

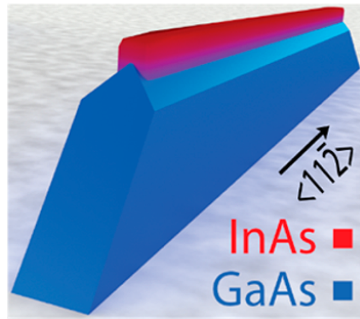

Figure 34: Schematic of an GaAs NM (blue), atop which an InAs NW is formed (red) [81].

By varying the deposition times and growth conditions, the size and composition of the NWs can be changed. The growth progression, which initiates as InGaAs and then evolves to pure InAs for longer growth times, is shown below.

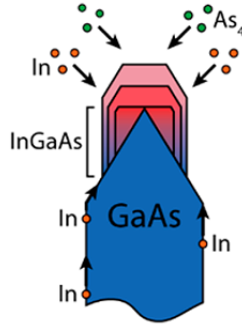

Figure 35: Schematic of the growth of a NW of first InGaAs at the interface, which transitions into pure InAs as it grows further from the GaAs NM [81].

Combining the concepts of patterning NMs into Y-branches and performing In(Ga)As NW growth on top of GaAs NMs, Y-shaped In(Ga)As NW junctions can be obtained, as seen below. Our approach thereby enables the growth of gold-free branched NWs at the wafer scale.

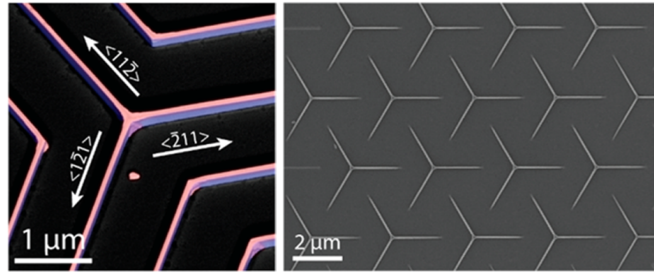

Figure 36: Left : A 30° tilted scanning electron microscope (SEM) image of a branched NM/NW structure, taken with an energy-selective back-scattered electron detector for z-contrast. The image is false-colored for visibility and annotated with relevant substrate directions. **Right** : SEM image of branched NW structures grown in a regular array [81].

Here, as the first step toward building MF devices based on this approach, we demonstrate the growth of low-defect linear Al(Ga)As NWs based on GaAs NMs. Magnetotransport measurements on an array of nanowires (depicted below) demonstrate weak localization in the diffusive regime, suggesting quasi-1D quantum transport. This makes such NWs ideal candidates for future quantum computing schemes.

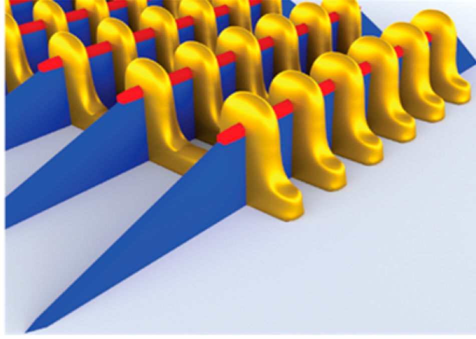

Figure 37: Model of an array of contacted linear NM/NW structures used in magnetotransport measurements [81].

8.2 Nanomembranes as a Platform

Membranes with top ridges parallel to the substrate were grown, as described previously [51]. The InAs NWs were then grown for 200 s at an As_4 flux of 8×10^{-6} Torr, an In rate of 0.2 Å/s and a substrate temperature of 540 °C. This optimized substrate temperature yielded continuous InAs growth on top of the NMs. A Si dopant flux of 10^{13} atoms/cm^2/s was also introduced to increase the conductivity of the NWs.

The NW morphology, composition, and structural quality were extensively characterized by correlated analysis using various electron microscopy techniques. These included electron energy loss spectroscopy (EELS) and atomic-resolution aberration-corrected annular dark field scanning transmission electron microscopy (ADF - STEM). The results were then coupled with geometrical phase analysis (GPA) to give strain information [82][83], which, in turn, was fed into a semi-empirical model to understand the formation of the NWs from a theoretical standpoint.

Analysis of focused ion-beam (FIB) lamellas prepared perpendicular to the NW axis by ADF-STEM and correlated EELS show that 50 nm diameter InAs NWs form on the 250 nm tall GaAs NMs. The InAs material preferentially accumulates along the top ridge of the GaAs NM, forming the NW, which is primarily InAs with a 20 nm thick intermixed InGaAs region at its base. This InGaAs region likely occurs due to strain-mediated intermixing with the GaAs NM below, as has been observed in InAs quantum dots on GaAs [84]. It is important to note that we observe no In signal from the NMs; the faint signal seen in the EELS map is believed to be created during the FIB cutting by a combination of redeposition of the TiO_x protective layer and surface diffusion of the highly mobile In adatoms.

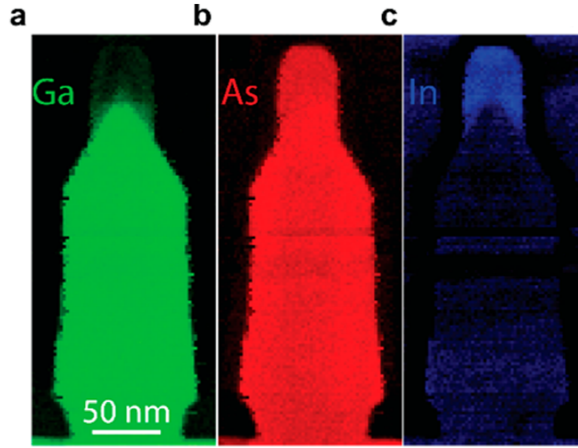

Figure 38: **a** – **c** : EELS maps with elemental contrast of a NM/NW cross section. Note that the overlap of the In EELS signal with the Ti signal from the TiO_x capping layer has caused an anomalous background of In within the NM, which is not physical [81].

Looking instead at the NW facets, as seen below, the resulting InAs NW structures are terminated by two (110) facets on the sides and have a single flat (111) top facet. The appearance of this (111) facet, instead of the two {113} facets as in the GaAs NMs, can be explained by the higher As_4 flux used in the InAs NW growth [85][86].

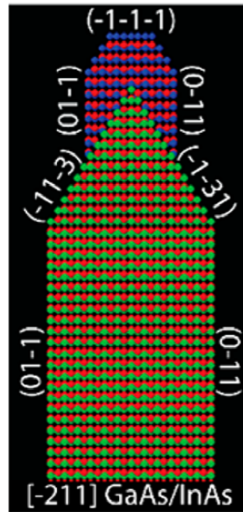

Figure 39: Atomic model showing faceting of the NM/NW heterostructure [81].

No defects were observed when viewing this transverse lamella in atomic-resolution ADF-STEM mode. As strain along the NW axis was predicted to be more difficult to relax than in the transverse direction, a second FIB lamella was prepared parallel to the axis of the NW and also imaged using atomic-resolution ADF-STEM. Here, a few misfit dislocations were observed near the InAs/GaAs interface, with an estimated density of approximately 100/μm (see Supplementary Information section). This constitutes a 40 % reduction in dislocation density with

respect to the equivalent 2D growth of InAs on GaAs and at least three times improvement with respect to the twin density typically observed in self-catalyzed InAs NWs [88][89][90].

Turning now to explaining the morphology of the structures, an analytical model shows that the surface and strain energy minimization play the most important role in driving the NW to adopt the observed shape (see Supplementary Information section). By taking advantage of the atomic resolution offered by ADF-STEM images, GPA was performed on the initial FIB lamella cut perpendicular to the NW axis. Looking specifically at the (111) plane spacing, a substantial 2-3 % residual compressive strain is observed within the NW, with the corresponding line scan given in the figure below.

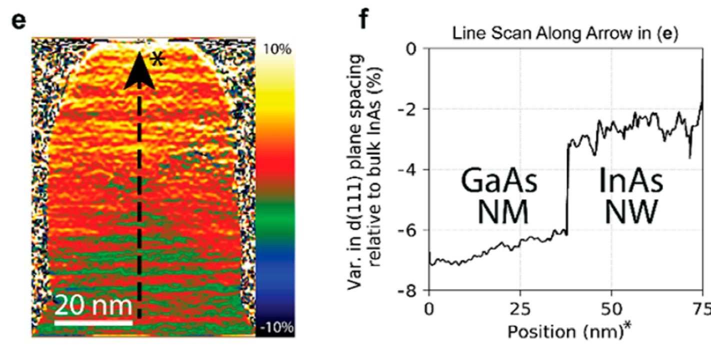

Figure 40: **e** : GPA map of the InAs NW region. **f** : Line scan along arrow in **e** [81].

Using this strain value, a semiquantitative model was developed to describe the NW formation energy, taking into account the InAs/GaAs surface energies and the InAs elastic strain energy. The total energy of the system was then minimized with respect to the NW aspect ratio. Interestingly, the experimentally observed aspect ratio coincides with that of the theoretical minimum energy shape, suggesting that the NW shape is simply driven by energy minimization (for more detail see Supplementary Information section).

8.3 Electrical Transport in the Mesoscopic Regime

To bring the NWs into the 1D electrical transport regime, they were downscaled to 20 nm diameters by narrowing the GaAs NMs by using smaller SiO_2 openings and shorter growth times for less lateral growth. The resulting NWs were smaller, both, laterally and vertically, resulting in intermixed InGaAs NWs, as depicted for small diameter NWs in the growth progression diagram in Figure 17. These results were confirmed by performing atom probe tomography (APT), which additionally yielded information about the Si dopant distribution.

The APT analysis confirmed the presence of an InGaAs NW, while also uncovering signs of dopant rejection during crystal growth, causing an accumulation of Si atoms at the NW surface. A typical APT map of the of the In mole fraction and the Si dopant distribution and a quantitative composition profile of the NW surface was extracted in the proximity histogram (proxigram) shown below.

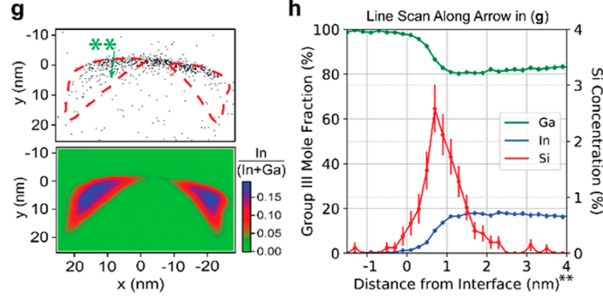

Figure 41: g : APT map of scaled-down NWs used in electrical measurements showing In concentration (lower map) and accumulation of Si dopant atoms (black dots) at the surface of the NW with In isoconcentration lines as a guide to the eye (upper map). Note that, since the NWs were capped with GaAs for APT analysis, the measured In concentration can be considered as a lower bound for the uncapped structures. **h** : Proxigram line scan along the dashed arrow in panel **g** showing Si accumulation on the NW top facet and In concentration within the NW[81].

In this sample, the NW group III mole fractions are 17 % In and 83 % Ga. (Additional maps in Supplementary Information section) Analysis of different InGaAs samples by APT tomography under similar conditions shows a slight tendency toward preferential In evaporation. In addition, a GaAs capping layer was deposited on the PT sample after the NW growth, which may have enhanced the Ga intermixing [91]. For these reasons, we consider the In mole fraction in this NW as a lower bound. Although a Si flux was present during InAs NW growth, the Si atoms are not homogeneously distributed throughout the NW. The Si atoms instead appear to accumulate preferentially at the (111) growth interface, resulting in a quasi-remotely doped structure.

The electrical properties of the NWs were explored through multi-contact resistance measurements on an array of NWs, for which an example device is shown below.

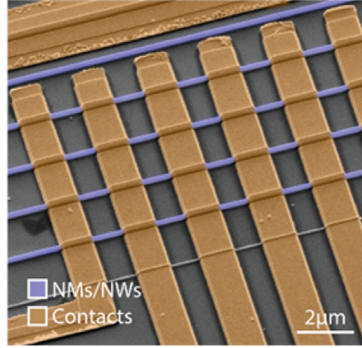

Figure 42: False-colored SEM image of four InAs/GaAs NW/NMs contacted in parallel [81].

An array of 34 NWs, comparable to those on which APT was performed, was used for these tests as a way to obtain the average response for many devices. Standard four-point measurements were then carried out at room temperature before moving to low-temperature magnetoconductance transport experiments.

Room-temperature transmission line measurements, shown below, gave linearly scaling and repeatable resistances, suggesting that a good-quality contact was achieved. A control sample without InAs NWs shows an increase of resistance by five orders of magnitude, directly proving that the observed conduction occurs due to the InAs deposition. Device behavior remained linear and ohmic down to 4.2 K, albeit with an increased contact resistance.

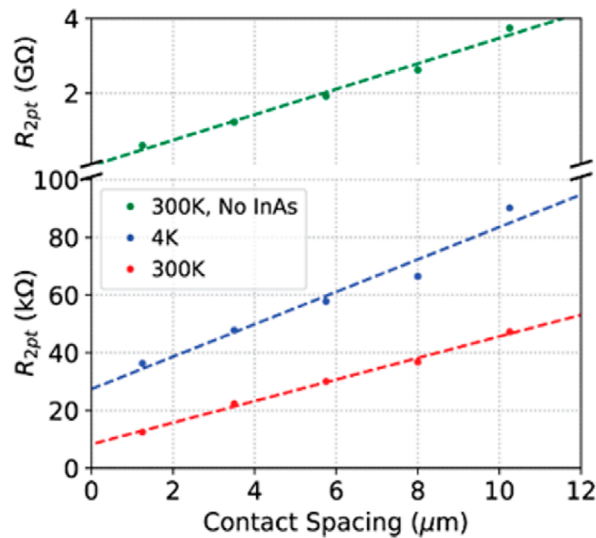

Figure 43: Transmission line measurement to extract contact resistance and resistivity (per NW) at 4.2 and 300 K, in comparison to NMs without the InAs deposition step [81].

Magnetoconductance measurements at 1.5 K revealed a zero-field minimum of conductance consistent with weak localization (WL) behavior. The conductance of the devices was measured under constant bias, while the magnetic field was applied perpendicular to the substrate and was

swept from -8 to 8 T. This analysis indicated conduction in the quasi-1D transport regime and elucidates important quantum figures of merit, such as coherence length l_φ, mean free path l_e, and spin-orbit length l_{so}.

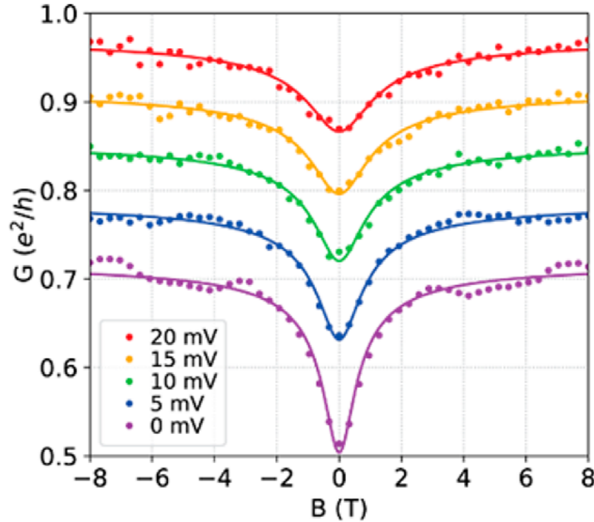

Figure 44: Average different conductance per NW as a function of magnetic field perpendicular to the NWs for a range of bias voltages measured at 1.5 K for a 1.25 μm long NW segment. The traces for biases above 0 mV are offset for clarity [81].

A coherence length l_φ of 130 nm and a lower bound on the spin-orbit length l_{so} were obtained by fitting the experimental data. The system was assumed to be in the diffusive regime with the electron mean free path $l_e \ll W$, with W being the width of the conducting channel, estimated from the APT results to be about 20 nm. In this regime, l_e is thus constrained to be a few nanometers due to the large amount of dopant and surface scattering. A simple quasi-1D model for the quantum corrections to the conductivity in the diffusive limit (see Methods) gives an excellent agreement with the data and yields l_φ 130 $\pm$ 4 nm near zero bias, as shown in the solid traces in the figure above. In the absence of weak anti-localization and adding spin-orbit coupling to the model (see Supplementary Information section), a lower bound for l_{so} of 280 nm is estimated. Some small variations in the conductance at large magnetic fields are noticable, presumably signatures of conductance fluctuations, which are strongly suppressed due to averaging from the parallel NW arrangement as well as the relatively short coherence length.

These initial results show that the electron confinement at the top of NWs grown on NMs is sufficient to produce quasi-1D conduction. These NWs could, therefore, be viable hosts for Majorana bound states, provided that two main potential obstacles are addressed. First, a NW made of higher spin-orbit material, such as pure or nearly pure InAs or InSb, will be required; i.e.,

intermixing should be reduced or eliminated. This will be apparent by the observation of weak anti-localization instead of weak localization. Second, impurity, interface, and alloy scattering need to be reduced, such that l_e transitions from the diffusive to the ballistic transport regime.

8.4 Conclusion and Outlook

The fast-growing field of quantum computing and the promise of robust, topologically protected qubits with III-V NWs drives the pursuit of scalable approaches to branched NW networks. We have described a path forward, using GaAs NMs as templates for the In(Ga)As NW growth. By exploiting strain in the highly mismatched InAs/GaAs system, continuous, low-defect NWs were formed. We have further observed weak localization, demonstrating that such NWs can provide sufficient confinement to achieve quasi-1D conduction. Our gold-free wafer-scale approach to branched NWs serves as a platform for future investigations into 1D transport and quantum computation with III-V NW networks with many exciting possibilities. From the MBE growth perspective, using GaSb NMs already described by other groups to grow InSb NWs would be interesting due to the higher g-factor of InSb [40][92]. Alternatively, suitable plastic strain relaxation, for example, by interfacial misfit array formation [93] may enable GaAs NMs to be viable templates for InSb NW growth. At the same time, the growth of new kinds of structures with additional functionalities is another avenue to explore, including, for example, research into parafermion devices by stacking multiple NWs on top of each other [34]. The wealth of intriguing new possibilities and approaches offered by template-assisted III-V NW growth makes this method an important step toward realizing a scalable quantum computing scheme based on NW topological qubits.

8.5 Methods

8.5.1 Substrate Preparation

Undoped GaAs (111) B substrates were prepared by first depositing 25 nm of SiO_2 by the plasma enhanced chemical vapor deposition (PECVD). This was followed by e-beam lithography, using ZEP resist and low-temperature development to achieve low line edge roughness [94]. Subsequent dry etching with fluorine chemistry was used to etch the SiO_2 down to the GaAs surface, and a final wet etch in a dilute buffered HF solution helped remove any remaining oxide. This yielded openings varying from 30 to 100 nm in width and 10-20 μm in length, depending on the e-beam

pattern.

8.5.2 Growth

The nanostructures were grown in a DCA D600 Gen II solid-source MBE. The optimal growth of the GaAs/InAs NM/NW heterostructures was found to be at a temperature of 630 °C/540 °C (as measured by the pyrometer), As flux of $4 \times 10^{-6}/8 \times 10^{-6}$ Torr and Ga/In deposition rates of 1.0/0.2 Å/s, respectively. The NMs were typically grown for 30 min (180 nm nominal 2D thickness), while the InAs NWs were grown for 200s (4 nm nominal 2D thickness).

8.5.3 (S)TEM

The cross sections of the NMs were prepared by FIB milling normal to the substrate surface and investigated by ADF-STEM in a probe corrected FEI Titan 60-300 keV microscope operated at 300 keV. The elemental maps were obtained by using an EELS coupled to a Tecnai F20 microscope.

8.5.4 Contacting

Conctacts were patterned by e-beam lithography followed by dual-angle evaporation of 14/80 nm of Cr/Au for good side-wall coverage. Before metallization, an O_2 plasma clean and a 6 min ammonium polysulfide etch at 40 °C were used to ensure a clean, oxide-free contact [87].

8.5.5 Quantum Transport Model

The conductance of the NW is described as

$$\Delta G = -\frac{2e^2}{hL}\left(\frac{1}{l_\varphi^2} + \frac{1}{l_B^2}\right)^{-1/2}, \tag{25}$$

where L is the spacing between the contacts and l_B is the magnetic dephasing length given by $l_B = \sqrt{D\tau_B}$, with D as the diffusion constant ($D_{1D} = v_F l_e$ for 1D diffusion). In this limit, the magnetic dephasing time τ_B is given by $\tau_B = 3l_m^4/W^2 D$, where $l_m = \sqrt{\hbar/eB}$ is the magnetic length [95][96][97].

8.5.6 GaAs Capping

After the growth of the NW/NM heterostructures, a 30 nm GaAs cap was deposited in situ by MBE at 400 °C. In the middle of this GaAs cap, the In shutter was opened for 10 s, making a few-monolayer insertion of $In_{0.16}Ga_{0.84}As$, indicating the midpoint of the GaAs cap. The NW/NM heterostructures were then coated with a 110 nm GaAs layer [98] using ion-beam sputtering at 9 kV and 7.5 mA for 1 h. The capping layer protected the sample from damage caused by the ion beam during FIB.

8.5.7 APT

A standard lift-out method [98][99] was performed in a FEI Helios dual-beam FIB microscope with a micromanipulator and the as-prepared wedge-shaped samples were welded onto Si microposts. Finally, the needle-shaped APT specimens were obtained by ion-beam annular milling. APT was performed with a local-electrode atom-probe (LEAP) 4000X Si tomograph (Cameca, Madison, WI) at a sample temperature of 40 K and a background pressure of 3×10^{-11} Torr. An ultraviolet focused laser with a wavelength of 355 nm was used to evaporate the sample atoms into ions, at a pulse rate of 250 kHz and detection rate of 0.7 %. The pulse energy was gradually changed from 1.2 pJ to 0.8 pJ during the evaporation process. The data was recontructed using IVAS 3.8.1 to provide a 3D composition profile. SEM images of the nanotips taken in the FIB were used to guide the choices of the reconstruction parameters.

8.6 Supporting Information

8.6.1 Growth Details

The InAs NWs were grown by MBE on top of defect-free GaAs NMs. The growth of the NMs was performed according to an approach published previously, using selective area epitaxy [51]. Following the growth of the GaAs NMs at 630 °C, the substrate temperature was decreased to 540 °C and InAs was overgrown on top of the GaAs NMs. During the InAs growth, an arsenic flux of 8×10^{-6} Torr was used along with an indium rate of 0.2 Å/s. This was typically grown for 200 s, yielding a nominal depositied InAs thickness of 4 nm.

8.6.2 Temperature Dependence of InAs

As a first step during the growth optimization, two temperature series were performed. Some representative SEM images from these series are shown below. Here, we see that at low temperatures the InAs grows as clusters on the sides/edges of the membrane rather than as a single coherent wire. This side growth is possibly due to the fact that at low temperatures the adatoms have shorter diffusion lengths and, thus, are not able to find the optimal (lowest energy) positions, i.e. on the vertex. As the temperature is increased, the InAs islands begin to merge and a coherent nanowire begins to form above 530 °C.

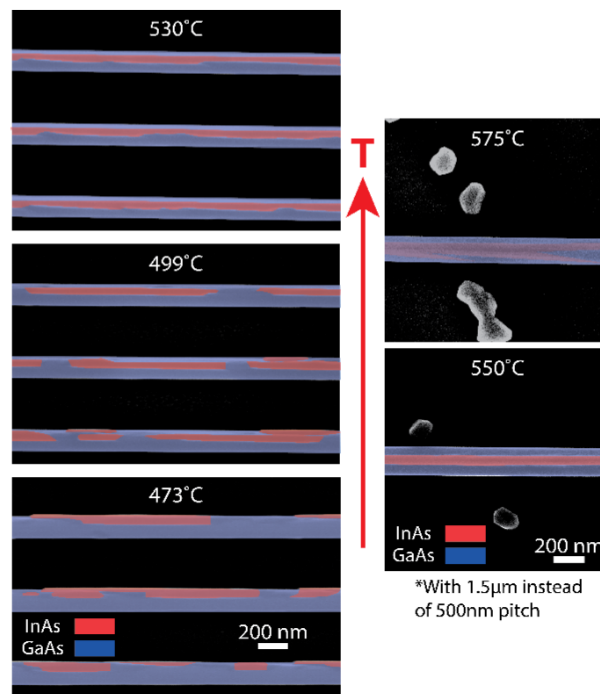

Figure 45: Temperature Dependence on InAs Growth Top-view SEM images showing temperature dependence of InAs growth on top of GaAs NMs. False-colored to show InAs islands as confirmed by energy-dispersive spectroscopy (EDS) measurements [102].

In a second series, on a substrate with NM pitches of 1500 μm, the growth temperature was increased further to observe the limit of the NW growth. At temperatures above about 550 °C, the InAs no longer grows on the NMs. The optimal growth temperature for achieving continuous coherent InAs NWs has, therefore, been found to be in the range of 540-550 °C.

8.6.3 Width/Pitch Dependence of InAs

The influence of the GaAs NM geometry on the nanowire growth was also explored on a single substrate grown at 530 °C. This comparison is shown below. From this analysis, we see that

thinner membranes stabilize the nanowire, making it more uniform. Increasing the pitch also improves the uniformity of the InAs NWs, though this is likely due to the fact that the NMs are thinner at larger pitches. NMs at larger pitches, due to less efficient arsenic capture, grow more slowly in, both, height and width. The optimal NM geometry is, therefore, achieved at large pitches (>1 μm) with mask openings as thin as possible, in order to achieve very thin GaAs NMs. For sufficiently thin NMs, the InAs covers the whole top surface of the GaAs NM and grows as a single NW with uniform thickness.

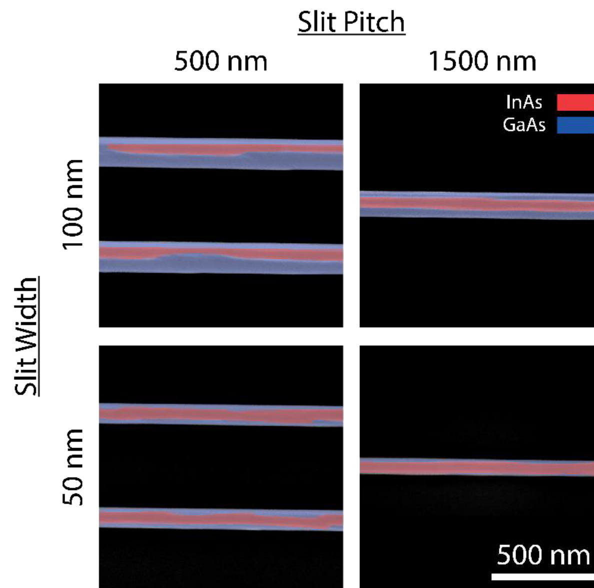

Figure 46: Geometry Dependence on InAs Growth Top-view SEM image comparison of InAs NW coverage of the GaAs NMs for various pitches and widths of the openings in the SiO_2 mask. The InAs/GaAs has been false-colored for visibility [102].

8.6.4 Raman Spectroscopy

Raman spectroscopy was performed on an InAs/GaAs device, in order to measure strain. This was performed using 488 nm laser excitation at a power of 200 μW and 1 μm spot size. A representative spectrum is shown below, where five main peaks can be distinguished and are summarized in the table that follows.

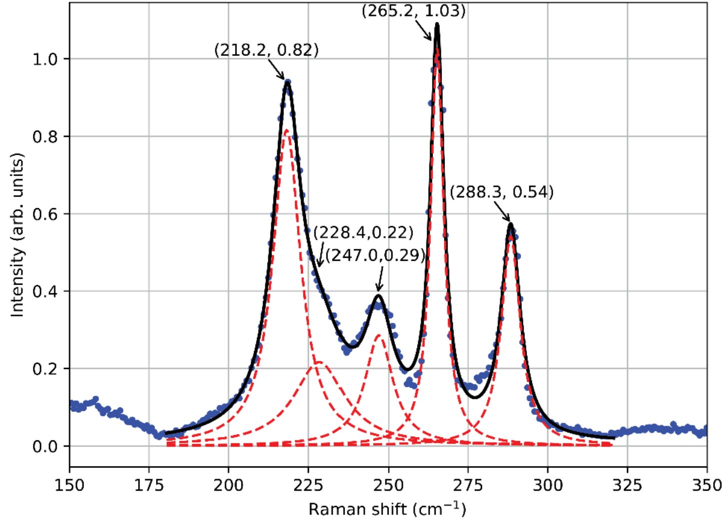

Figure 47: Raman Spectrum of InAs NW on GaAs NM [102]

Peak Name	Expected	Found
InAs TO	217.8 cm^{-1}	218.2 cm^{-1}
InAs SO [1]	240.0 cm^{-1} (bulk) 226.6 cm^{-1} (60 nm NW)	228.4 cm^{-1}
InAs LO	233.9 cm^{-1} 240.2 cm^{-1} [2]	247.0 cm^{-1}
GaAs TO	267.7 cm^{-1}	265.2 cm^{-1}
GaAs LO	291.2 cm^{-1}	288.3 cm^{-1}

Figure 48: Table of expected and measured Raman peaks [100][101][102]

Here, the expected SO phono peak was calculated assuming a cylindrical InAs nanowire with a diameter of 30 nm [101]. From the table, it can be seen that most peaks are measured within about 4 cm^{-1} of the expected frequency. However, the InAs LO peak shows a significant shift of 7 cm^{-1} due to strain [103]. Additionally, the shape of the LO phonon peak is broader than the expected Lorentzian fit, which we take as evidence of inhomogeneous broadening due to inhomogeneous strain that is also seen in finite differences simulations below.

8.6.5 Strain Simulations

The strain and electrical properties of the InAs nanowires were simulated using nextnano^3 (v1.9.2), a Schrödinger-Poisson-current finite differences solver [104]. The simulation was set up allowing for relaxation of the structure into the air spaces around the NW/NM. An unstrained GaAs substrate was imposed on the system at the base of the simulation.

The resulting strain tensor maps are shown below. It can be seen that the strain in the InAs nanowire is about 2-3 % on average. This agrees well with what was seen in HR-STEM GPA and Raman spectroscopy.

Note that, while the actual GaAs NMs are hundreds of nanometers tall, the simulations used a 50 nm tall NM to reduce the computational expense. This approximation is justified because, as seen in the simulations, below about 30 nm from the top of the NM, there is nearly no strain remaining in the GaAs NM.

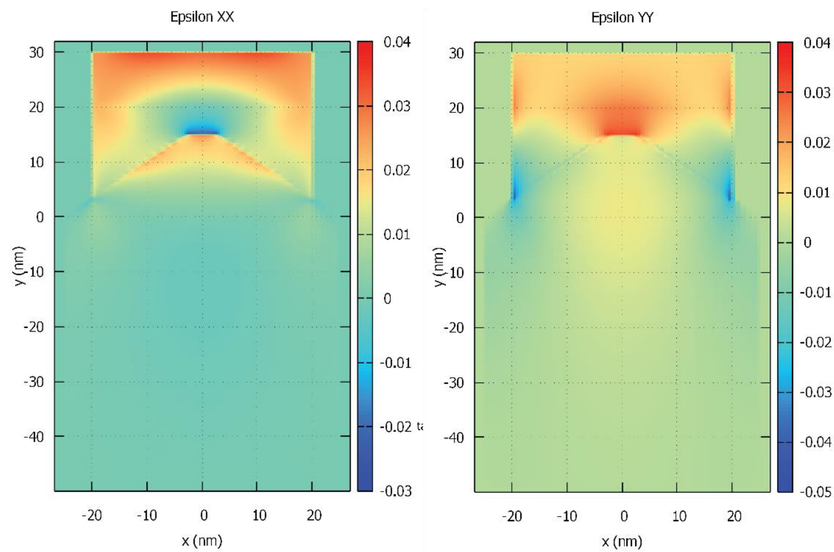

Figure 49: Simulations of strain tensor in x and y directions [102]

8.6.6 Growth Model

We provide a model to explain the preferential accumulation of InAs on the top ridge of the NM. Consider the NM/NW geometry shown below in the cross-sectional view perpendicular to the NM:

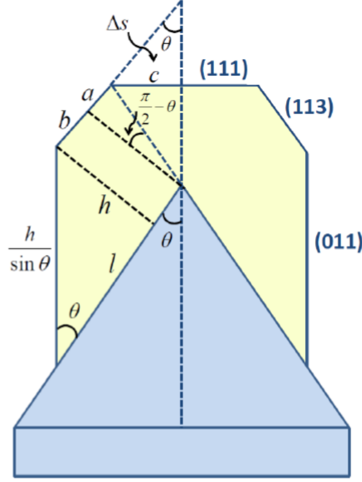

Figure 50: NW model geometry System geometry showing the geometrical parameters used in modelling the free energy of forming the InAs NW [102].

We assume that the InAs NW facets are composed of vertical, horizontal, and inclined facets of the (011), (111), and (113) families, respectively, and that the inclined NW facets are replaced by the horizontal facets at the crossing point of the initial NM facets with the inclined NW facets, as suggested by Figure 21 in the section **Nanomembranes as a Platform**. From geometrical considerations, we have $a = h\cot 2\theta$ and $b = l - h\cot\theta$, with θ as the taper angle of the NM, hence

$$b + a = l - h(\cot\theta - \cot 2\theta). \tag{26}$$

The (131) facet of the InAs of width $b+a$ and surface energy $\gamma_{InAs}^{(131)}$ replaces the initial facet of the GaAs NM of width l and surface energy $\gamma_{GaAs}^{(131)}$. Additionally, the NW formation creates the InAs-GaAs interface of width l and interfacial energy $\gamma_{InAs-GaAs}^{(131)}$. We also create the vertical facet of height $h/\sin\theta$ having the surface energy $\gamma_{InAs}^{(011)}$, and the horizontal facet of width c and surface energy $\gamma_{InAs}^{(111)}$. From geometrical considerations,

$$c = h\frac{\sin\theta}{\sin 2\theta}. \tag{27}$$

Summarizing all these surface energy terms and using $\cot 2\theta = (1/2)(\cot\theta - \tan\theta)$ and $\sin 2\theta = 2\sin\theta\cos\theta$ in (8) and (9), respectively, the surface energy change per length $2d$ (where

d is the length of the initial NM) equals

$$\Delta F_{surf} = \left[\gamma^{(131)}_{InAs-GaAs} + \gamma^{(131)}_{InAs} - \gamma^{(131)}_{GaAs}\right] l + \left[\frac{\gamma^{(011)}_{InAs}}{\sin\theta} - \frac{1}{2}\gamma^{(131)}_{InAs}(\tan\theta + \cot\theta) + \frac{\gamma^{(111)}_{InAs}}{2\cos\theta}\right] h. \quad (28)$$

Grouping the brackets into C_1 and C_2, we can write

$$F = C_1 l + C_2 h. \quad (29)$$

Clearly, the C_1 term gives the surface energy change in the (131) direction and is positive in the non-wetting and negative in the wetting cases, respectively. The C_2 term should always be positive and is associated with the InAs facets in contact with vapor.

The surface area of half the NW cross-section s equals the area of the parallelogram lh minus the area of the upper triangle Δs. The latter is given by $h^2/(8\sin\theta\cos\theta)$. Therefore,

$$s = lh - \frac{h^2}{8\sin\theta\cos\theta}, \quad (30)$$

where the second term is less than 10 % of the first one in our geometry and can be neglected in the first approximation.

To account for the effect of strain relaxation, we use the simplest formula [105][106][107]

$$\Delta G_{elastic} = \lambda\epsilon^2 V \frac{1}{1 + \alpha h/l}, \quad (31)$$

showing that the elastic energy (for the reduced strain ϵ due to dislocations) rapidly decreases ($\alpha \ll 1$) with increasing the aspect ration h/l with respect to the 2D film of the same volume V. Using $V \approx 2dlh$ and dividing it by the facet length $2d$, we arrive at the equation expressing the free energy of forming the InAs NW of width l and height h on top of the GaAs NM

$$\Delta F(l, h) = C_1 l + C_2 h + \frac{C_3 lh}{1 + \alpha h/l}. \quad (32)$$

This free energy is defined per unit length of the structure. The C_1 term gives the surface energy change upon covering the GaAs (131) facets with InAs and is proportional to the NW width l. The C_2 term ($C_2 > 0$) stands for the surface energy of all other InAs facets and is proportional to the NW height h. The last term gives the elastic energy of the InAs NW, proportional to the

NW cross-sectional area $s \approx lh$, with C_3 being the elastic energy per unit volume for the reduced mismatch [105], and α describing the stress relaxation with the aspect ratio h/l [105][106][107]. In fact, the NW cross-sectional area s equals $lh - \epsilon h^2$ due to the development of the horizontal (111) InAs top facet seen in Figure 21 in the section **Nanomembranes as a Platform**, but the ϵh^2 term is typically less than 10 % and we omit it to simplify the analysis. We also assume that the term associated with the dislocation energy is roughly the same for any aspect ratio, which should be valid for large enough volumes of deposited InAs, with the NW heights already well above the critical thickness for forming misfit dislocations (~1.2 nm) [106].

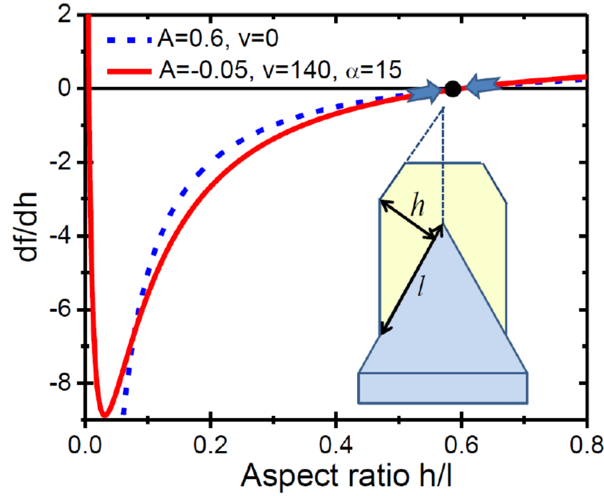

Figure 51: Change in free energy of formation with aspect ratio Graphs of the df/dh versus aspect ratio obtained in the non-wetting ($A > 0$) and wetting ($A < 0$) cases from equation (9). The zero point at $h/l \approx 0.6$ corresponds to the minimum free energy of forming the NW, because its derivative is negative for smaller and positive for larger aspect ratios. The real curve is expected to be the one in the wetting case, where the system surpasses an energetic barrier at a small x as in the Stranski-Krastanow growth. The value of $v = 140$ corresponds to the parameters of InAs with the reduced mismatch $\epsilon = 0.03$. The inset shows the geometry, the approximation $s \approx lh$ used in the calculations neglects the truncation of the full parallelogram in the top part of the NW [102].

To access the preferred shape of InAs on top of GaAs, we minimize equation (14) at a fixed $s = lh$, corresponding to a fixed volume of deoposited InAs [108]. Introducing $f = \Delta F/b$, the result is given by

$$\frac{df}{dh} = 1 - \frac{A}{x} - \frac{vs^{1/2}}{(1+\alpha x)^2}, \tag{33}$$

with $A = C_1/C_2$ as the normalized surface energy change in the (131) plane, $v = 2\alpha C_3 s^{1/2}/b$ as the strain-induced factor that increases with the amount of deposited InAs, and $x = l/h$ as the aspect ratio of the NW. The preferred aspect ratio is now defined by the stable zero point of df/dh, corresponding to the minimum free energy.

Figure 33 shows two possible cases with the preferred $x \approx 0.6$, as observed in Figure 21 in the section **Nanomembranes as a Platform**. We believe, however, that our GaAs/InAs system is initially wetting, that is, the surface energy favors 2D growth of InAs on GaAs, while 3D structures emerge only after the formation of a continuous wetting layer, as in the Stranski-Krastanow growth [107]. Therefore, the system is described by the solid line in Figure 33. In this case, reaching a high aspect ratio on the order of 0.6, which is necessary to form the NWs on top of the NMs, can only be due to strain relaxation and requires a high value of the strain-induced v factor of about 140. The c coefficient equals $\lambda\epsilon^2$, with $\lambda = 1.22 \times 10^{11}$ J/m^3 as the elastic modulus of InAs and ϵ as the reduced lattice mismatch. With the experimentally $\epsilon = 0.03$, this yields $v = 140$ at $\alpha = 15$ for a plausible value of $C_2 = 0.091$ J/m^2 [106].

8.6.7 TEM Compositional Line Scan

Looking at the EELS maps in more detail, a compositional map and line scan are shown in the figures below.

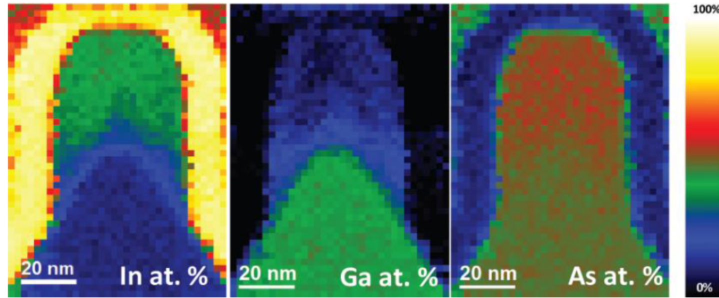

Figure 52: Detailed compositional maps Compositional map of InAs NM on GaAs NM for In, Ga, and As separately [102].

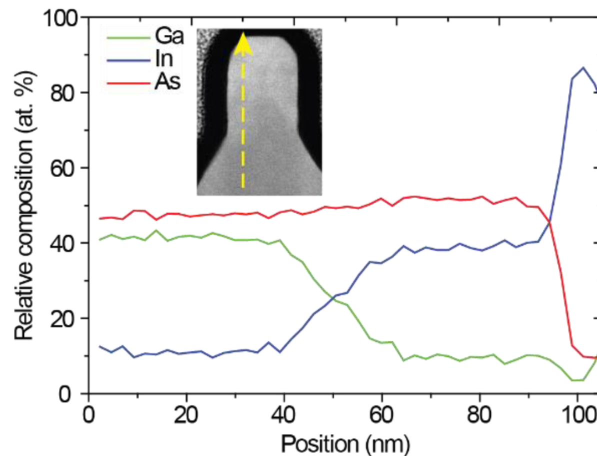

Figure 53: EELS line scans Compositional line scan from the GaAs NM into the InAs NW, showing relative concentrations of Ga, In, and As [102].

From the line scan, we first notice that the amount of indium in the GaAs region and gallium in the InAs region never goes below ~10 %. This is suspicious and is likely an artifact of the EELS measurement, possibly caused by indium/gallium adatom migration induced by the 200 keV electron beam. An additional contributor to the indium signal could be the titanium in the TiO_2 capping layer. The two elements are difficult to differentiate, as the titanium $L_{2,3}$ edges overlap with the indium $M_{4,5}$ edges.

The scan also shows a region between about 40 nm and 60 nm where gallium is present in the InAs NW. APT measurements have ruled out Ga cation diffusion during the FIB preparation process. Due to the 100 ° difference in growth temperature between the GaAs and InAs and the necessary cool-down period between the two growths, we do not expect any free gallium adatoms on the surface to contribute to the formation of this InGaAs region. Rather, it is likely that stress drives diffusion of some gallium atoms from the NM into the InAs NW during NW growth to accomodate the high lattice mismatch. This observation suggests such strain might be used to overcome the miscibility gap that is present in unstrained $In_xGa_{(1-x)}As$ below about 800 K [109][110].

8.6.8 InAs Crystal Quality

The crystal quality of the InAs NWs were further assessed by TEM imaging from the side of a GaAs/InAs NM/NW structure. Figure 36 **a** provides an example atomic resolution ADF-STEM analysis from a roughly 70 × 70 nm^2 region near the base of the InAs NW. Geometrical phase analysis (GPA) of (-1-1-1) dilatation (see Figure 36 **b**) reveals the presence of a double twin that appears to originate at the InAs/GaAs interface and propagates through the InAs layer.

The GPA structural map of the (-1-11) planes in Figure 36 **c** allows us to identify misfit dislocations, highlighted in red. Figure 36 **d** applies a rotation filter that further highlights these misfit dislocations. The appearance of misfit dislocations in the axial direction, along the NW, is expected because the strain can not be as easily relaxed compared with the radial case. This is believed to be the reason that no misfit dislocations were observed in the transversal atomic resolution ADF-STEM cross sections. On the other hand, in the longitudinal cross-section, one can count seven misfit dislocations in this roughly 70 nm-long region. Using this value as an initial guess, we estimate that this structure has on the order of 100 misfit dislocations per micrometer.

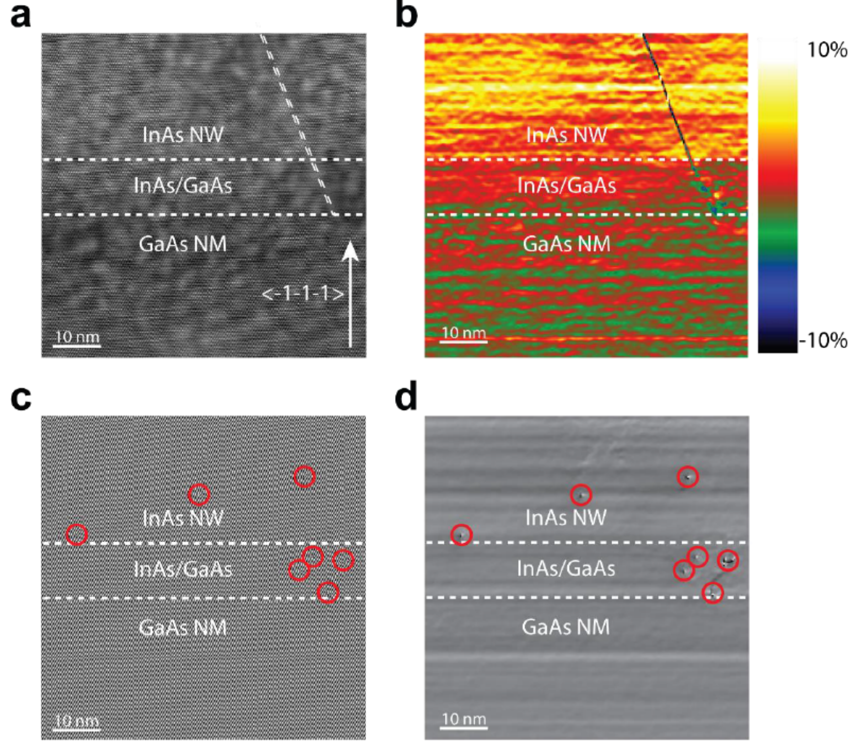

Figure 54: TEM defect analysis (a) Atomic resolution ADF-STEM image taken from a <0-11> zone axis at the base of the InAs NW on a GaAs NM showing two twins originating at the heterojunction and propagating into the InAs NW. **(b)** GPA analysis of image in **(a)** looking at dilation of (-1-1-1) planes. Here, the twin is clearly visible and the color contrast enables us to distinguish the InAs from the GaAs region. **(c)** Structural map of (-1-11) planes in image **(a)** allowing us to see the presence of misfit dislocations, highlighted in red. **(d)** Rotation filter of (-1-11) planes from image **(a)**, allowing us to more accurately distinguish misfit dislocations [102].

8.6.9 Magnetotransport Model

The conductivity dependence on magnetic field was fit with the following weak localization model for the quantum correction to the classical conductivity in the quasi 1D diffusive limit [95][111]

$$\Delta G = -\frac{2e^2}{hL}\left(\frac{1}{l_\varphi^2} + \frac{1}{l_B^2}\right)^{-1/2}, \tag{34}$$

where L is the length of the wire between contacts, l_φ the phase coherence length, and l_B the magnetic dephasing length. l_B relates to the magnetic relaxation time τ_B as

$$l_B = \sqrt{D\tau_B}, \tag{35}$$

with $D = v_F l_e$ for 1D wires. In our system, in the diffusive limit where $l_e \ll W$, with W the

conducting channel width, and $W \ll l_\varphi$ (quasi-1D transport), τ_B is given as [95][96][97][112]

$$\tau_B = \frac{3 l_m^4}{W^2 D}, \tag{36}$$

where $l_m = \sqrt{\hbar/eB}$. This regime constrains l_e to maximally a few nanometers, which is in good agreement with the expected spacing between dopants. We estimate from a 3D doping concentration of 10^{27} per cubic meter a 1D concentration of 10^9 per meter, thus roughly one dopant per nanometer. The fits for the data yielded the values shown in the following table for l_φ in this limit.

Bias [mV]	l_φ [nm]	$\pm$ [nm]
0	134	4
5	97	2
10	84	2
15	73	2
20	66	2

The accuracy of the fits for l_φ in this diffusive limit need to be taken with a degree of caution. When spin-orbit length, l_{so}, and mean free path, l_e, are included into the formalism, one has [113]

$$\Delta G = -\frac{e^2}{hL}\left[3\left(\frac{1}{l_\varphi^2} + \frac{4}{3l_{so}^2} + \frac{1}{l_B^2}\right)^{-1/2} - \left(\frac{1}{l_\varphi^2} + \frac{1}{l_B^2}\right)^{-1/2} - 3\left(\frac{1}{l_\varphi^2} + \frac{4}{3l_{so}^2} + \frac{1}{l_e^2} + \frac{1}{l_B^2}\right)^{-1/2} + \left(\frac{1}{l_\varphi^2} + \frac{1}{l_e^2} + \frac{1}{l_B^2}\right)^{-1/2}\right]. \tag{37}$$

The data was fit for a range of values for l_{so}, which result in slightly varying l_φ between 130 and 160 nm, that fall off quickly with addition of voltage bias. When $l_{so} \to \inf$, the diffusive limit is recovered, as expected. The spin-orbit strength extracted from these fits is somewhat weak, corresponding to larger spin-orbit lengths than otherwise known from InAs [114][115]. This is likely due to a combination of the gallium content in the wires and motional narrowing in the diffusive limit, with a mean free path on the order of nanometers. The complete lack of weak-antilocalization in the data is consistent with very weak spin-orbit interaction, thus, a large l_{so}. A 2D conductance map, from which the above tabled data comes, is displayed below, which

shows the dependence of conductivity on, both, magnetic field and applied DC bias.

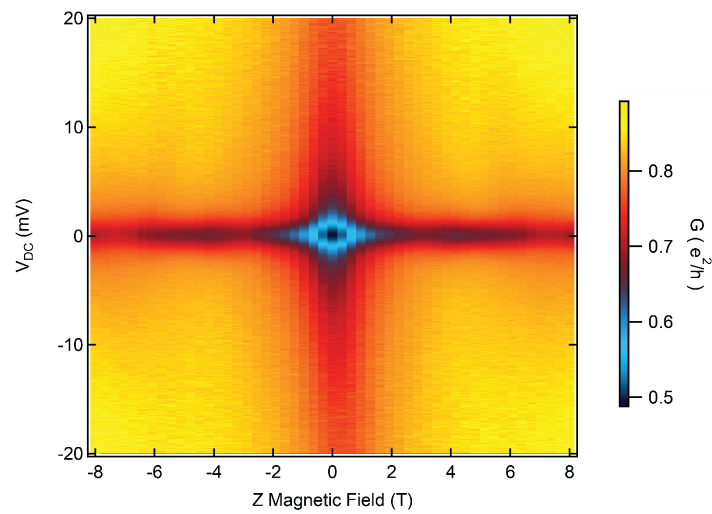

Figure 55: Conductivity map as a function of magnetic field and bias voltage Color scaling is differential conductance in units of e^2/h. The decrease in conductance around zero magnetic field is clearly manifested [102].

9 Remote Doping of Scalable Nanowire Branches

M. Friedl*[1], K. Cerveny*[2], C. Huang[3] D. Dede[1], M. Samani[2], M. O. Hill[3], N. Morgan[1], W. Kim[1] L. Güniat[1] J. Segura-Ruiz[4], L. J. Lauhon[3], D. M. Zumbühl[2], and A. Fontcuberta i Morral[1]

* Equal contribution

[1] Laboratoire des Matériaux Semiconducteurs, École Polytechnique Fédérale de Lausanne, EPFL, 1015 Lausanne, Swizterland

[2] Department of Physics, University of Basel, Klingelbergstrasse 82, CH-4056 Basel, Switzerland

[3] Department of Materials Science and Engineering, Northwestern University, Evanston, Illinois 60208, United States

[4] ESRF: the European Synchrotron, Grenoble 38043, France

This chapter was published in *Nano Lett.* **20**, 3577-3584 (2020).

9.1 Abstract

Selective-area epitaxy provides a path toward high crystal quality, scalable, complex nanowire networks. These high-quality networks could be used in topological quantum computing as well as in ultrafast photodetection schemes. Control of the carrier density and mean free path in these devices is key for all of these applications. Factors that affect the mean free path includescattering by surfaces, donors, defects, and impurities. Here, we demonstratehow to reduce donor scattering in InGaAs nanowire networks by adopting a remote-doping strategy. Low-temperature magnetotransport measurements indicate weak anti-localization - a signature of strong spin-orbit interaction - across a nanowire Y-junction. This work serves as a blueprint for achieving remotely doped, ultraclean, and scalable nanowire networks for quantum technologies.

9.2 Introduction

In the last two decades, semiconductor nanowires (NWs) [168] have opened multiple new perspectives in a wide variety of applications including photovoltaics [169][170][171][172][173], photodetectors [174][175][176][177], lasers [178][179][180][181][182], single-photon emitters [183][184], photoelectrochemistry [185], nanoscale electronics [186], and research into topological quantum computing [187][188][189][190][191]. While most NW fabrication approaches result in free-standing structures, selective-area epitaxy (SAE) has recently been revived for the fabrication of horizontal NW assemblies that can be directly contacted on a wafer [192][193]. SAE has thus been used to obtain lateral III-V NWs, with high NW crystal quality and with scalability unmatched by any other bottom-up NW growth method. The ability of SAE NWs to be grown into NW networks [194], and the relative ease with which they can be further processed directly on the original substrate, makes them extremely attractive for use in experiments exploring topological quantum transport physics [195][196][197][198][199].

It has generally been reported that surface scattering in NWs reduces carrier mean free paths which, by extension, also reduces carrier mobility with respect to their bulk conterparts. This is especially pertinent in InAs NWs, where the surface Fermi level pinning results in most of the conduction occurring at the surface [198]. Room-temperature electrically measured mobilities for undoped, vertically grown InAs NWs thus fall in the range of ∼20-3000 $cm^2/(Vs)$ [199][200][201][202][203]. Noncontact measurement techniques such as THz pump-probe spectroscopy report slightly higher mobilities of ∼4000-6000 $cm^2/(Vs)$ due to the smaller length scale of the assessement and a possible selection bias (higher mobility sections contributing more to the signal) [203][204][205]. Still, mobilities remain significantly lower than the reported values for thin films of around 30,000 $cm^2/(Vs)$ [206]. InGaAs nanowires with In:Ga ratios around 50%, on the other hand, have been reported with somewhat lower mobilities ranging from ∼500 to 1500 $cm^2/(Vs)$ [207][208].

Over the years, modulation doping has proven to be a staple technique to many applications employing high-performance semiconductor heterostructures. This technique allows for the creations of two-dimensional electron gases (2DEGs) with high carrier concentration combined with extremely high mobilities. From groundbreaking scientific discoveries such as the integer and fractional quantum Hall effects [209][210][211], and enabling novel concepts such as topological qubits [212][213][214][215], to high-power applications using high electron mobility

transistors (HEMTs) [216][217], a wide range of fields have benefited and are continuing to benefit from remotely doped 2DEG heterstructure schemes. With current knowledge and modern epitaxy techniques, state-of-the-art 2DEG devices can achieve mobilities regularly exceeding 10^7 $cm^2/(Vs)$ [218][219]. Similarly to bulk, direct doping of NWs reduces carrier mobilities due to ionized dopant scattering. To circument this carrier scattering mechanism, vertically grown free-standing GaAs NWs with a remote-doping design exhibit both high carrier densities and high mobility [220][221][222][223].

In this work, we demonstrate the growth of quasi-1D InGaAs NW heterostructures hosting coherent transport by combining remote doping with SAE. The InGaAs NWs are obtained on a GaAs nanomembrane (NM) buffer in which the doping is located. The band alignment naturally results in the localization of electrons in the region with higher indium content (and lower bandgap). Improved electrical transport is demonstrated by low-temperature field-effect and magneto-transport measurements across InGaAs NW Y-branches, demonstrating high-quality NW junctions. This research thus lays the groundwork for future exploitation of remote-doping schemes in scalable NW networks, including materials beyond InGaAs.

9.3 Growth

Remotely doped InGaAs NWs were grown on top of GaAs NM buffers using a SAE approach, as depicted in Figure 1a A GaAs (111)B substrate was covered by the SiO_2 mask to achieve high growth selectivity. The SiO_2 mask was then patterned with stripes along the three equivalent $\langle 11\overline{2} \rangle$ directions on the substrate using e-beam lithography and reactive ion etching. The resist was stripped with an O_2 plasma, and the substrate was etched in a dilute buffered HF solution before being loaded into the molecular beam epitaxy (MBE) cluster for growth to ensure an ultraclean surface.

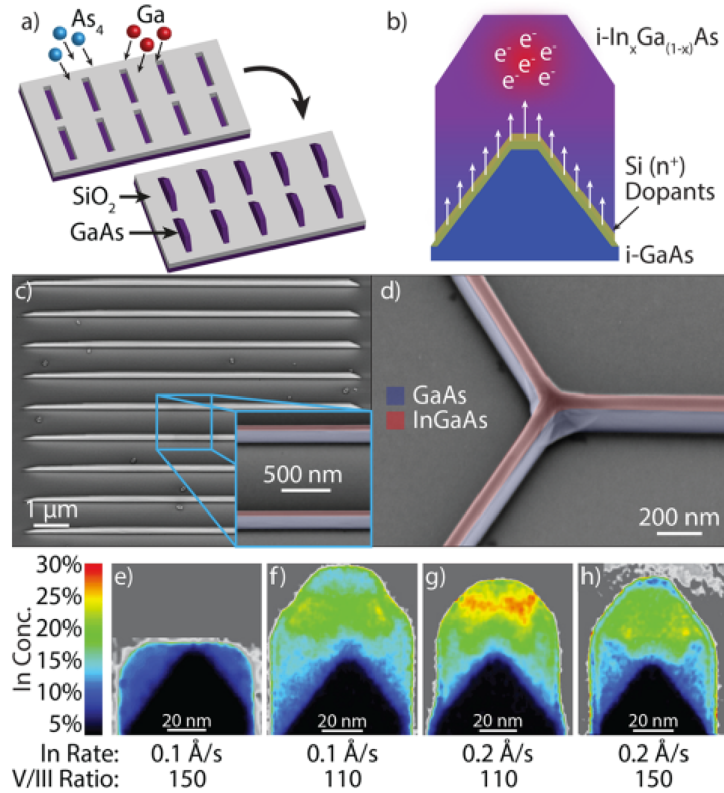

Figure 56: Figure 1. (a) Illustration of the SAE growth process. (b) Diagram showing the desired doping profile for remotely doped InGaAs NWs on GaAs NMs. (c) Tilted SEM image of an array of NWs after MBE growth. (d) Close-up tilted SEM image of a Y-junction showing uniform coalescence of InGaAs NWs. (e-h) Elemental maps of In concentration taken with STEM EDS on NW cross sections showing the dependence of growth conditions on NW composition.

Figure 1b corresponds to the general scheme of the structures in this work. Silicon dopants are introduced at a distance from the InGaAs channel. We expect carriers to localize into the lower-bandgap NW region. As a result, the NWs benefit from an increased carrier concentration thanks to the extrinsic dopants, while ionized impurity scattering is limited due to the physical separation between the doped and transport regions.

Figure1c shows a representative scanning electron microscopy (SEM) image of the remotely doped NW structures. We recognize a high degree of uniformity in both the buffer NMs and the NWs. Similarly, as show in Figure 1d, Y-branched structures result from the merging of NWs growing in three equivalent directions [192]. These branched structures exhibit a high degree of NW uniformity, which is further confirmed by X-ray fluorescence (XRF) measurements performed at the ID16B beamline of the European Synchrotron Radiation Facility (ESRF) shown in the Supporting information.

In-Ga intermixing is commonly observed at the interface between InAs and GaAs [224].

This is also the case for InAs grown on GaAs buffer NMs. In a previous study, we demonstrated InGaAs NWs with a relatively low In content [192]. Increasing the In content is key to enhancing spin-orbit interaction (SOI). In this context, we explored different growth conditions to increase the In concentration. In particular, we varied temperature along with In and As_4 fluxes. We present four representative samples iwth a variation in the In deposition rate and As_4 beam equivalent pressure (BEP). The composition was analyzed by performing elemental maps by scanning transmission electron microscopy (STEM) energy dispersive X-ray spectroscopy (EDS) on prepared cross sections. The resulting In concentration maps are shown in Figure 1e-h. Here, the atomic concentration of In is calculated as $C_{In}/(C_{In} + C_{Ga} + C_{As})$ with the maximum possible concentration being 50% for pure InAs. In Figure 1e, we see that an In rate of 0.1 Å/s and V/III ratio of 150 yields a self-terminating growth and a flat (111) top facet with an In concentration of ∼10% at the two upper corners of the structure. Decreasing the V/III ratio to 110, as shown in Figure 1f, results in a more pointed structure that does not self-terminate. This results in a larger amount of material being deposited and a maximum In concentration of ∼20%. Doubling the In deposition rate to 0.2 Å/s (while halving the growth time to keep the total deposited volume constant) gives a similarly shaped structure; however, now the peak In concentration is ∼25%, as shown in Figure 1g. Finally, Figure 1h shows the result of also increasing the V/III ratio to 150 with an In deposition rate of 0.2 Å/s. We observe a structure very similar to Figure 1f with a pointed shape and a maximum In concentration of 20%.

We, therefore, observe that a higher In flux yields an increaesd In concentration in the NW, up to about 25%. On the other hand, at low In rates, In concentrations of only 10% or less are observed. The InAs growth temperatures are relatively low for solid-phase diffusion which is typically only observed above 750 °C [225][226][227]. The In-Ga intermixing could instead be mediated by surface adatom diffusion during growth. This is a thermodynamically driven effect which, consequently, can be suppressed at higher deposition rates where the system approaches a kinetic regime [228].

Also, the V/III ratio is known to affect the atomic surface reconstruction which in turn affects facet-dependent growth rates and the resulting shape [229][230]. In Figure 1e, at high V/III ratios and low growth rates, InGaAs grows to form a flat (111)B top facet, after which NW growth stops. This suggests that desorption of In species from this flat top facet is higher than the incoming flux. However, if the In rate is increased, as in Figure 1h, then NW growth is re-

established which can be explained by the fact that the increased incoming flux becomes greater than the desorbing flux, thus continuing NW growth. Similarly, if the V/III ratio is cecreased, as in Figure 1f, a similar effect is achieved. This, therefore, suggests that, at the higher V/III ratio, the abundance of As atoms plays a role in inhibiting growth on the (111)B top facet. Thus, higher In rates and lower V/III ratios should be pursued to reduce Ga intermixing in the NW. This result is at least partially supported by recent reports on (100) GaAs substrates where very low V/III ratios are used to grow pure InAs NWs on top of GaAs(Sb) buffers [193].

The highest In concentration was about 25% absolute, corresponding to $In_{0.5}Ga_{0.5}As$. This sample was obtained with a high In flux and lower V/III ratio. These conditions were kept for the rest of the structures presented in this study.

9.4 Atom-Probe Tomography

As the silicon dopant concentration was well below the detection limits of STEM EDS, atom probe tomography (APT) was used as a technique to image the three-dimensional distribution of the dopants in the structure.

APT was used to analyze the distribution of the dopants in the nanowire heterostructures, as shown in Figure 2 [192][231]. Samples were prepared by lift-out and annular milling using a focused ion beam to isolate the nanowire region for analysis [232][233]. Details of the specimen preparation and the APT analysis conditions can be found in the Experimental Section. Figure 2a shows the APT reconstruction of the region indicated by the dashed white line in the schematic. Silicon dopants were mostly detected on the GaAs top facet, as shown in Figure S8. The analysis here focuses on the subregion indicated in the dashed black line. To accurately measure the Si dopant distribution despite this artifact, a proximity histogram [234] was generated, as show in Figure 2b on either side of a 16% In mole fraction isosurface. The Si concentration peaks below the NM-NW interface, as expected from the doping scheme. APT analysis of two additional heterostructures (see the Supporting Information) found a similar distribution of Si concentrated at the NM-NW boundary. Moving 5-10 nm away from the interface, Si was not detected above the noise level (see Figure S8). The upper bounds on the Si concentration in the upper and lower regions away from the interface are 2×10^{18} and 7×10^{18} cm^{-3}, respectively, as indicated by dashed lines in Figure 2b. These measurements demonstrate that Si was incorporated at a distance from the InGaAs transport channel, validating the remote doping from the compositional

mapping point of view.

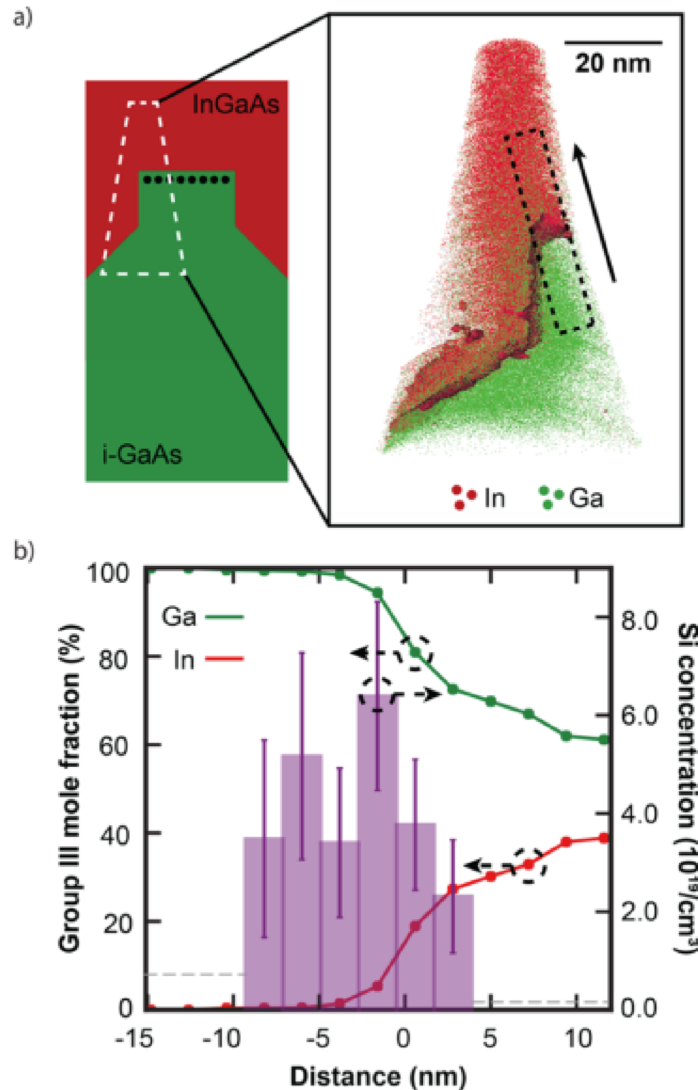

Figure 57: Figure 2. (a) APT reconstruction of an InGaAs NW on a GaAs NM. The white dashed line in the schematic indicates the region analyzed by APT. Ga and In atoms are shown in green and red, respectively. As atoms are omitted for clarity. The NM-NW boundary is rendered with an isoconcentration surface of 5% In mole fraction. (b) Proximity histogram across the NM-NW interface showing the Si dopant distribution. Gray dashed lines show the upper bounds on Si concentration in regions away from the interface, where Si counts were not above the noise level. The isoconcentration surface of 16% In mole fraction is at 0 nm as a reference.

9.5 Magnetotransport

NW structures were electrically contacted for four-point measurements on all three arms of the Y-junctions (see the Experimental Section). A top gate was fabricated by first covering the junction with a 40 nm thick HfO_2 gate oxide by atomic layer deposition (ALD) followed by metal evaporation. An SEM image of an electrical device illustrating the overall design is displayed in Figure 3a. A false-colored cross-sectional focused ion beam (FIB) STEM image is displayed

in Figure 3b with the identification of the different layers of the device. It is important to note that the metallic contact layers are continuous through the whole high-aspect-ratio structure, as a result of the dual-angle evaporation.

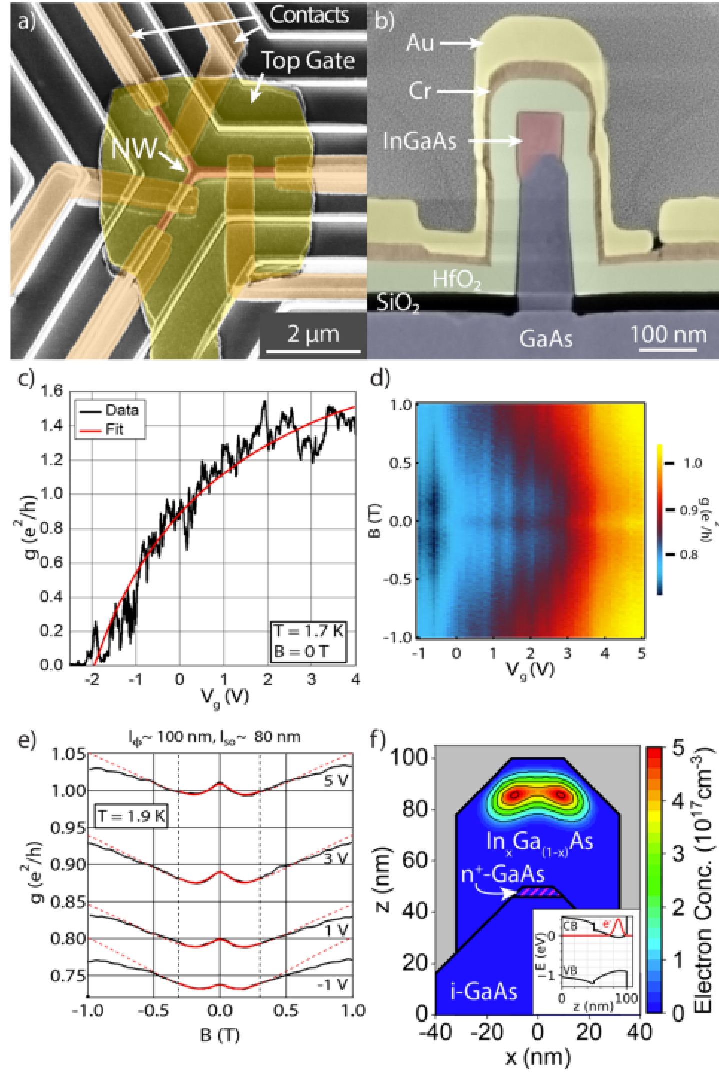

Figure 58: Figure 3. (a) False-colored SEM image of a fabricated electrical device showing three pairs of contacts to enable four-point measurements and a global top gate. (b) False-colored cross-sectional STEM high-angle annular dark-field (HAADF) image showing the layers in a fabricated electrical device. (c) Differential conductance as a function of top gate voltage V_g, from which the field-effect mobility $\mu = \sim 480 \pm 50$ cm^2/(Vs), the conduction threshold V_{th} = -1.9 ± 0.2 V, and the contact resistance R_s = 12.2 ± 0.6 kΩ were extracted. (d) Differential conductance plot (color scale) as a function of magnetic field perpendicular to the substrate and top gate voltage with $V_{g,AC}$ = 200 mV (peak-to-peak) oscillation added. (e) Magnetoconductance cuts (black) with fits (red) as labeled, exhibiting clear WAL. The WAL model is valid between the dashed vertical lines, which also denote the fitting range (solid red). Theory curves are extended to the full B-range (dashed red). Over the full gate range, average values of l_φ = 100 ± 20 nm and l_{so} = 80 ± 20 nm, where the mean free path l_e = 20 nm was held fixed here. (f) Finite element simulation in nextnano of remotely doped structure obtained from APT measurements showing an electron distribution in the InGaAs NW which is spatially separated from the n-type silicon dopants and disordered GaAs/InGaAs interface. Inset: band structure cut along x = 0 nm with electron concentration overlaid in red.

The samples were then cooled down and electrically characterized at cryogenic temperature.

The conductance as a function of top gate voltage V_g is shown in Figure 3c in units of e^2/h, giving very similar results over all pairs of arms of the Y-junctions. From this measurement, the field-effect mobility is extracted using [235]

$$G(V_g) = \left(R_s + \frac{L^2}{\mu C(V_g - V_{th})} \right)^{-1} \tag{38}$$

with $L = 600$ nm being the length of the channel, $\epsilon_0 = 8.854 \times 10^{12}$ F/m, $\epsilon_{HfO_2} = 6.5$, [193] and C the gate capacitance. The contact resistance R_s, the conductance threshold voltage V_{th}, and the mobility μ are the fit parameters. The gate capacitance was estimated numerically using a finite element simulation in COMSOL, though similar values were calculated analytically using coaxial cable or parallel plate capacitor models. The contribution of the GaAs NM to the electrical transport is negligible, as already previously demonstrated [192].

We extract a field-effect mobility μ of $\sim$480 $\pm$ 50 $\text{cm}^2/(\text{Vs})$. At zero gate voltage, this corresponds to a mean free path l_e of $\sim$300 $\pm$ 30 nm in the 1D limit and $\sim$20 $\pm$ 5 nm in the 3D limit. The associated Fermi wavelengths λ_F are smaller than the effective width of the nanowire, suggesting that a 3D approach is appropriate. Given a rather high carrier density from the capacitance models, the conductance of $\sim$1 e^2/h corresponds to partial transmission of many transverse quantum modes, corresponding to a multimode conductor. This mean free path l_e represents a significant improvement over previous work [192], where l_e was found to be limited by ionized dopant scattering on an $\sim$nm length scale.

Reported electron mobility values in free-standing InGaAs NWs at room temperature range between 500 and 1500 $\text{cm}^2/(\text{Vs})$, for similar In content [207][208]. We associate this difference, in part, to the reduced diameter and the presence of strong surface and boudnary scattering at both the top surface and disordered GaAs/InGaAs interface. In addition, the presence of alloy scattering due to disorder, as evidenced by the STEM EDS investigations, is also likely to play a role in limiting mobility in this ternary system [236]. While our result is on the low end of this spectrum, we stress that our wires, grown by a SAE approach, enable scalability not achievable via standard growth techniques.

The magnetoconductance of the devices was then probed. Figure 3d and e displays the conductance as a function of the applied magnetic field B. Again, the results are independent of which Y-junction arms are used. The enhanced conductance at zero field indicates the presence of weak anti-localization (WAL), a hallmark signature of the SOI. WAL is the result of the ac-

cumulating spin precessions around momentum-dependent effective magnetic fields arising from spin-orbit coupling in the Dyakonov-Perel mechanism [237]. In the quasiclassical, clean limit [238][239][240][241]

$$\Delta G = -\frac{e^2}{hL}\left[3\left(\frac{1}{l_\varphi^2}+\frac{4}{3l_{so}^2}+\frac{1}{l_B^2}\right)^{-1/2} - \left(\frac{1}{l_\varphi^2}+\frac{1}{l_B^2}\right)^{-1/2} - 3\left(\frac{1}{l_\varphi^2}+\frac{4}{3l_{so}^2}+\frac{1}{l_e^2}+\frac{1}{l_B^2}\right)^{-1/2} + \left(\frac{1}{l_\varphi^2}+\frac{1}{l_e^2}+\frac{1}{l_B^2}\right)^{-1/2}\right] \tag{39}$$

for a multimode quasi-1D wire, where the phase coherence length l_φ is exceeding the wire width W and $l_e \gg W$. Here, e is the electron charge, h is the Planck constant, l_{so} is the spin-orbit length, and l_B is the magnetic dephasing length, which in the clean limit $l_e \gg W$ is given by

$$l_B^2 = \frac{C_1 l_e l_m^4}{W^3} + \frac{C_2 l_e^2 l_m^2}{W^2} \tag{40}$$

where $l_m = \sqrt{\hbar/eB}$ is the magnetic length and $C_{1,2}$ are constants dependent on the type of boundary scattering [238]. Here, similar values were obtained in using both specular and diffusive boundary scattering. The coherence length, l_φ, is a measure for how far an electron will travel on average before having its phase randomized due to inelastic scattering events. The spin-orbit length, l_{so}, is the typical length for the spin to precess appreciably and is, thus, a key measure for the strength of the SOI, with a shorter l_{so} corresponding to stronger spin-orbit coupling. We mention here that our extracted mean free path falls outside the clear validity of either of the clean ($l_e \gg W$) or diffusive ($l_e \ll W$) limits. Thus, we have done the fits in both regimes (see the Supporting Information for details), giving very good agreement with the experiment. We obtain values of $l_\varphi \sim 100$ nm and $l_{so} \sim 80$ nm using both the clean and diffusive limits. For the clean regime fits, $l_e = 20$ nm was held fixed in order to extract l_ϕ and l_{so} unambiguously. The presence of WAL indicating strong SOI in the system is also a clear advance over previous results [192], in addition to the longer mean free path. Also, the coherence and spin-orbit parameters extracted here are very similar to other studies [193][194][213].

Both Dresselhaus and Rashba SOIs are key resources for topological quantum computation and spin qubits. Dresselhaus SOI, on the one hand, is due to a lack of crystal inversion symmetry.

NWs particularly those with low symmetry and/or large aspect ratio cross sections, can have a strong Dresselhaus SOI, as recently predicted [242]. Rashba SOI, on the other hand, is due to a breaking of structural inversion symmetry, often appearing at an interface or surface. Both types of SOI may be gate-controlled, i.e., by changing the electric field (Rashba) [243][244][245] or by gate-tuning the wave function asymmetry (Dresselhaus) [193][242]. Given the width of the present NWs, the estimated Dresselhaus contribution is negligible. We have measured the gate voltage dependence of the magnetoconductance. The resulting plot is show in Figure 3d. Universal conductance fluctuations and charge switchers can often obscure the results of the magnetoconductance. In order to mitigate this, we coupled an AC-oscillation to the top gate [244]. Using the model from eq 2 over the full gate voltage range, l_φ and l_{so} are found to be essentially independent of gate voltage (see Figures S5 and S6). This can be attributed to the wrap-around geometry of the gate, effectively shielding the NW from applied electric fields, while still allowing one to gate-tune the density (see Figure 3b). Thus, the WAL observed here is presumably due to the Rashba effect arising from built-in electic fields in the structure, such as gradients in the bandgap, presence of ionized dopants, or surface effects. In the Supporting Information, we give more details and a full analysis of the data with and without the AC oscillation.

9.6 Conclusion

We have demonstrated that remote doping of InGaAs NW networks grown by SAE is a promising approach to improving their quantum transport properties. Remote doping has enabled significant improvement of the key transport parameters such as the mean free path and SOI strength over previous bulk-doped NWs [192]. Together with increased In content lowering the band gap, the Y-junctions exhibit WAL, indicating strong SOI, which is a necessary ingredient for future applications in topological quantum computation. These measurements further serve as proof of the quality of the crystal across NW Y-junctions, and this work opens up new perpsectives into using this approach in networked quantum computing schemes.

9.7 Experimental Section

Growth. MBE growth was performed in a DCA P600 solid-source MBE chamber. Twenty-five nm of SiO_2 was deposited on GaAs (111)B substrates by plasma-enhanced chemical vapor

deposition (PEVCD). These were patterned by e-beam lithography using 35 nm of ZEP resist and etching in an SPTS APS dielectric etching tool employing SF_6 and CHF_3 chemistry. After resist stripping in an O_2 plasma, the samples were etched for 10 s in a highly dilute buffered HF solution to remove ∼5 nm of SiO_2 everywhere and smoothen the mask. Samples were then loaded and annealed at 400 °C for 2 h in a degassing chamber followed by 630 °C for 30 min in the growth chamber immediately before growth. The GaAs buffer NMs were grown at a temperature of 630 °C at an equivalent 2D GaAs growth rate of 1 Å/s with an arsenic BEP of 4 $\times 10^{-6}$ Torr. They were grown to an equivalent 2D thickness of 100 nm, resulting in structures with a height of ∼300 nm. Toward the end of the buffer growth, Si dopants were introduced for a short duration via a Si sublimation cell at a rate of 10^13 $cm^{-2}s^-1$ to achieve the desired doping profile, nominally 2 nm below the surface of the NM. After GaAs growth, the substrate temperature was decreased to 540 °C, while the As BEP was increased to 8×10^{-6} Torr for InAs deposition. The In flux corresponded to an InAs equivalent growth rate of 0.1 Å/s. The In flux was closed after the 2D equivalent grown thickness of 60 nm of InAs, and the sample was then cooled down under As flux.

STEM. Cross sections of the samples were prepared first in a FEI Nova 600 Nanolab dual-beam SEM/FIB tool before being loaded into a FEI Tecnai Osiris microscope operating at 200 keV in STEM mode. Elemental contrast was obtained by EDS thanks to four cryo-cooled Super-X silicon drift detectors (SDDs).

APT. To protect the sample from damage during FIB milling, the sample was coated with 120 nm of Ni using ion-beam sputtering at 9 kV and 7 mA. Then, a further protective Pt capping layer was deposited by ion beam induced deposition prior to lift-out using a FEI Helios dual-beam focued ion beam. Wedge-shaped lift-outs were welded onto Si microposts, and annular milling was used to isolate the region of interest within a needle-shaped tip with a diameter of 20-60 nm. APT analysis was perfored using a local-electrode atom-probe (LEAP) 5000 XS (CAMECA, Madison, WI) with a 355 nm wavelength laser under the following conditions: 250 kHz pulse rate 30 K background temperature, 2.5×10^{-11} Torr background pressure, and 0.4% target detection rate. An intial pulse energy of 3 pJ was used to evaporate through the surface oxides; pulses of 0.65-0.74 pJ were used in the region analyzed. APT data were reconstructed using IVAS 3.8.5 software. The tip profile method was applied, in which SEM images of the nanotips before analysis were used to determine the reconstructed radius as a function of analyzed depth.

Contacts and Electrical Measurements. The devices were cleaned with standard solvents, and the contacts were patterned with e-beam lithography, followed by an O_2 plasma cleaning. Before metallization, the samples were then exposed to an ammonium polysulfide (NH_4S_x) solution for 150 s to remove the native oxide [245]. Contacts were deposited by dual-angle evaporation of 14/50 nm of Cr/Au to achieve suitable sidewall coverage. Next, 40 nm of HfO_2 was deposited by ALD followed by another round of e-beam lithography and metallization to pattern the top gates. Finally, the sample was bonded into a chip carrier and measured using standard lock-in techniques in a variable temperature insert cryostat. Similar results were reproduced on another sample from the same wafer.

9.8 Supporting Information

9.8.1 1D Finite Element Simulations of Remote-Doping

1D finite element simulations were performed using the nextnano software package [246] to simulate the band structure and carrier concentration of remotely-doped template-assisted nanowire (NW) structures. A simulation of a GaAs nanomembrane (NM) with either a pure InAs NW or intermixed $In_{0.5}Ga_{0.5}As$ NW on top was performed, as shown in Figure S1

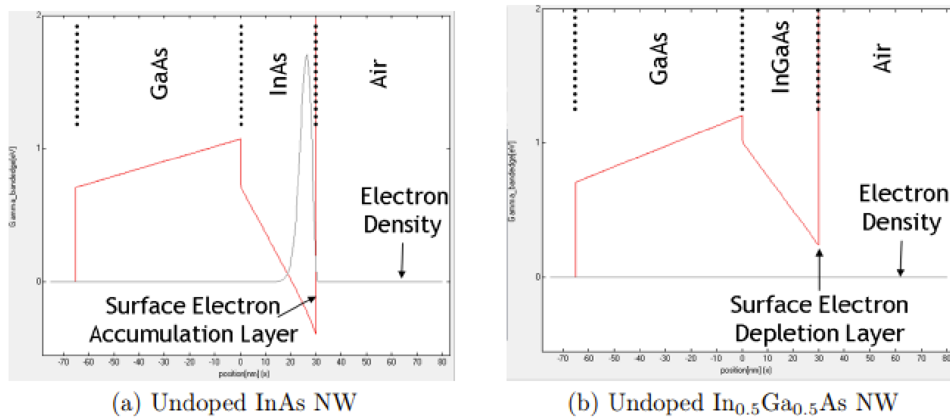

(a) Undoped InAs NW

(b) Undoped $In_{0.5}Ga_{0.5}As$ NW

Figure 59: Figure S1: Finite element simulations showing the conduction band (red) and electron concentrations (grey) in undoped InAs (a) and $In_{0.5}Ga_{0.5}As$ (b) NWs.

Here, Fermi level pinning in the conduction band was assumed for the InAs NW, resulting in a large electron concentration near the surface of the NW. The Fermi level pinning was simulated by implementing a donor surface charge density of 2.5×10^{12} cm^{-2}. In contrast, the InGaAs NW has no free electrons in the conduction band due to the lack of surface states which pin the Fermi level in the conduction band.

A 10 nm-thick modulation-doped layer was then inserted into the structure 20 nm below the InGaAs NW. A dopant concentration of 10^{19} cm^{-3} was assumed. The result of this simulation is given in Figure S2.

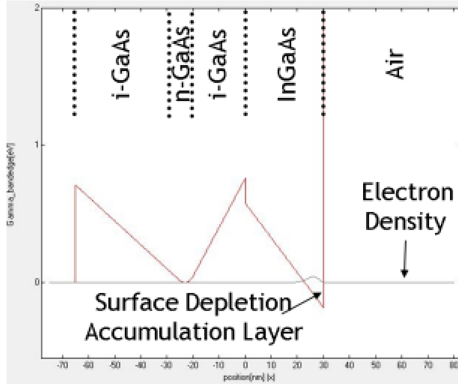

Figure 60: Figure S2: Finite element simulation of a modulation-doped $In_{0.5}Ga_{0.5}As$ NW showing the conduction band (red) and electron concentrations (gray). We see a maximum in the electron concentration now that appears in the InGaAs NW that appears due to the modulation-doped structure.

The addition of the remote doping layer does have an impact on the overall electron concentration in the NW. We now get a small peak in the electron density of 4×10^{16} cm^{-3}. This basic 1D simulation was sufficient as a proof of concept, however, a more in-depth study was then performed using the NW structure as determined by scanning transmission electron microscopy (STEM) energy dispersive x-ray spectroscopy (EDS) investigations combined with atom probe tomography (APT), as described in the main text.

9.8.2 X-ray Fluorescence Mapping

To get a better understanding of the uniformity of the NWs, especifically in the Y-junction devices, x-ray fluorescence (XRF) mapping was performed at the European Synchrotron Radiation Facility (ESRF) by Jaime Segura-Ruiz. Figure S3 gives an example of two measurements performed on InGaAs Y-branch structure. We can see In K_α signal is relatively uniform across the junction for Figure S3a. However, in the opposite orientation shown in Figure S3b, both the scanning electron microscopy (SEM) image and the In K_α signal show a large degree of non-uniformity across the junction.

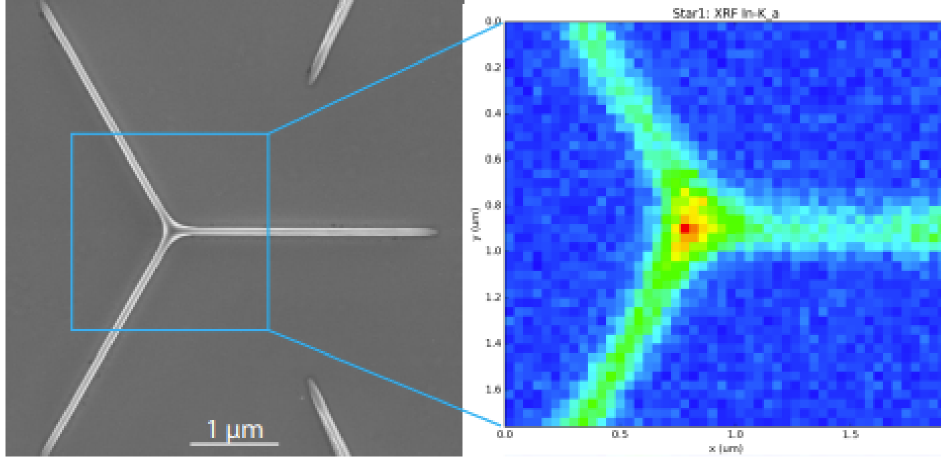

(a) Intersection of slits along $\langle \bar{1}\,\bar{1}\,2 \rangle$ directions.

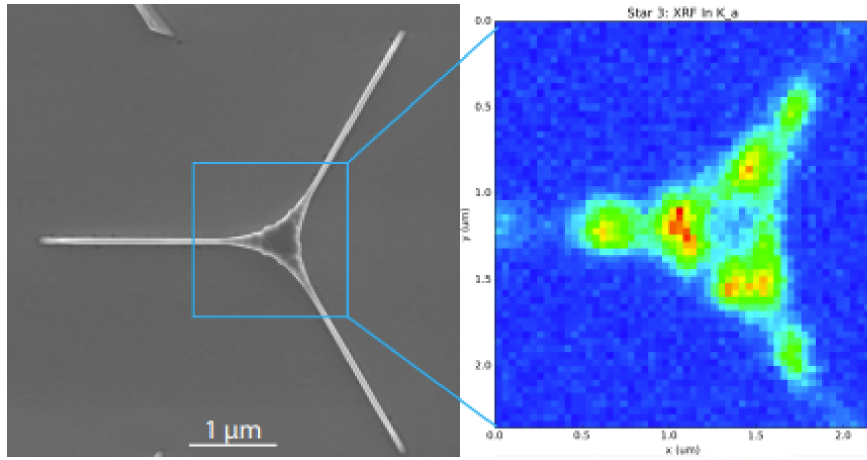

(b) Intersection of slits along $\langle 1\,1\,\bar{2} \rangle$ directions.

Figure 61: Figure S3: SEM images (left) combined with XRF maps of the In K_α signal (right) of InGaAs Y-branch structures in both the favourable intersection orientation (a) and unfavourable orientation (b).

The measurements were performed at the ID16B beamline at the ESRF with a beam size of 52 nm × 56 nm and beam energy of 29.8 keV.

9.8.3 Magnetoconductance Modeling

Here, we present the results from fitting the data with the clean limit as well as the diffusive limit. For clean limit, l_e was fixed at 20 nm to extract l_φ and l_{so}. The diffusive limit is valid when $l_e \ll W$. In this limit, the quantum correction to the classical conduction is given by

$$\Delta G = \frac{e^2}{hL}\left[3\left(\frac{1}{l_\varphi^2} + \frac{4}{3l_{so}^2} + \frac{1}{l_B^2}\right)^{-1/2} - \left(\frac{1}{l_\varphi^2} + \frac{1}{l_B^2}\right)^{-1/2}\right], \tag{41}$$

where here l_B is

$$l_B^2 = \frac{3\hbar^2}{e^2 W^2 B^2}. \tag{42}$$

Given that the mean free path of ~20 nm in the 3D regime is most appropriate, and our expected conducting channel's width is around this value, neither of the clean or the diffusive limits are exactly valid. The diffusive limit ignores boundary scattering completely, while the clean limit may over-emphasize this effect. Fits in the clean limit employing both specular as well as diffusive boundary scattering were conducted, giving very similar values for both. Next, we compare the diffusive fits to the clean fits, showing representative traces from both regimes below. From this plot, while both formulae give decent fits, we see that the clean regime fits the data slightly better than the diffusive regime, as evidenced by a smaller χ^2 in the fit (0.0025 vs 0.0081).

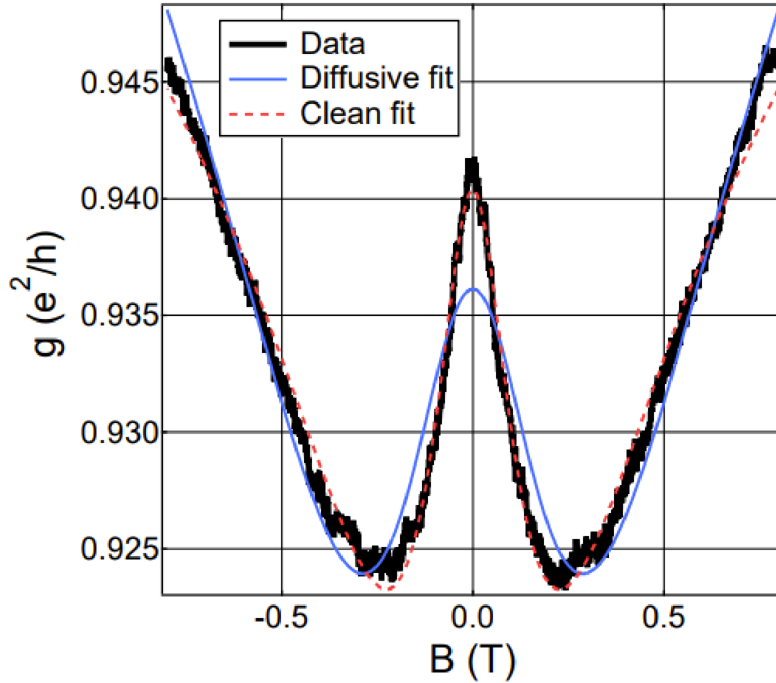

Figure 62: Figure S4: Comparison of magnetoconductance data fitting in the diffusive and clean limits. In the diffusive limit $l_\varphi = 74$ nm and $l_{so} = 55$ nm, while in the clean limit $l_\varphi = 94$ nm and $l_{so} = 70$ nm. Here we can see that the clean limit provides a much better fit to the experimental data.

9.8.4 Additional Magnetoconductance Measurements

The conduction of the device was also probed at 4 K and 1.9 K as a function of magnetic field and top gate voltage with and without the use of an AC oscillation coupled to the gate. First,

we present the values for $l\varphi$ and l_{so} extracted using Equation (2) on the dataset in Figure 3 (d) of the main text (with AC coupling) in Figure S5. l_e was initially extracted as a fit parameter to Equation (1) of the main text and found to be 20 ± 5 nm in the 3D limit. We then kept it fixed at 20 nm for the fits over the whole dataset. This was done to increase the reliability of the fits, as three free parameters are highly sensitive to starting conditions. Here, we find no significant change of l_{so} and l_φ as a function of V_g. Across the entire dataset l_φ has an average of 100 nm with a standard deviation of 10 nm and l_{so} 80 nm with standard deviation 5 nm.

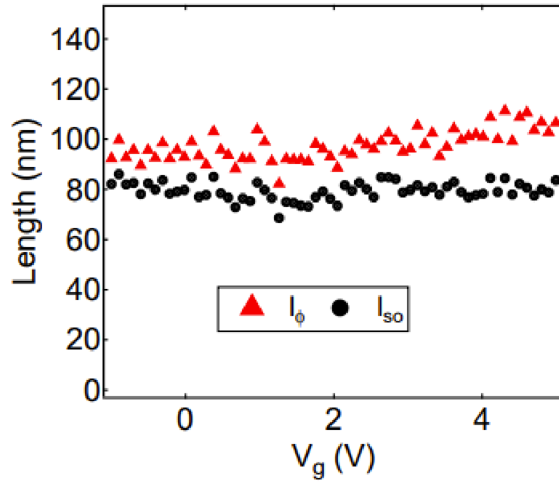

Figure 63: Figure S5: Plot of extracted values for l_φ and l_{so} from Figure 3 (d) of the main text. Data taken at 1.9 K.

In Figure S6, we present the results from unmodulated datasets daten at different temperatures on a different junction configuration compared to the previous data. The unmodulated data has a larger variance, but the overall trend of the values for l_φ and l_{so} remains the same. The agreement across multiple junction configurations is suggestive of a relatively homogeneous growth quality. The points are averages of traces taken at each particular value of gate voltage, which were carried out to mitigate switchers in some of the magnetoconductance data, attributed to the presence of trapped charges in the HfO_2 dielectic layer.

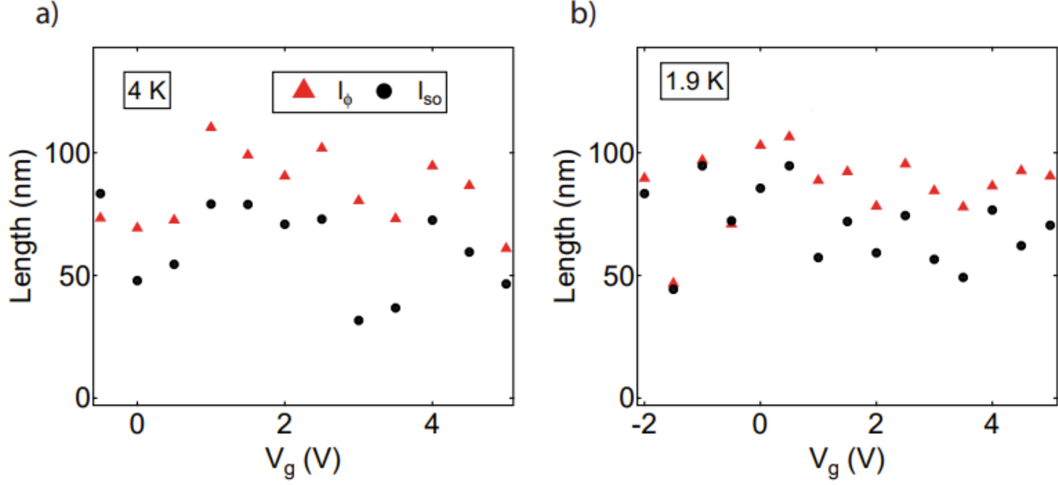

Figure 64: Figure S6: Plot of extracted values for l_φ and l_{so} at 4 K and 1.9 K (Figures (a) and (b) respectively) against gate voltage.

The analysis of the data, including the fitting, was carried out uniformly across the entirety of the data. It should be noted, however, that the weak anti-localization (WAL) formalism itself takes a uniform channel geometry into account, which is not the case across the junction. This introduces an additional uncertainty to the values of the extracted parameters (l_φ, l_{so}) through this formalism.

9.8.5 Description of Analysed Samples

Figure S7 depicts the main growth chip used for the APT and electrical analysis presented in this work. The growth chip consisted of a 1.1 nm triangle with three identical patterned regions labeled A, B and C. These regions were then used for various experiments. Region A was capped with HfO_2 for electrical experiments, however, high resistances obscured any interesting transport properties. Instead, they were then processed for structural characterization for STEM and APT analysis. However, due to the HfO_2 not being a favourable capping layer for APT, Region C was exclusively dedicated to APT analysis. It was therefore capped by amorphous GaAs before performing APT on it.

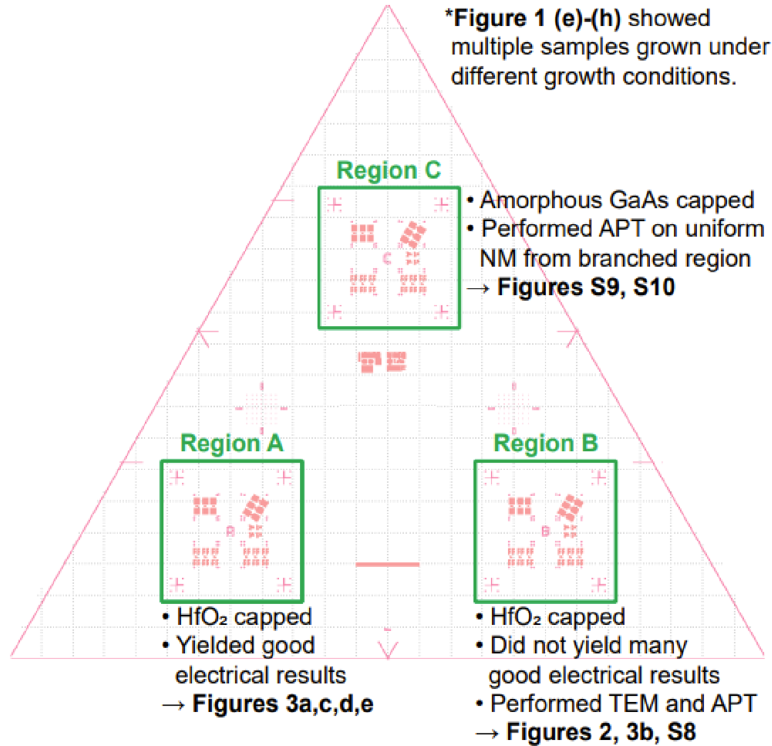

Figure 65: Figure S7: Diagram with descriptions of how the samples were processed for the structural and electrical analysis presented in this work.

9.8.6 APT Analysis of Multiple NWs from the Same Growth Chip

APT analysis was carried out on three NWs from the same growth chip. Figure 2 shows analysis of the first nanowire, and Figure S8 shows mass spectra from isolated regions of this sample. Analysis of two additional nanowires is shown in Figure S9 and Figure S10. All samples exhibit a very similar Si distribution, i.e., the Si sopants are concentrated near the InGaAs/GaAs interface. The peak at m/z = 14 was found to be a reliable measurew of the presence of Si dopants; m/z = 14 was detected near the interaface of each nanowire analyzed, but was not detected in measurable concentrations elsewhere. In contrast, the hit rate of m/z = 28 was observed to increase in noisier regions at the beginning and end of the APT run, even in the absence of m/z = 14, which likely indicates overlap with other species such as CO. For the sample in Figure 2, m/z = 28 was closely correlated with m/z = 14 in the region within 5-10 nm of the interface, so hits from both regions were included in Figure 2d. In Figure S9 and Figure S10, the species are plotted separately, with m/z = 14 in grey and m/z = 28 in light blue. The grey dashed line indicates the detection limit of Si^{++} and Si^{+} in these samples. Hits at m/z = 14.5, 15, 29 and 30, which include counts from $^{29}Si^{++}$, $^{30}Si^{++}$, $^{29}Si^{+}$, and $^{30}Si^{+}$, respectively, were not included

in the analysis on concentration due to potential overlap with unidentified species. To correct for this systematic undecounting, concentrations based on ^{28}Si counts were multiplied by a factor of 1.084, which amounts to assuming a natural isotope abundance in the Si source.

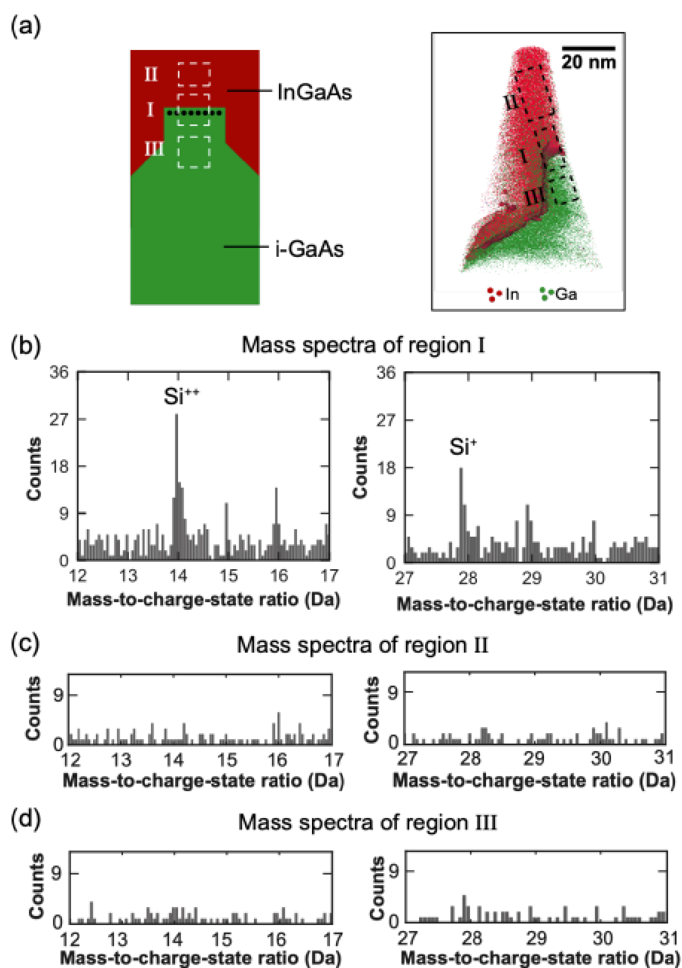

Figure 66: Figure S8: Mass spectra from different regions of the sample shown in Figure 2. (a) Schematic and corresponding APT reconstruction of the sample marked with the regions: (I) above the InGaAs/GaAs interface on the top; (II) around the top facet; (III) below the top facet. (b), (c), (d) Mass spectra near $^{14}Si^{++}$ and $^{28}Si^{++}$ in regions I, II, III respectively.

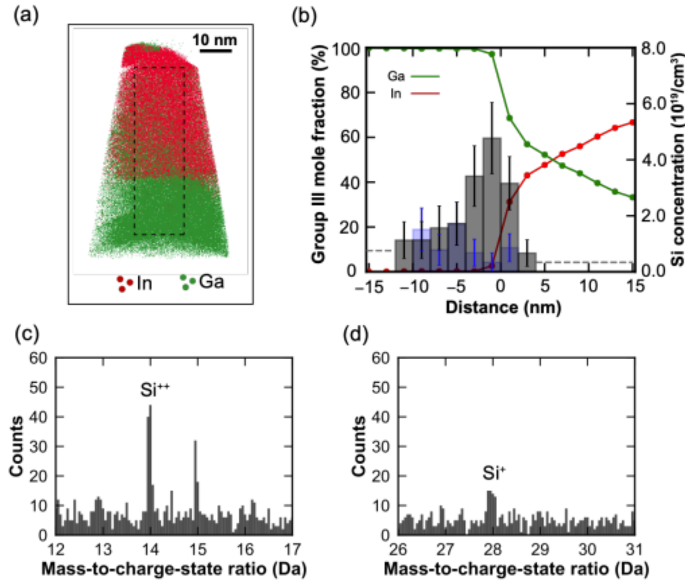

Figure 67: Figure S9: (a) APT reconstruction of a second sample. The black dashed line shows the region analyzed in the proxigram and mass spectra. (b) The proximity histogram of the sample moving from GaAs NM towards InGaAs NW. The distributions of Si^{++} and Si^{+} are shown in grey and light blue bars, respectively. The dashed grey line shows the detection limit of Si, which is sensitive to the total number of counts. (c), (d) Mass spectra around $^{14}Si^{++}$ and $^{28}Si^{++}$, respectively, for the region indicated by the black box in panel (a).

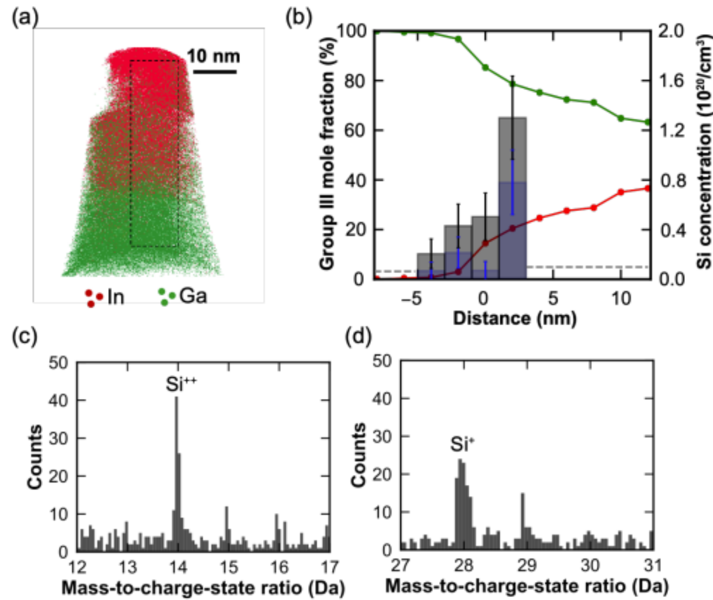

Figure 68: Figure S10: (a) APT reconstruction of a third sample. The black dashed line shows the region analyzed in the proxigram and mass spectra. (b) The proximity histogram of the sample moving from GaAs NM towards InGaAs NW. The distributions of Si^{++} and Si^{+} are shown in grey and light blue bars, respectively. The dashed grey line shows the detection limit of Si, which is sensitive to the total number of counts. (c), (d) Mass spectra around $^{14}Si^{++}$ and $^{28}Si^{++}$, respectively, for the region indicated by the black box in panel (a).

10 Outlook and Summary

10.1 Controlling Rashba Spin-Orbit Interaction: Principle Idea

Initial devices with the split-gate architecture depicted in schematics in the Nanofabrication chapter have been fabricated and preliminary measurements have been carried out on samples with modulation doping similar to those in the Remote Doping of Scalable Nanowire Branches chapter. The aim for these devices is to investigate the controllability of the Rashba spin-orbit interaction via the independent tuning of the carrier density in and electric field across the wires. Before displaying and discussing some of the preliminary results, we will first go through the principle. We know that the energy associated with Rashba spin-orbit interaction can be approximated (assuming isotropy) as [146]

$$E_R = \alpha k_F, \tag{43}$$

where $\alpha = \alpha_0 + \alpha_{mat}\vec{E_g}$ is the so-called Rashba parameter. α_0 is a sample specific offset, α_{mat} is a material specific constant, and $\vec{E_g}$ is the applied electric field across the wire due to the gates. We can approximate $\vec{E_g}$ as [153]

$$\vec{E_g} = \frac{1}{2}\left(\frac{V_{g1}}{d_{g1}} - \frac{V_{g2}}{d_{g2}}\right), \tag{44}$$

where V_i are the applied gate voltages and d_i are their distances from the wire. Another ingredient is the spin-orbit length, which can be expressed in terms of α as [240]

$$l_{so} = \frac{\hbar}{2m^*\alpha}. \tag{45}$$

This is relevant for our magnetoconductance measurements, as we will potentially have access to l_{so} via the weak (anti-)localization corrections to the conduction [240][139][163]:

$$\Delta G = -\frac{e^2}{hL}\left[3\left(\frac{1}{l_\varphi^2} + \frac{4}{3l_{so}^2} + \frac{1}{l_B^2}\right)^{-1/2} - \left(\frac{1}{l_\varphi^2} + \frac{1}{l_B^2}\right)^{-1/2} - 3\left(\frac{1}{l_\varphi^2} + \frac{4}{3l_{so}^2} + \frac{1}{l_e^2} + \frac{1}{l_B^2}\right)^{-1/2} + \left(\frac{1}{l_\varphi^2} + \frac{1}{l_e^2} + \frac{1}{l_B^2}\right)^{-1/2}\right] \tag{46}$$

So, by tuning the gate voltage applied to the two gates while keeping the carrier density fixed,

we expect the electrons to experience a changing electric field, which should act to modulate α, which will manifest in a change in l_{so}. The change in l_{so} would then surface in the changing shape of the weak (anti-)localization curves. This line of reasoning is valid if l_φ and l_e remain constant under different electric fields across the conducting channel.

10.2 Controlling Rashba Spin-Orbit Interaction: Device Architecture

The devices were fabricated with a four-point setup to bypass the large contact resistances that $In_xGa_{1-x}As$ wires with $x \lesssim 0.5$ typically host. The length between the middle contacts, thus the channel being measured, was lithographically defined to be 500 nm.

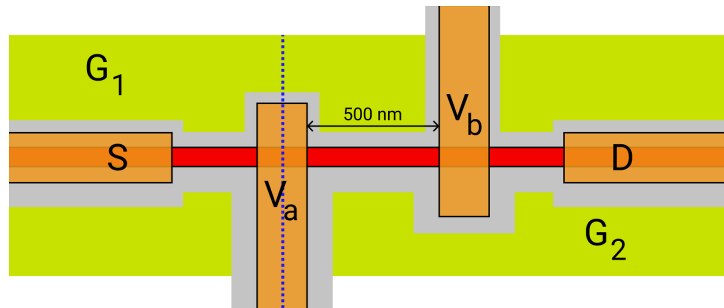

Figure 69: Top view schematic of a split-gate device. S: source, D: drain, $V_{a,b}$: voltage probes, $G_{1,2}$ gates. Grey represents HfO_2 dielectric, red is the nanowire under investigation, orange is contacts and voltage probes, yellow-green is the gates. The blue dashed line represents the linecut through which a FIB cut was made and subsequently imaged via TEM.

The previous schematic represents a typical device architecture for nanowire with a split-gate. Such a device was subjected to a FIB (focused ion beam) cut of a lamella, which was then imaged using HAADF (high-angle annular dark-field) in a TEM (transmission electron microscope) to demonstrate the cross-section of a real device. The cross section was taken across the blue dashed line in the previous image.

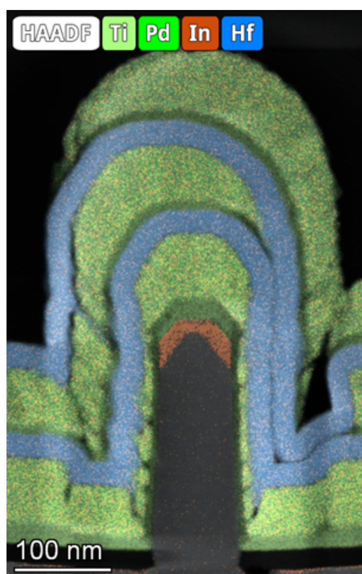

Figure 70: False-colored TEM image using HAADF of a cross section from a fabricated split-gate device. Dark grey represents the nanomembrane, orange the InGaAs nanowire, blue the HfO_2, and green the Ti/Pd contacts and gates. Image courtesy of Didem Dede.

Taking a look at the TEM image, a couple of things come to mind. First, the total gate stack is rather high. The FIB cut that was taken happened to be through the contact, so this does not show what the result is between the contacts in the conducting channel. From this image, it appears that the second top gate layer might not be able to influence the wire as much as would be desired. The measured data (see next section) indicates, however, that it was sufficient to apply a voltage to the wire. Second, the side-wall coverage of the contact itself is very sparse. In future fabrication runs this could be improved upon by depositing more metal during the tilt and less from directly above. Third, the general stack itself can likely be reduced, which would ensure that each gate was, indeed, properly located to the sides of the device. This could be done by decreasing the thickness of the HfO_2 dielectric layers as well as by depositing less metal on each gate layer. With these points in mind, it should still be seen as an indicator that the design itself is viable, and that with some minor changes we should hope for more success.

10.3 Controlling Rashba Spin-Orbit Interaction: Preliminary Measurements and Discussion

With a clear understanding of the device architecture, we can now move onto some preliminary measurements. After fabrication, the sample was inserted into a dilution refrigerator equipped with a magnet. Below is a map of conduction as a function of the voltage applied by the two side gates.

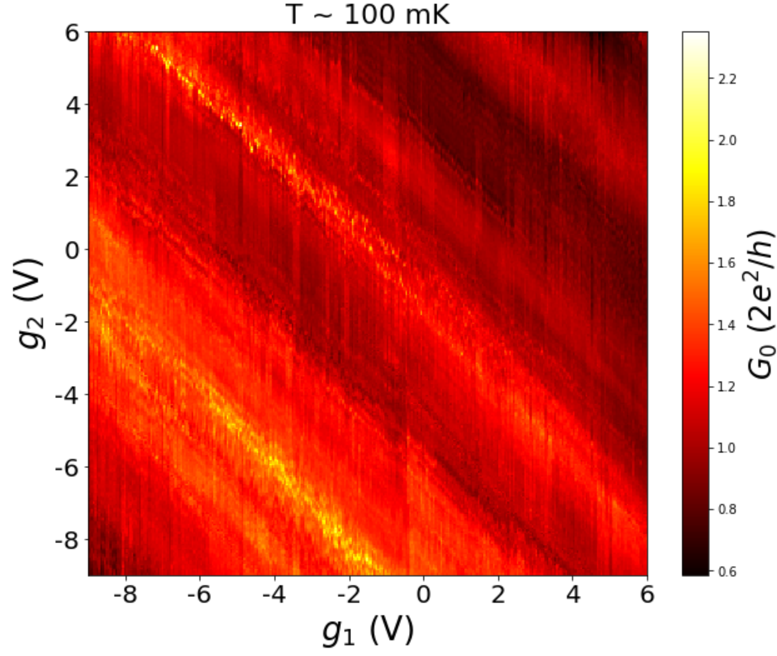

Figure 71: Two dimensional plot of conductance (color scale) G in units of $2e^2/h$ as a function of the two side gates g_1 and g_2. Measurement taken at 100 mK. Four-point measurement using standard lockin techniques with an excitation voltage of 30 μV and no DC bias offset.

Here, we see that the response of the device to the gates is nearly symmetric in its contours going from the top left to the bottom right. What we also notice are oscillations in the conduction going perpendicular to these contours. This was not expected and is not fully understood. Additionally, the wire does not pinch off in the range of the applied voltages. More thoughts on this follow later.

Next, we probed a contour of constant density as a function of magnetic field B_z. This was done by setting the total applied gate voltage, which we call $\varepsilon = g_1 + g_2$, equal to zero but changing the contributions from each individual gate. This should keep the density constant across the wire, while changing the electric field it experiences.

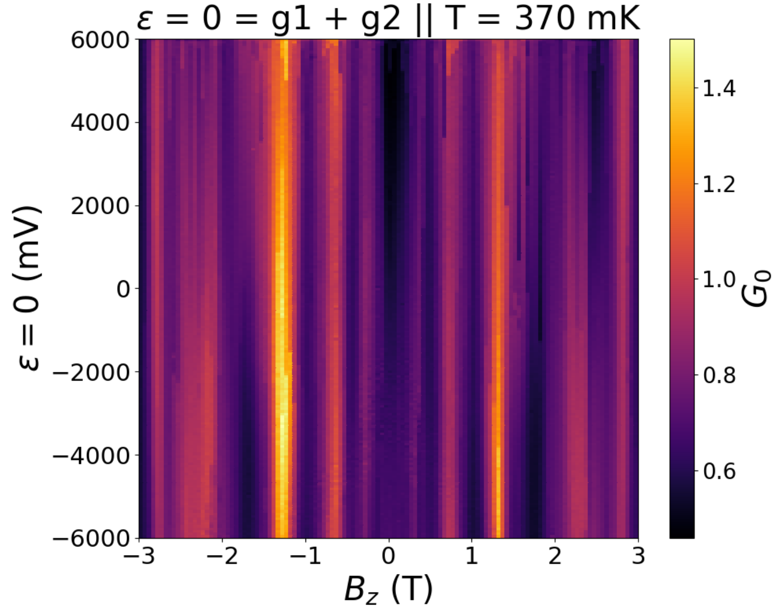

Figure 72: Two dimensional plot of conductance (color scale) G in units of $2e^2/h$ as a function of parameterized electric field across the wire $\varepsilon = 0 = g_1 + g_2$ and magnetic field B_z. Measurement taken at 370 mK.

Taking horizontal line cuts from this plot, we get magentoconductance responses at different values for the electric field across the wire.

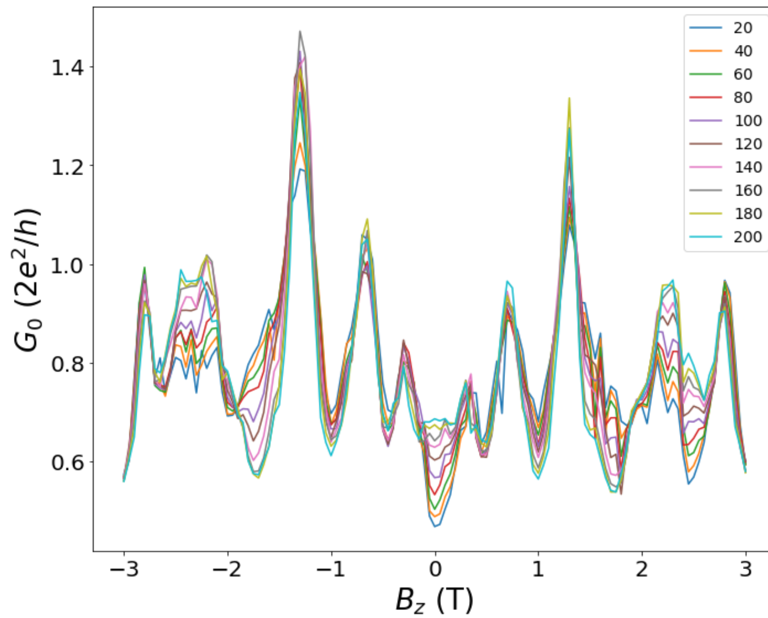

Figure 73: Line cuts from the previous color plot at different electric fields. Measurement taken at 370 mK.

There are a number of things that we need to consider when looking at these line cuts. First, we appear to have the presence of UCF superimposed on our conductance traces. These obscure the exact value of our conductance. Second, if we look at the area around $B_z = 0$ T, we see

a consistent evolution from a deep weak localization behavior (strong reduction in conductance at $G(B_z = 0)$, dark blue) up to, perhaps, the onset of weak anti-locazlization (increase in conductance at $G(B_z = 0)$, light blue). If this interpretation is correct, that would suggest that the application of the electric field was tuning the Rashba parameter. Then, given this and given that the fluctuations were due to UCF, we would need to subtract the background conduction that the fluctuations were superimposed upon in order to quantify the magnitude of the effect. Measurements have been carried out with qualitatively similar results up to $\varepsilon = \pm 1$ V. Offsets greater than this yielded inconsistent results, which suggests that changing the chemical potential (by changing carrier density) past a certain point somehow introduces significant noise on the system. This is not fully understood at the moment, but one possible explanation could be that the wave function of the carriers sits in a different location. Another possibility is that changes to the gate voltages variably activate charge traps in the oxide layers, resulting in unpredictable behavior. More devices are needed to assess these problems.

Another point is that the wires could not be pinched off completely, even with the application of very large voltages ($<$ -80 V!) on the gates. For comparison, the wires in Chapter 9 pinched off at around -2 V. This may be due to additional roughness at the interface between the GaAs nanomembranes and the InGaAs nanowires [122]. Furthermore, it was discovered after the measurements that the growth that these particular devices were fabricated from deviated in material composition from that in Chapter 9. Below is a representative EDX (energy-dispersive X-ray) analysis of a nanowire cross-section from the same chip.

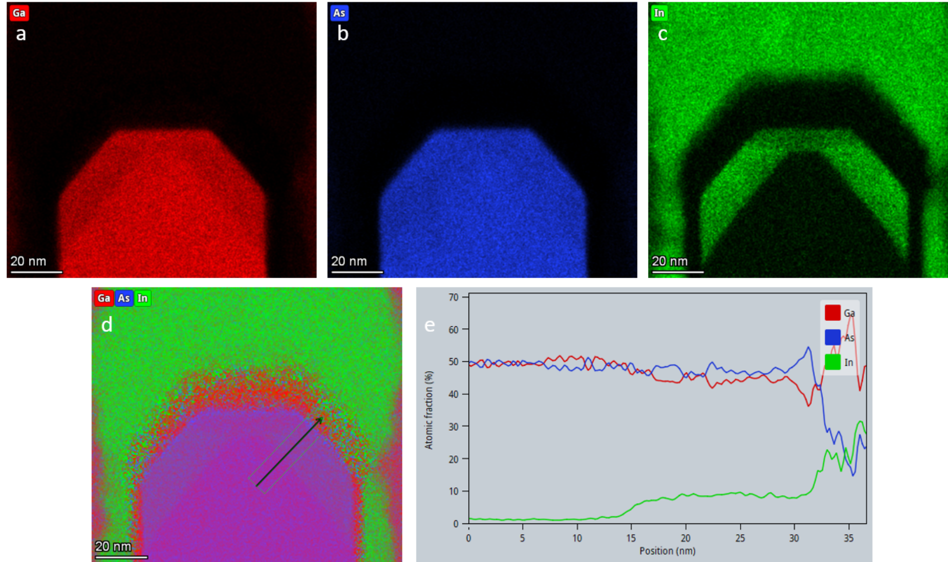

Figure 74: EDX analysis of representative nanowire cross-section. a-c: Ga, As, and In distributions respectively. d: combined result of the three with arrow indicating direction of atomic fraction percent. d: atomic fraction indicating In content $\sim$ 10 percent. Images courtesy of Didem Dede.

Compared with the results of the nanowire composition in Chapter 9, we notice a significant decrease in In content, which was unexpected. Upon looking into it, it was found that while the growth recipe was the same, the In container in the MBE was nearly empty, and the resultant In flux was lower than expected. Without being able to pinch the wires off, we have no way to access the mobility in the wires, thus can not indepently fix l_e. Without this, we can not extract quantitative values for l_{so}, even if we were able to extract l_φ from the UCF.

Therefore, while we see signs that the device architecture may be working as intended, more devices are necessary to confirm that we are, indeed, modulating the spin-orbit interaction across the wires. Devices where we can pinch off to get access to the mean free path could then be quantitatively analyzed and a thorough investigation of l_{so} as a function of density and electric field can be carried out. As of this writing, devices are being grown and will be investigated in the near future.

10.4 Additional Outlook and Summary

As alluded to earlier, there is a wealth of interesting physics that can be explored in selectively grown nanowire systems of sufficient crystalline purity. In addition to controlling the Rashba spin-orbit interaction, with improvements in growth and fabrication techniques, one could expect to investigate quantized (ballistic) transport [206], quantum dots [264][265][266], spin qubits

[267], coupling of superconductors [195], and, perhaps, 1D-1D tunneling spectroscopy of stacked nanowires [261][262][263]. The interface between the nanowire and the nanomembrane likely needs to be sharper and host of fewer defects for these. Overall defect density throughout the wires themselves is also necessary in order to move past diffusive transport and towards ballistic behavior. Encapsulation of the nanowires with a dielectric or a high-bandgap semiconductor, such as GaAs could serve to, both, increase the surface quality as well as provide a thin barrier for a future superconductor deposited on top. It has been predicted theoretically that without a thin insulating barrier between the semiconductor nanowire and the superconductor, the transverse subbands of the wire shift in energy significantly compared to the chemical potential of the wire itself, making the realization of a topological state in such a system [268]. For many of these future prospects, we must move away from using dopants, which should be possible with sufficiently high indium content in the wires, as the Fermi level should be pinned in the conduction band at the surface for homogenous, high indium content wires [152].

In summary, multiple, novel semiconducting nanostructures have been realized, measured and analyzed. First, InGaAs nanowires with bulk Si^+ dopants selectively grown on top of GaAs nanomembranes served as a first proof-of-principle. Fabrication techniques to contact these high aspect ratio structures were developed. These first wires had small mean free paths and low indium content, which displayed no discernible spin-orbit interaction in the magnetoconductance measurements. Weak localization behavior was observed and a lower bound for the spin-orbit length could be extracted.

Next, some aspects of the growth of the wires were adapted, resulting in higher indium content wires. At this point, additionally, we moved from a bulk doping to a modulation doping strategy in order to reduce the scattering due to the presence of Si^+ ions inside the conducting channels. Simultaneously, a fabrication procedure to selectively deposit HfO_2 was envisioned, tested, and executed to allow for the depositing of electrostatic top gates on the devices. This allowed tuning of the carrier density in the wires and, thus, the independent extraction of a longer mean free path compared with the bulk doping approach. Magnetotransport across the nanowire Y-junctions was probed in these devices yielding clear signals of weak antilocalization, showcasing strong spin-orbit interaction in the wires.

Later, a more advanced fabrication process with multiple ALD and gate layers was developed in order to create initial devices with a split-gate architecture. This allows the independent tuning

of the carrier density and the electric field across the wires, and can serve as a system for the manipulation and control of Rashba spin-orbit interaction in the future.

11 Fabrication Recipes

11.1 Devices from Template-Assisted Scalable Nanowire Networks

11.1.1 Phase 1: PMMA

- Spinning of 400 nm PMMA 5 %
  - Cleaning/preparation of sample
    * Remove sample from silicon wafer: 200 °C on hot plate to dislodge As paste (if applicable)
    * 1 min. in acetone (ACE) at 20 % sonication
    * 4 further min. in ACE
    * 1 min. IPA
    * Blow drying
    * Heat 5 min. at 120 °C
    * Blow drying
  - Spinning
    * 2000 rpm
    * Step size: 4
    * 40 sec
  - Bake 5 min at 180 °C
  - Blow dry
  - Apply gold nanoparticles to corners for e-beam focusing
  - Take photos to ensure an even coating and measure distance to gold particles

11.1.2 Phase 2: E-beam Lithography for contacts and Development

- Preparation with gold particle placement
- GDS files prepared for membrane arrays as needed
- e-beam lithography
  - 20 kV

- dose of 200 μC / cm^2 for the 2 mm write field
- dose of 200 μC / cm^2 for the 400 μm write field

- Development
  - (MIBK + IPA) : MEK with ratio of 100:1.3
  - 90 sec. in developer at 4 °C (should do this at -15 °C for very fine gate structures for optimal development [116], in which case it should only be developed for 30 sec.)
  - 30 sec. in IPA
  - Blow drying

11.1.3 Phase 3: Reactive Ion Etching

- O_2 plasma to remove PMMA residues
  - 16% O_2
  - $5e^{-5}$ mbar
  - 30 W
  - 30 sec.
  - 250 mTorr
- Etches about 25 nm PMMA
- This should be done after development on *every* lithography step

11.1.4 Phase 4: Ammonium Polysulfide (NH_4S_x) Etching + Ti/Au (or Ti/Pd) Evaporation

- Before etch preparation of Sharon: removal of plate and placement of sticky tape aligned properly with respect to the nanomembranes (for side wall coverage during angle evaporation) with mark for quick transition into vacuum
- NH_4S_x etching solution with DI water
  - Solvent heated to 40 °C (DI water). Give this 20 min. to stabilize
  - Mix NH_4S_x magnetically for a few minutes ahead of time

- Use syringe with filter to optimally clean the solution before mixing with the DI water
- Etch time of 6 min
- Etch time can be varied and could be investigated as an etch series for comparison
- The purity of the InAs will play a role, once it is clear that the samples are mostly of the same composition, this should be more thoroughly investigated to optimize contacts
- Insertion into Sharon in vacuum state inside of 5 minutes (ideally inside of 2-3)

- Sharon evaporation
  - 4 nm Ti evaporation at +/- 23°each as well as 2 nm planar
  - 40 nm Au evaporation at +/- 23°each as well as 10 nm planar

11.1.5 Alternative Phase 4a: Argon Milling Etch + Ti/Pd Evaporation

- This is a method that has not been used in over a year. The process takes much longer than using Sharon and has not yielded noticably better results. It could be investigated for potential optimization and comparison to the NH_4S_x method in the future
- Chip placed into Bestec with membranes properly aligned parallel to screw axis
- Ar milling
  - Base Pressure: $7 \cdot 10^{-6}$ mbar
  - Ar Flow: Needle valve adjusted to give steady process pressure
  - Process Pressure: $5 \cdot 10^{-5}$ mbar
  - Plasma Power (Magnetron): Adjust voltage so that output current is at 20 mA
  - Extraction Voltage: -0.6 kV
  - Anode Voltage: 1 kV
  - Exposure Time: 2 - 3.5 min.
- Evaporation:
  - E-gun evaporation of Ti (2 x 7 nm)
  - thermal evaporation of Pd (2 x 60 nm)

- Notes:
  * Correct "filter" on reader must be selected for each material
  * +/- 25°for both process as normal, but on this machine it is very difficult to modulate this parameter as well as one can with Sharon
  * For angle evaporation of Pd:
    · z at 125
    · +25°:
      y at 00.42
      x at 97.26
    · -25°:
      y at 99.735
      x at 98.075
  * 82.5 min. per 30 nm evaporation

11.1.6 Phase 5: Metal Lift-off

- ACE at 50 °C for 2 h
- Use plastic pipette for turbulence to blow off metal
- Sonication at 20 % for 30 sec. (40 % also appears to work without damaging the membrane quality, but this should be avoided whenever possible.)
- Use pipette again
- IPA flush for 1 min.
- Blow dry
- Photos

11.2 Devices from Remote Doping of Scalable Nanowire Branches

11.2.1 Phase 1: PMMA

- Spinning of 400 nm PMMA 5 %
  - Cleaning/preparation of sample

    * Remove sample from silicon wafer: 200 °C on hot plate to dislodge As paste (if applicable)
    * 1 min. in acetone (ACE) at 20 % sonication
    * 4 further min. in ACE
    * 1 min. IPA
    * Blow drying
    * Heat 5 min. at 120 °C
    * Blow drying
  - Spinning
    * 2000 rpm
    * Step size: 4
    * 40 sec
  - Bake 5 min at 180 °C
  - Blow dry
  - Apply gold nanoparticles to corners for e-beam focusing
  - Take photos to ensure an even coating and measure distance to gold particles

11.2.2 Phase 2: E-beam Lithography for contacts and Development

- Preparation with gold particle placement
- GDS files prepared for membrane arrays as needed
- e-beam lithography
  - 20 kV
  - dose of 200 μC / cm^2 for the 2 mm write field
  - dose of 200 μC / cm^2 for the 400 μm write field
- Development
  - (MIBK + IPA) : MEK with ratio of 100:1.3
  - 90 sec. in developer at 4 °C (should do this at -15 °C for very fine gate structures for optimal development [116], in which case it should only be developed for 30 sec.)

- 30 sec. in IPA
- Blow drying

11.2.3 Phase 3: Reactive Ion Etching

- O_2 plasma to remove PMMA residues
  - 16% O_2
  - $5e^{-5}$ mbar
  - 30 W
  - 30 sec.
  - 250 mTorr
- Etches about 25 nm PMMA
- This should be done after development on *every* lithography step

11.2.4 Phase 4: Ammonium Polysulfide (NH_4S_x) Etching + Ti/Au (or Ti/Pd) Evaporation

- Before etch preparation of Sharon: removal of plate and placement of sticky tape aligned properly with respect to the nanomembranes (for side wall coverage during angle evaporation) with mark for quick transition into vacuum
- NH_4S_x etching solution with DI water
  - Solvent heated to 40 °C (DI water). Give this 20 min. to stabilize
  - Mix NH_4S_x magnetically for a few minutes ahead of time
  - Use syringe with filter to optimally clean the solution before mixing with the DI water
  - Etch time of 2.5 min
  - Etch time can be varied and could be investigated as an etch series for comparison
  - The purity of the InAs will play a role, once it is clear that the samples are mostly of the same composition, this should be more thoroughly investigated to optimize contacts
  - Insertion into Sharon in vacuum state inside of 5 minutes (ideally inside of 2-3)

- Sharon evaporation
  - 4 nm Ti evaporation at +/- 23°each as well as 2 nm planar
  - 40 nm Au evaporation at +/- 23°each as well as 10 nm planar

11.2.5 Phase 5: Metal Lift-off

- ACE at 50 °C for 2 h
- Use plastic pipette for turbulence to blow off metal
- Sonication at 20 % for 30 sec. (40 % also appears to work without damaging the membrane quality, but this should be avoided whenever possible.)
- Use pipette again
- IPA flush for 1 min.
- Blow dry
- Photos

11.2.6 Phase 6: ALD window of HfO_2

- Make sure to take photos before ALD process for comparison
- Spining of bi-layer resist
  - PMMA/MMA 33% 617.08
    - 6000 rpm
    - Step size: 4
    - 40 sec
    - bake 5 min at 180 °C
    - yields roughly 600 nm
  - PMMA 679.03
    - 3500 rpm
    - Step size: 4
    - 40 sec

        * bake 5 min at 180 °C
        * yields roughly 200 nm

- e-beam lithography on window
    - 10 kV
    - Dose 140 μC/cm^2
    - It's an overdose on purpose, just need to open up the area and resolution is not relevant
    - Develop the same as with contacts
- Load the recipe for deposition of HfO_2
- set the desired number of layers
    - 10 layers correspond to ~1.6 nm of oxide
    - 40 nm of HfO_2 was used on the majority of samples. This was leak tight even for gates that were overlapping contacts
    - An oxide thickness series could be carried out to find the optimal thickness. It is likely that thinner oxides will also be leak tight
- In the future, it could be investigated whether or not an NH_4S_x step before deposition of the oxide layer affects the quality of the membranes

11.2.7 Phase 7: Spinning PMMA, Lithography, and Metallization of Wrap-Around Gates

- Follow same procedure with PMMA and SEM lithography as with contacts
- For the evaporation of wrap-around top gates $10 \times 10/40 \times 40$ nm of Ti/Au was used
- For thinner gating schemes such as finger gates, this may require thinning and/or optimization
- For liftoff, follow same procedure as with contacts

11.3 Devices with Split-Gate Architecture

11.3.1 Phase 1: PMMA

- Spinning of 400 nm PMMA 5 %
  - Cleaning/preparation of sample
    - Remove sample from silicon wafer: 200 °C on hot plate to dislodge As paste (if applicable)
    - 1 min. in acetone (ACE) at 20 % sonication
    - 4 further min. in ACE
    - 1 min. IPA
    - Blow drying
    - Heat 5 min. at 120 °C
    - Blow drying
  - Spinning
    - 2000 rpm
    - Step size: 4
    - 40 sec
  - Bake 5 min at 180 °C
  - Blow dry
  - Apply gold nanoparticles to corners for e-beam focusing
  - Take photos to ensure an even coating and measure distance to gold particles

11.3.2 Phase 2: E-beam Lithography for contacts and Development

- Preparation with gold particle placement
- GDS files prepared for membrane arrays as needed
- e-beam lithography
  - 20 kV
  - dose of 200 μC / cm^2 for the 2 mm write field

- dose of 200 μC / cm^2 for the 400 μm write field

- Development
  - (MIBK + IPA) : MEK with ratio of 100:1.3
  - 90 sec. in developer at 4 °C (should do this at -15 °C for very fine gate structures for optimal development [116], in which case it should only be developed for 30 sec.)
  - 30 sec. in IPA
  - Blow drying

11.3.3 Phase 3: Reactive Ion Etching

- O_2 plasma to remove PMMA residues
  - 16% O_2
  - $5e^{-5}$ mbar
  - 30 W
  - 30 sec.
  - 250 mTorr
- Etches about 25 nm PMMA
- This should be done after development on *every* lithography step

11.3.4 Phase 4: Ammonium Polysulfide (NH_4S_x) Etching + Ti/Au (or Ti/Pd) Evaporation

- Before etch preparation of Sharon: removal of plate and placement of sticky tape aligned properly with respect to the nanomembranes (for side wall coverage during angle evaporation) with mark for quick transition into vacuum
- NH_4S_x etching solution with DI water
  - Solvent heated to 40 °C (DI water). Give this 20 min. to stabilize
  - Mix NH_4S_x magnetically for a few minutes ahead of time
  - Use syringe with filter to optimally clean the solution before mixing with the DI water

- Etch time of 2.5 min
- Etch time can be varied and could be investigated as an etch series for comparison
- The purity of the InAs will play a role, once it is clear that the samples are mostly of the same composition, this should be more thoroughly investigated to optimize contacts
- Insertion into Sharon in vacuum state inside of 5 minutes (ideally inside of 2-3)

- Sharon evaporation
  - 4 nm Ti evaporation at +/- 23°each as well as 2 nm planar
  - 40 nm Au evaporation at +/- 23°each as well as 10 nm planar

11.3.5 Phase 5: Metal Lift-off

- ACE at 50 °C for 2 h
- Use plastic pipette for turbulence to blow off metal
- Sonication at 20 % for 30 sec. (40 % also appears to work without damaging the membrane quality, but this should be avoided whenever possible.)
- Use pipette again
- IPA flush for 1 min.
- Blow dry
- Photos

11.3.6 Phase 6: ALD window of HfO_2

- Make sure to take photos before ALD process for comparison
- Spining of bi-layer resist
  - PMMA/MMA 33% 617.08
    - 6000 rpm
    - Step size: 4

        * 40 sec
        * bake 5 min at 180 °C
        * yields roughly 600 nm
    - PMMA 679.03
        * 3500 rpm
        * Step size: 4
        * 40 sec
        * bake 5 min at 180 °C
        * yields roughly 200 nm

- e-beam lithography on window
    - 10 kV
    - Dose 140 μC/cm^2
    - It's an overdose on purpose, just need to open up the area and resolution is not relevant
    - Develop the same as with contacts
- Load the recipe for deposition of HfO_2
- set the desired number of layers
    - 10 layers correspond to $\sim$1.6 nm of oxide
    - 40 nm of HfO_2 was used on the majority of samples. This was leak tight even for gates that were overlapping contacts
    - An oxide thickness series could be carried out to find the optimal thickness. It is likely that thinner oxides will also be leak tight
- In the future, it could be investigated whether or not an NH_4S_x step before deposition of the oxide layer affects the quality of the membranes

11.3.7 Phase 8: Spinning PMMA and Lithography of First Split Gate

- Follow same procedure with PMMA and SEM lithography as with contacts

- For the evaporation of first split gate layer tilt sample 23°to one side with respect to the nanomembranes
- Evaporation of 7/53 nm of Ti/Pd (Au also possible)
- For liftoff, follow same procedure as with contacts

11.3.8 Phase 9: Second ALD Window of HfO_2

- Make sure to take photos before ALD process for comparison
- Spining of bi-layer resist
  - PMMA/MMA 33% 617.08
    - 6000 rpm
    - Step size: 4
    - 40 sec
    - bake 5 min at 180 °C
    - yields roughly 600 nm
  - PMMA 679.03
    - 3500 rpm
    - Step size: 4
    - 40 sec
    - bake 5 min at 180 °C
    - yields roughly 200 nm
- e-beam lithography on window
  - 10 kV
  - Dose 140 μC/cm^2
  - It's an overdose on purpose, just need to open up the area and resolution is not relevant
  - Develop the same as with contacts
- Load the recipe for deposition of HfO_2

- set the desired number of layers
  - 10 layers correspond to ∼1.6 nm of oxide
  - 40 nm of HfO_2 was used on the majority of samples. This was leak tight even for gates that were overlapping contacts
  - An oxide thickness series could be carried out to find the optimal thickness. It is likely that thinner oxides will also be leak tight
- In the future, it could be investigated whether or not an NH_4S_x step before deposition of the oxide layer affects the quality of the membranes

11.3.9 Phase 10: Spinning PMMA and Lithography of Second Split Gate

- Follow same procedure with PMMA and SEM lithography as with contacts
- For the evaporation of first split gate layer tilt sample 23°to other side with respect to the nanomembranes
- Evaporation of 7/53 nm of Ti/Pd (Au also possible)
- For liftoff, follow same procedure as with contacts

11.4 Glueing into Chip Carrier and Gold Bonding

- Chip carrier cleaned for 5 min. in ACE at 100 % sonication
- 1 min. IPA flush
- Blow dry
- Ag paste used to glue sample into carrier (Shake bottle very well)
- Leave to dry for 30 min. before bonding
- Offer ritual sacrifice to the gods (small animals are usually - but not always - sufficient)
- Au bonding

References

[1] Huard, Roger L., *Plato's Political Philosophy: The Cave*, New York: Algora

[2] Digoenes Laërtius, *Life of Plato*, V

[3] H. Zhang, CX. Liu, S. Gazibegovic, et al, *Retraction note: Quantized Majorana conductance.*, Nature 591, E30 (2021)

[4] S. Vaitiekenas, G.W. Winkler, B. Van Heck, T. Karzig, M. T. Deng, K. Flensberg, L. I. Glazman, C. Nayak, P. Krogstrup, R. M. Lutchyn and C. M. Marcus, *Flux-induced topological superconductivity in full-shell nanowires*, Science 367, eaav3392 (2020)

[5] S. Gazibegovic, D. Car, H. Zhang, S. C. Balk, J. A. Logan, M. W. A. de Moor, M. C. Cassidy, R. Schmits, D. Xu, G. Wang, P. Krogstrup, R. L. M. Op het Veld, K. Zuo, Y. Vos, J. Shen, D. Bouman, B. Shojaei, D. Pennachio, J. Sue Lee, P. J. van Veldhoven, S. Koelling, M. A. Verheijen, L. P. Kouwenhoven, C. J. Palmstrom and E. P. A. M. Bakkers, *Epitaxy of advanced nanowire quantum devices*, Nature 548, 434-438 (2017)

[6] Tzu, L. *Tao Te Ching*, A. Waley, Trans. Wordsworth Editions (1996)

[7] Mandelbrot, B. *The Fractal Geometry of Nature*, W. H. Freeman and Co. (1982)

[8] H. van Houten et al., *Physics and Technology of Submicron Structures*, H. Heinrich, G. Bauer, and F. Kuchar, eds). Springer, Berlin (1988)

[9] H. van Houten et al., *Magnetoresistance of narrow GaAs-(Al, Ga)As heterostructures in the quasi-ballistic regime*, Acta Electronica 28, 27-38 (1988)

[10] P. Krogstrup, N. L. B. Ziino, W. Chang, S. M. Albrecht, M. H. Madsen, E. Johnson, J. Nygård, C. M. Marcus, and T. S. Jespersen, *Epitaxy of semiconductor-superconductor nanowires*, Nature Materials 14, 400-406 (2015)

[11] T. S. Cheng, A. Davies, A. Summerfield, Y. Cho, I. Cebula, R. J. A. Hill, C. J. Mellor, A. N. Khlobystov, T. Taniguchi, K. Watanabe, P. H. Beton, C. T. Foxon, L. Eaves, and S. V. Novikov, *High temperature MBE of graphene on sapphire and hexagonal boron nitride flakes on sapphire*, Journal of Vacuum Science & Technology, B, Nanotechnology and Microelectronics: Materials, Processing, Measurement, and Phenomena 34, 02L101 (2016)

[12] S. Valdueza-Felip, *Nitride-Based Semiconductor Nanostructures for Applications in Optical Communications at 1.5 um*, PhD Thesis [Universidad de Alcalá, Escuela Politécnica, Departamento de Electrónica] (2011)

[13] M. Friedl, *Scalable Nanowire Networks: Growth and Functionality*, PhD Thesis [École Polytechnique Fédérale de Lausanne] (2020)

[14] D. J. Smith, T. Aoki, J. K. Furdyna, X. Liu, M. R. McCartney, and Y. H. Zhang, *Atomic-scale characterization of (mostly zincblende) compound semiconductor heterostructures*, Journal of Physics: Conference Series 471, 012005 (2013)

[15] Semiconductor Industry Association, *Global Semiconductor Sales Increase 24% Year-to-Year in October; Annual Sales Projected to Increase 26% in 2021, Exceed $600 Billion in 2022*, https://www.semiconductors.org/global-semiconductor-sales-increase-24-year-to-year-in-october-annual-sales-projected-to-increase-26-in-2021-exceed-600-billion-in-2022/ (2021, Dec. 3)

[16] M. Sarsby, N. Yurttagül, and A. Geresdi, *500 microkelvin nanoelectronics*, Nature Communications 11, 1-7 (2020)

[17] M. Palma, C. P. Scheller, D. Maradan, A. V. Feshchenko, M. Meschke, and D. M. Zumbühl, *On-and-off chip cooling of a Coulomb blockade thermometer down to 2.8 mK*, Appl. Phys. Lett. 111, 253101 (2017)

[18] A. T. Jones, C. P. Scheller, J. R. Prance, Y. B. Kalyoncu, D. M. Zumbühl, R. P. Haley, *Progress in cooling nanoelectronic devices to ultra-low temperatures*, Journal of Low Temperature Physics 201, 772-802 (2020)

[19] P. Drude, *Zur Elektronentheorie der Metalle*, Annalen der Physik 306, 566-613 (1900)

[20] R. P. Feynman (R. Phillips), *"Surely You're Joking, Mr. Feynman": Adventures of a Curious Character* New York :W.W. Norton (1984)

[21] R. P. Feynman, *Simulating Physics with Computers*, International Journal of Theoretical Physics 21, 467-488 (1982)

[22] P. Benioff, *The computer as a physical system: A microscopic quantum mechanical Hamiltonian model of computers as represented by Turing machines*, Journal of Statistical Physics 22, 563-591 (1980)

[23] S. Aaronson, *What Makes Quantum Computing So Hard to Explain?*, Quanta Magazine, (2021)

[24] A. K. Lenstra, *Integer Factoring*, Designs, Codes and Cryptography 19, 101-128 (2000)

[25] A. Ambainis, *Quantum search algorithms*, ACM SIGACT News 35, 22-35 (2004)

[26] A. Ambainis, *What Can We Do with a Quantum Computer?*, Institute for Advanced Study (2014)

[27] J. Biamonte, P. Wittek, N. Pancotti, P. Rebentrost, N. Wiebe, and S. Lloyd, *Quantum mahine learning*, Nature 549, 195-202 (2017)

[28] S. Lloyd, *Universal Quantum Simulators*, Science 273, 1073-1078 (1996)

[29] A. I. Gircha, A. S. Boev, K. Avchaciov, P. O. Fedichev, and A. K. Federov, *Training a discrete variational autoencoder for generative chemistry and drug design on a quantum annealer*, arXiv:2108.11644 (2021)

[30] H. S. Zhong, H. Wang, Y. U. Deng, M. C. Chen, L. C. Peng, Y. H. Luo, J. Qin, D. Wu, X. Ding, Y. Hu, P. Hu, X. Y. Yang, W. J. Zhang, H. Li, Y. Li, X. Jiang, L. Gan, G. Yang, L. You, Z. Wang, L. Li, N. L. Liu, C. Y. Lu, and J. W. Pan, *Quantum computational advantage using photons*, Science 370, 1460 - 1463 (2020)

[31] Z. Merali, *First sale for quantum computing*, Nature 474, 18 (2011)

[32] F. Arute et al., *Quantum supremacy using a programmable superconducting processor*, Nature 574, 505-510 (2019)

[33] Y. Wu, W. S. Bao, S. Cao, F. Chen, M. C. Chen, X. Chen, T. H. Chung, H. Deng, Y. Du, D. Fan, and M. Gong, *Strong Quantum Computational Advantage Using a Superconducting Quantum Processor*, Phys. Rev. Lett. 127, 180501 (2021)

[34] Q. Zhu et al., *Quantum Computational Advantage via 60-Qubit 24-Cycle Random Circuit Sampling*, arXiv:2109.03494 (2021)

[35] M. A. Nielsen and I. L. Chuang, *Quantum Computation and Quantum Information*, Cambridge University Press (2000)

[36] M. V. G. Dutt et al., *Quantum register based on individual electronic and nuclear spin qubits in diamond*, Science 316, 1312-1316 (2007)

[37] D. J. Wineland et al., *Experimental issues in coherent quantum-state manipulation of trapped atomic ions*, J. Res. Natl. Inst. Stand. Technol. 103, 259-328 (1998)

[38] D. J. Wineland and R. Blatt, *Entangled states of trapped atomic ions*, Nature 453, 1008-1014 (2008)

[39] A. Wallraff et al., *Strong coupling of a single photon to a superconducting qubit using circuit quantum electrodynamics*, Nature 431, 162-167 (2004)

[40] L. DiCarlo et al., *Demonstration of two-qubit algorithms with a superconducting quantum processor*, Nature 260, 240-244 (2009)

[41] M. Ansmann et al., *Violation of Bell's inequality in Josephson phase qubits*, Nature 461, 504-506 (2009)

[42] J. A. Schreier et al., *Suppressing charge noise decoherence in superconducting charge qubits*, Phys. Rev. B 77, 180502 (2008)

[43] C. Kloeffel and D. Loss, *Prospects for Spin-Based Quantum Computing in Quantum Dots*, Annu. Rev. Condens. Matter Phys. 4, 51-81 (2013)

[44] D. Deutsch, *Quantum theory, the Church-Turing principle and the universal quantum computer*, Proc. R. Soc. Lond. A 400, 97-117 (1985)

[45] P. Shor, *Fault-tolerant quantum computation*, Proceedings of the Symposium on the Foundations of Computer Science, IEEE Press (1996); e-print quant-ph/9605011

[46] L. K. Grover, *Quantun Mechanics Helps in Searching for a Needle in a Haystack*, Phys. Rev. Lett. 79, 325 (1997)

[47] D. Loss, D. P. DiVincenzo, *Quantum Computation with Quantum Dots*, Phys. Rev. A 57, 120 (1998)

[48] A. Kitaev, C. Laumann, *Topological phases and quantum computation*, Lecture notes from 2008 Les Houches summer school "Exact methods in low-dimensional physics and quantum computing", arXiv:0904.2771

[49] A. Kitaev, *Fault-tolerant quantum computation by anyons*, Annals of Physics 303, 2-30 (2003)

[50] M. H. Freedman, A. Kitaev, M. J. Laresen and Z. Wang, *Topological Quantum Computation*, Bull. Amer. Math. Soc. 40, 31-33 (2003)

[51] V. T. Lahtinen, J. K. Pachos, *A Short Introduction to Topological Quantum Computation*, arXiv:1705.04103v4 (2017)

[52] P. Shor, *Algorithms for quantum computation: discrete logarithms and factoring*, Proceedings of the 35th Annual Symposium on Fundamentals of Computer Science, IEEE Press, pp. 124 - 134 (1994)

[53] T. D. Ladd, F. Jelezko, R. Laflamme, Y. Nakamura, C. Monroe and J. L. O'Brien, *Quantum computers*, Nature 464, 45-53 (2010)

[54] D. Kielpinski, C. Monroe, D. J. Wineland, *Architecture for a large-scale ion-trap quantum computer*, Nature 417, 709-711 (2002)

[55] D. Gottesman, *An Introduction to Quantum Error Correction and Fault-Tolerant Quantum Computation*, Proc. Symp. Appl. Math. 68, 13-46 (2010)

[56] D. J. Reilly, *Engineering the quantum-classical interface of solid-state qubits*, npj Quantum Inf. 1, 15011 (2015)

[57] J. M. Gambetta, J. M. Chow, M. Steffen, *Building logical qubits in a superconducting quantum computing system*, npj Quantum Inf. 3, 2 (2017)

[58] S. Takahashi, I. S. Tupitsn, J. van Tol, C. C. Beedle, D. N. Hendrickson, and P. C. Stamp, *Decoherence in crystals of quantum molecular magnets*, Nature 476, 76-79 (2011)

[59] J. Goetz, F. Deppe, P. Eder, M. Fisher, M. Müting, J. Puertas Martinez, S. Pogorzalek, F. Wulschner, E. Xie, and K. G. Federov, *Second-order decoherence mechanisms of a transmon qubit probed with thermal microwave states*, Quantum Sci. Technol. 2, 025002 (2017)

[60] A. Stern, N. H. Lindner, *Topological Quantum Computation - From Basic Concepts to First Experiments*, Science 339, 1179-1184 (2013)

[61] J. Klinovaja, D. Loss, *Parafermions in an Interacting Nanowire Bundle*, Phys. Rev. Lett. 112, 246403 (2014)

[62] J. Klinovaja, D. Loss, *Time-reversal invariant parafermions in interacting Rashba nanowires*, Phys. Rev. B 90, 1-8 (2014)

[63] A. Das, Y. Ronen, Y. Most, Y. Oreg, M. Heiblum, and H. Shrrikman, *Zero-bias peaks and splitting in an Al-InAs nanowire topological superconductor as a signature of Majorana fermions*, Nature Physics 8, 887-895 (2012)

[64] S. M. Albrecht, A. P. Higginbotham, M. Madsen, F. Kuemmeth, T. S. Jespersen, J. Nygard, P. Krogrstup, and C. M. Marcus, *Exponential protection of zero modes in Majorana islands*, Nature 531, 206-209 (2016)

[65] M. T. Deng, C. L. Yu, G. Y. Huang, M. Larsson, P. Caroff, and H. Q. Xu, *Anomalous Zero-Bias Conductance Peak in an Nb-InSb Nanowire-Nb Hybrid Device*, Nano Lett. 12, 6414-6419 (2012)

[66] Y. H. Lee, X. Q. Zhang, W. Zhang, M. T. Chang, C. T. Lin, K. D. Chang, Y. C. Yu, J. T. W. Wang, C. S. Chang, L. J. Li, and T. W. Lin, *Synthesis of Large-Area* MoS_2 *Atomic Layers with Chemical Vapor Deposition*, Adv. Mater. 24, 2320-2325 (2012)

[67] E. J. H. Lee, X. Jiang, M. Houzet, R. Aguado, C. M. Lieber, and S. DeFrancschi, *Spin-resolved Andreev levels and parity crossings in hybrid superconductor-semiconductor nanostructures*, Nature Nanotechnology 9, 79-84 (2014)

[68] R. M. Lutchyn, E. P. A. M. Bakkers, L. P. Kouwenhoven, P. Krogstrup, C. M. Marcus, and Y. Oreg, *Realizing Majorana zero modes in superconductor-semiconductor heterostructures*, arXiv:cond-mat/1707.04899 (2018)

[69] J. Gooth, M. Borg, H. Schmid, V. Schaller, S. Wirths, K. Moselund, M. Luisier, S. Karg, and H. Riel, *Ballistic One-Dimensional InAs Nanowire Cross-Junction Interconnects*, Nano Lett. 17, 2596-2602 (2017)

[70] Y. Huang, X. Duan, Q. Wei, C. M. Lieber, *Directed assembly of one-dimensional nanostructures into functional networks*, Science 291, 630-633 (2001)

[71] Y. Huang, X. Duan, Y. Cui, L. J. Lauhon, K. H. Kim, and C. M. Lieber, *Logic Gates and Computation from Assembled Nanowire Building Blocks*, Science 294, 1313-1317 (2001)

[72] N. A. Melosh, A. Boukai, F. Diana, B. Gerardot, A. Badolato, P. M. Petroff, and J. R. Heath, *Ultrahigh-Density Nanowire Lattices and Circuits*, Science 300, 112-115 (2003)

[73] O. Gül, D. J. van Woerkom, I. van Weperen, D. Car, S. R. Plissard, E. P. A. M. Bakkers, and L. P. Kouwenhoven, *Towards high mobility InSb nanowire devices*, Nanotechnology 26, 215202 (2015)

[74] D. Car, J. Wang, M. A. Verheijen, E. P. A. M. Bakkers, S. R. Plissard, *Rationally Designed Single-Crystalline Nanowire Networks*, Adv. Mater. 26, 4875-7879 (2014)

[75] T. Rieger, D. Rosenbach, D. Vakulov, S. Heedt, T. Schäpers, D. Grützmacher, and M. I. Lepsa, *Crystal Phase Transformation in Self-Assembled InAs Nanowire Junctions on Patterned Si Substrates*, Nano Lett. 16, 1933-1941 (2016)

[76] J. H. Kang, Y. Cohen, Y. Ronen, M. Heiblum, R. Buczko, P. Kacman, R. Popovitz-Biro, and H. Shtrikman, *Crystal Structure and Transport in Merged InAs Nanowires MBE Grown on (001) InAs*, Nano Lett. 13, 5190-5196 (2013)

[77] D. Dalacu, A. Kam, D. G. Austing, and P. J. Poole, *Droplet dynamics in controlled InAs nanowire interconnections* Nano Lett. 13, 2676-2681 (2013)

[78] C. B. Collins, R. O. Carlson, and C. J. Gallagher, *Properties of gold-doped silicon*, Phys. Rev. 105, 1168-1173 (1957) bibitem79 G. Tütüncüoglu, M. de la Mata, D. Deiana, H. Potts, F. Matteini, J. Arbiol, and A. Fontcuberta i Morral, *Towards defect-free 1-D GaAs/AlGaAs heterostructures based on GaAs nanomembranes*, Nanoscale 7, 19453-19460 (2015)

[79] Z. Yang, A. Surrente, G. Tütüncüoglu, K. Galkowski, M. Cazaban-Carraze, F. Amaduzzi, P. Leroux, D. K. Maude, A. Fontcuberta i Morral, and P. Plochocka, *Revealing Large-Scale Homogeneity and Trace Impurity Sensitivity of GaAs Nanoscale Membranes*, Nano Lett. 17, 2979-2984 (2017)

[80] C. Y. Chi, C. C. Chang, S. Hu, T. W. Yeh, S. B. Cronin, and P. D. Dapkus, *Twin-Free GaAs Nanosheets by Selective Area Growth: Implications for Defect-Free Nanostructures*, Nano Lett. 13, 2506-2515 (2013)

[81] M. Friedl, K. Cerveny, P. Weigele, G. Tütüncüoglu, S. Marti-Sanchez, C. Huang, T. Patlatiuk, H. Potts, Z. Sun, M. O. Hill, L. Güniat, W. Kim, M. Zamani, V. G. Dubrovskii, J. Arbiol, L. J. Lauhon, D. M. Zumbühl, and A. Fontcuberta i Morral, *Template-Assisted Scalable Nanowire Networks*, Nano Lett. 18, 2666 (2018)

[82] M. de la Mata, C. Magen, P. Caroff, and J. Arbiol, *Atomic Scale Strain Relaxation in Axial Semiconductor III-V Nanowire Heterostructures*, Nano Lett. 14, 6614-6620 (2014)

[83] M. de la Mata, R. Leturcq, S. R. Plissard, C. Rolland, C. Magen, J. Arbiol, and P. Caroff, *Twin-Induced InSb Nanosails: A Convenient High Mobility Quantum System*, Nano Lett. 16, 825-833 (2016)

[84] M. O. Lipinski, H. Schuler, O. G. Schmidt, K. Eberl, and N. Y. Phillipp, *Strain-induced material intermixing of InAs quantum dots in GaAs*, Appl. Phys. Lett. 77, 1789 (2000)

[85] E. Pehlke, N. Moll, and M. Scheffler, *The Equillibrium Shape of Quantum Dots*, arXiv:cond-mat/9612004 (1996)

[86] N. Moll, M. Scheffler, and E. Pehlke, *Influence on surface stress on the equilibrium shape of strained quantum dots*, Phys. Rev. B 58, 4566-4571 (1998)

[87] D. B. Suyatin, C. Thelander, M. T. Björk, I. Maximov, and L. Samuelson, *Sulfur passivation for ohmic contact formation to InAs nanowires*, Nanotechnology 18, 105307 (2007)

[88] J. G. Belk, D. W. Pashley, C. F. McConville, J. L. Sudijono, B. A. Joyce, and T. S. Jones, *Surface atomic configurations due to dislocation activity in InAs/GaAs(110) heteroepitaxy*, Phys. Rev. B 56, 10289 (1997)

[89] B. Z. Nosho, L. A. Zepeda-Ruiz, R. I. Pelzel, W. H. Weinberg, and D. Maroudas, *Surface morphology in InAs/GaAs(111)A heteroepitaxy: Experimental measurements and computer simulations*, Appl. Phys. Lett. 75, 829-831 (1999)

[90] H. Potts, M. Friedl, F. Amaduzzi, K. Tang, G. Tütüncüoglu, F. Matteini, E. A. LLado, P. C. McIntyre, and A. Fontcuberta i Morral, *From Twinning to Pure Zincblende Catalyst-Free InAs(Sb) Nanowires*, Nano Lett. 16, 637-643 (2016)

[91] J. M. Garcia, G. Medeiros-Ribeiro, K. Schmidt, T. Ngo, J. L. Feng, A. Lorke, J. Kotthaus, and P. M. Petroff, *Intermixing and shape changes during the formation of InAs self-assembled quantum dots*, Appl. Phys. Lett. 71, 2014 (1997)

[92] M. Fahed, L. Desplanque, D. Troadec, G. Patriarche, and X. Wallart, *Selective area heteroepitaxy of GaSb on GaAs (001) for in-plane InAs nanowire achievement*, Nanotechnology 27, 505301 (2016)

[93] A. Trampert, E. Tournie, and K. H. Ploog, *Influence of the growth mode on the microstructure of highly mismatched InAs/GaAs heterostructures*, Physcia Status Solidi (a) 145, 481-489 (1994)

[94] L. E. Ocola and A. Stein, *Effect of cold development on improvement in electron-beam nanopatterning resolution and line roughness*, J. Vac. Sci. Technol. B Microelectron. Nanom. Struct. 24, 3061 (2006)

[95] C. W. J. Beenakker and H. van Houten, *Boundary scattering and weak localization of electrons in a magnetic field*, Phys. Rev. B 38, 3232-3240 (1988)

[96] S. Hikami, A. I. Larkin, and Y. Nagaoka, *Spin-Orbit Interaction and Magnetoresistance in the Two Dimensional Random System*, Prog. Theor. Phys. 63, 707-710 (1980)

[97] B. L. Al'tshuler and A. Aronov, *Magnetoresistance of thin films and of wires in a longitudinal magnetic field*, JETP Lett. 33, 499 (1981)

[98] Z. Sun, O. Hazut, R. Yerushalmi, L. J. Lauhon, and D. N. Seidman, *Criteria and considerations for preparing atom-probe tomography specimens of nanomaterials utilizing an encapsulation methodology*, Ultramicroscopy 184, 225-233 (2018)

[99] K. Thompson, D. Lawrence, D. J. Larson, J. D. Olson, T. F. Kelly, and B. Gorman, *In situ site-specific preparation for atom probe tomography*, Ultramicroscopy 107, 131-139 (2007)

[100] D. J. Lockwood, G. Yu, and N. L. Rowell, *Optical phonon frequencies and damping in AlAs, GaP, GaAs, InP, InAs and InSb studied by oblique incidence infrared spectroscopy*, Solid State Commun. 136, 404-409 (2005)

[101] M. Cantoro, A. V. Klekachev, A. Nourbakhsh, B. Soree, M. M. Heyns, and S. De Gendt, *Long-wavelength confined optical phonons in InAs nanowires probed by Raman spectroscopy*, Eur. Phys. J. B 79, 423-428 (2011)

[102] Supporing Information to M. Friedl et al., *Template-Assisted Scalable Nanowire Networks*, Nano Lett. 18, 2666 (2018)

[103] L. Pavesi, G. Mariotto, J. F. Carlin, A. Rudra, and R. Houdre, *Raman study of a single InP/InAs/InP strained quantum well*, Solid State Commun. 84, 705-709 (1992)

[104] S. Birner, T. Zibold, T. Andlauer, T. Kubis, M. Sabathil, A. Trellakis, and P. Vogl, *nextnano: General Purpose 3-D Simulations*, IEEE Trans. Electron Devices 54, 2137-2142 (2007)

[105] F. Glas, *Critical dimensions for the plastic relaxation of strained axial heterostructures in free-standing nanowires*, Phys. Rev. B 74, 121302 (2006)

[106] X. Zhang, V. G. Dubrovskii, N. V. Sibirev, and X. Ren, *Analytical study of elastic relaxation and plastic deformation in nanostructures on lattice mismatched substrates*, Cryst. Growth Des. 11, 5441-5448 (2011)

[107] V. G. Dubrovskii, N. V. Sibirev, X. Zhang, and R. A. Suris, *Stress-driven nucleation of three-dimensional crystal islands: From quantum dots to nanoneedles*, Cryst. Growth Des. 10, 3949-3955 (2010)

[108] V. G. Dubrovskii, V. Consonni, A. Trampert, L. Geelhaar, and H. Riechert, *Scaling thermodynamic model for the self-induced nucleation of GaN nanowires*, Phys. Rev. B 85, 1-6 (2012)

[109] J. Y. Shen, C. Chatillon, I. Ansara, A. Watson, B. Rugg, and T. Chart, *Optimisation of the thermodynamic and phase diagram data in the ternary As-Ga-In system*, Calphad 19, 215-226 (1995)

[110] D. Schlenker, T. Miyamoto, Z. Pan, F. Koyama, and K. Iga, *Miscibility gap calculation for* $Ga_{1-x}In_xN_yAs_{1-y}$ *including strain effects*, J. Cryst. Growth 196, 67-70 (1999)

[111] S. Chakravarty and A. Schmid, *Weak localization: The quasiclassical theory of electrons in a random potential*, Phys. Rep. 140, 193-236 (1986)

[112] B. L. Al'tshuler, D. Khmel'nitzkii, A. I. Larkin, and P. A. Lee, *Magnetoresistance and Hall effect in a disordered two-dimensional electron gas*, Phys. Rev. B 22, 5142-5153 (1980)

[113] I. van Weperen, B. Tarasinski, E. Eeltink, V. S. Pribiag, S. R. Plissard, E. P. A. M. Bakkers, L. P. Kouwenhoven, and M. Wimmer, *Spin-orbit interaction in InSb nanowires*, Phys. Rev. B 91, 1-5 (2015)

[114] D. Liang and X. P. A. Gao, *Strong Tuning of Rashba Spin-Orbit Interaction in Single InAs Nanowires*, Nano Lett. 12, 3263-3267 (2012)

[115] A. E. Hansen, M. T. Björk, C. Fasth, C. Thelander, and L. Samuelson, *Spin relaxation in InAs nanowires studied by tunable weak antilocalization*, Phys. Rev. B 71, 1-5 (2005)

[116] B. Cord, J. Lutkenhaus, and K. K. Berggren, *Optimal temperature for development of poly(methylmethacrylate)*, J. Vac. Sci. Technol. B 25, 2013-2016 (2007)

[117] Image from http://en.wikipedia.org/wiki/Atomic_layer_deposition (image part of public domain)

[118] J. Robertson, *High dielectric constant oxides*, Eur. Phys. J. Appl. Phys. 28, 265-291 (2004)

[119] M. Balasubramanian, L. K. Bera, S. Mathew, N. Balasubramanian, V. Lim, M. S. Joo, and B. J. Cho, *Wet etching characteristics and surface morphology evaluation of MOCVD grown* HfO_2 *film*, Thin Solid Films 462-463, 101-105 (2004)

[120] V. Lowalakar and S. Raghavan, *Etching of zirconium oxide, hafnium oxide, and hafnium silicates in dilute hydrofluoric acid solutions*, Journal of Materials Research 19, 1149-1156 (2004)

[121] M. S. Tyagi, *Electrical properties of metal-GaAs Schottky barriers*, Surface Science 64, 323-333 (1977)

[122] F. Krizek, J. E. Sestoft, P. Aseev, S. Marti-Sanchez, S. Vaitiekenas, L. Casparis, S. A. Khan, Y. Liu, T. Stankevic, A. M. Whiticar, A. Fursina, F. Boekhout, R. Koops, E. Uccelli, L. P. Kouwenhoven, C. M. Marcus, J. Arbiol, and P. Krogstrup, *Field effect enhancement in buffered quantum nanowire networks*, arXiv:1802.07808v2 (2018)

[123] S. Alagha, S. Estevez Hernandez, C. Blömers, T. Stoica, R. Calarco, and T. Schäpers, *Universal conductance fluctuations and localization effects in InN nanowires connected in parallel*, Journal of Applied Physics 108, 113704 (2010)

[124] C. W. J. Beenakker and H. van Houten, *Quantum Transport in Semiconductor Nanostructures*, Solid State Physics 44, 1-228 (1991)

[125] V. K. Dugaev and D. E. Khmel'nitskii, *Magnetoresistance of metal films with low impurity concentrations in a parallel magnetic field*, JETP 59, 10387 (1984)

[126] P. G. de Gennes and M. Tinkham, *Superconductivity of Metals and Alloys*, Benjamin, New York, Ch. 8 (1966)

[127] L. Zheng and S. Das Sarma, *Coulomb scattering lifetime of a two-dimensional electron gas*, Phys. Rev. B 53, 9964 (1996)

[128] B. L. Al'tshuler and A. G. Aronov, *Electron-Electron Interaction in Disordered Systems*, Elsevier, Amsterdam (1985)

[129] A. G. Huibers, M. Switkes, C. M. Marcus, K. Campman, and A. C. Gossard, *Dephasing in Open Quantum Dots*, Phys. Rev. Lett. 81, 200-203 (1998)

[130] K. K. Choi, D. C. Tusi, and K. Alavi, *Dephasing time and one-dimensional localization of two-dimensional electrons in GaAs / AlxGa1-xAs Heterostructures*, Phys. Rev. B 36, 7551 (1987)

[131] C. Kurdak, A. M. Chang, A. Chin, and T. Y. Chang, *Quantum interference effects and spin-orbit interaction in quasi-one-dimensional wires and rings*, Phys. Rev. B 46, 6846 (1992)

[132] B. L. Al'tshuler, V. E. Kravtsov, and I. V. Lerner, *Statistical properties of mesoscopic fluctuations and similarity theory*, JETP Lett. 43, 342-344 (1986)

[133] P. A. Lee and A. D Stone, *Universal Conductance Fluctuations in Metals*, Phys. Rev. Lett. 55, 1622 (1985)

[134] P. A. Lee, A. D. Stone, and H. Fukuyama, *Universal conductance fluctuations in metals: Effects of finite temperature, interactions, and magnetic field*, Phys. Rev. B 35, 1039 (1987)

[135] R. Landauer, *Spatial Variation of Currents and Fields Due to Localized Scatterers in Metallic Conduction*, IBM Journal of Research and Development 1, 223-231 (1957)

[136] J. P. Bird, *The low-temperature analysis of narrow GaAs/AlGaAs heterojunction wires*, J. Phys.: Condens. Matter 3, 2897 (1991)

[137] B. L. Al'tshuler and A. G. Aronov, *Magnetoresistance of thin films and of wires in a longitudinal magnetic field*, JETP Lett. 33, 499 (1981)

[138] C. W. J. Beenakker and H. van Houten, *Flux-cancellation effect on narrow-channel magnetoresistance fluctuations*, Phys. Rev. B 37, 6544-6546 (1988)

[139] S. Estevez Hernandez, M. Akabori, K. Sladek, Ch. Volk, S. Alagha, H. Hardtdegen, M. G. Pala, N. Demarina, D. Grützmacher, and Th. Schäpers, *Spin-orbit coupling and phase coherence in InAs nanowires*, Phys. Rev. B 82, 235303 (2010)

[140] G. Petersen, S. Estevez Hernandez, R. Calarco, N. Demarina, and Th. Schäpers, *Spin-orbit copuling and phase-coherent transport in InN nanowires*, Phys. Rev. B 80, 125231 (2009)

[141] Ch. Blömers, T. Grap, M. I. Lepsa, J. Moers, St. Trellenkamp, D. Grützmacher, H. Lüth, and Th. Schäpers, *Hall effect measurements on InAs nanowires*, Appl. Phys. Lett. 101, 152106 (2016)

[142] B. L. Al'tshuler, A. G. Aronov, and D. E. Khmelnitsky, *Effects of electron-electron collisions with small energy transfers on quantum localisation*, J. Phys. C: Solid State Phys. 15, 7367 (1982)

[143] Ch. Blömers, Th. Schäpers, T. Richter, R. Calarco, H. Lüth, and M. Marso, *Temperature dependence of the phase-coherence length in InN nanowires*, Appl. Phys. Lett. 92, 132101 (2008)

[144] B. L. Al'tshuler and A. G. Aronov, *Damping of one-electron excitations in metals*, JETP Lett. 30, 514-516 (1979)

[145] S. Kettemann, *Dimensional Control of Antilocalization and Spin Relaxation in Quantum Wires*, Phys. Rev. Lett. 98, 176808 (2007)

[146] R. Winkler, *Spin-Orbit Coupling Effects in Two-Dimensional Electron and Hole Systems*, Springer, Berlin (2003)

[147] Y. Bychkov, E. I. Rashba, *Properties of a 2D electron gas with lifted spectral density*, JETP Lett. 39, 78 (1984)

[148] G. Dresselhaus, *Spin-Orbit Coupling Effects in Zinc Blende Structures*, Phys. Rev. 100, 580 (1955)

[149] J. J. Sakurai, *Advanced Quantum Mechanics*, Addison-Wesley series in advanced physics (Addison-Wesley, Reading, Mass., 1998)

[150] M. J. Carballido, C. Kloeffel, D. M. Zumbühl, and D. Loss, *Low-symmetry nanowire cross-sections for enhanced Dresselhaus spin-orbit interaction*, Phys. Rev. B 103, 195444 (2021)

[151] J. R. Weber, A. Janotti, and C G. Van de Walle, *Intrinsic and extrinsic causes of electron accumulation layers on InAs surfaces*, Appl. Phys. Lett. 97, 192106 (2010)

[152] N. Taoka, M. Yokoyama, S. H. Kim, R. Suzuki, S. Lee, R. Iida, T. Hoshii, W. Jevasuwan, T. Maeda, T. Yasuda, O. Ichikawa, N. Fukuhara, M. Hata, M. Takenaka, and S. Takagi, *Impact of Fermi level pinning inside conduction band on electron mobility in InGaAs metal-oxide semiconductor field-effect transistors*, Appl. Phys. Lett. 103, 143509 (2013)

[153] F. Dettwiler, J. Fu, S. Mack, P. J. Weigele, J. C. Egues, D. D. Awschalom, and D. M. Zumbühl, *Stretchable Persistent Helices in GaAs Quantum Wells*, Phys. Rev. X 7, 031010 (2017)

[154] A. E. Hansen, M. T. Björk, C. Fasth, C. Thelander, and L. Samuelson, *Spin relaxation in InAs nanowires studied by tunable weak antilocalization*, Phys. Rev. B 71, 205328 (2005)

[155] D. Grundler, *Large Rashba Splitting in InAs Quantum Wells due to Electron Wave Function Penetration into the Barrier Layers*, Phys. Rev. Lett. 84, 6074 (2000)

[156] M. I. D'Yakonov, and V. I. Perel, *Spin Orientation of Electrons Associated with the Inter-band Absorption of Light in Semiconductors*, JETP 33, 1053 (1971)

[157] G. Bergman, *Influence of Spin-Orbit Coupling on Weak Localization*, Phys. Rev. Lett. 48, 1046-1049 (1982)

[158] C. Kurdak, A. M. Chang, A. Chin, and T. Y. Chang, *Quantum interference effects and spin-orbit interaction in quasi-one-dimensional wires and rings*, Phys. Rev. B 46, 6846-6856 (1992)

[159] S. Hikami, A. I. Larkin, and Y. Nagaoka, *Spin-Orbit Interaction and Magnetoresistance in the Two Dimensional Random System*, Progress of Theoretical Physics 63, 707-710 (1980)

[160] Y. Kawaguchi, I. Takayanagi, and S. Kawaji, *Spin-Orbit Interaction in Two Dimensional Systems in InAs n-Inversion Layers*, J. Phys. Soc. Jpn. 56, 1293-1296 (1987)

[161] S. Maekawa and H. Fukuyama, *Magnetoresistance in Two-Dimensional Disordered Systems: Effects of Zeeman Splitting and Spin-Orbit Scattering*, J. Phys. Soc. Jpn. 50, 2516-2524 (1981)

[162] S. Chakravarty and A. Schmid, *Weak Localization: The Quasiclassical Theory of Electrons in a Random Potential*, Physics Reports 140, 193-236 (1986)

[163] M. Friedl, K. Cerveny, C. Huang, D. Dede, M. Samani, M. O. Hill, N. Morgan, W. Kim, L. Güniat, J. Segura-Ruis, L. J. Lauhon, D. M. Zumbühl, and A. Fontcuberta i Morral, *Remote Doping of Scalable Nanowire Branches*, Nano Lett. 20, 3577-3584 (2020)

[164] D. Hisamoto, W. C. Lee, J. Kedzierski, E. Anderson, H. Takeuchi, K. Asano, T. J. King, J. Bokor, and C. Hu, *A folded-channel MOSFET for deep sub-tenth micro era*, IEE International Electron Devices Meeting Technical Digest, 1032-1034 (1998)

[165] L. C. Camenzind, S. Geyer, A. Fuhrer, R. J. Warburton, D. M. Zumbühl, and A. V. Kuhlmann, *A hole spin qubit in a fin field-effect transistor above 4 kelvin*, Nature Electronics 5, 178-183 (2022)

[166] B. S. Doyle, S. Datta, M. Doczy, S. Hareland, B. Jin, J. Kavalieros, T. Linton, A. Murthy, R. Rios, and R. Chau, *High Performance Fully-Depleted Tri-Gate CMOS Transistors*, IEEE Electron Device Letters 24, 263-265 (2003)

[167] C.C. Wu, D.W. Lin, A. Keshavarzi, C.H. Huang, C.T. Chan, C.H. Tseng, C.L. Chen, C.Y. Hsieh, K.Y. Wong, M.L. Cheng, T.H. Li, Y.C. Lin, L.Y. Yang, C.P. Lin, C.S. Hou, H.C. Lin, J.L. Yang, K.F. Yu, M.J. Chen, T.H. Hsieh, Y.C. Peng, C.H. Chou, C.J. Lee, C.W. Huang, C.Y. Lu, F.K. Yang, H.K. Chen, L.W. Weng, P.C. Yen, S.H. Wang, S.W. Chang,

S.W. Chuang, T.C. Gan, T.L. Wu, T.Y. Lee, W.S. Huang, Y.J. Huang, Y.W. Tseng, C.M. Wu, Eric Ou-Yang, K.Y. Hsu, L.T. Lin, S.B. Wang, T.M. Kwok, C.C. Su, C.H. Tsai, M.J. Huang, H.M. Lin, A.S. Chang, S.H. Liao, L.S. Chen, J.H. Chen, P.S. Lim, X.F. YU, S.Y. Ku, Y.B. Lee, P.C. Hsieh, P.W. Wang, Y.H. Chiu, S.S. Lin, H.J. Tao, M. Cao, and Y.J. Mii, *High Performance 22/20nm FinFET CMOS Devices with Advanced High-K/Metal Gate Scheme*, IEDM (2010)

[168] E. Garnett, L. Mai, and P. Yang, *Introduction: Nanomaterials/Nanowires*, Chem. Rev. 119, 8955-8957 (2019)

[169] J. V. Holm, H. I. Jorgensen, P. Krogstrup, J. Nygard, H. Liu, and M. Aagesen, emphSurface-passivated GaAsP single-nanowire solar cells exceeding 10% efficiency grown on silicon, Nat. Commun. 4, 1498 (2013)

[170] P. Krogstrup, H. I. Jorgensen, M. Heiss, O. Demichel, J. V. Holm, M. Aagesen, J. Nygard, and A. Fontcuberta i Morral, *Single-nanowire solar cells beyond the Shockley-Queisser limit*, Nat. Photonics 7, 306-310 (2013)

[171] R. R. LaPierre, A. C. E. Chia, S. J. Gibson, C. M. Haapamaki, J. Boulanger, R. Yee, P. Kuyanov, J. Zhang, N. Tajik, N. Jewell, and K. M. A. Rahman, *III-V nanowire photovoltaics: Review of design for high efficiency*, Phys. Status Solidi RRL 7, 815-830 (2013)

[172] A. D. Mallorqui, E. Alarcon-Llado, E. Russo-Averchi, G. Tütücüoglu, F. Matteini, D. Rüffer, and A. Foncuberta i Morral, *Characterization and analysis of InAs/p-Si heterojunction nanowire-based solar cell*, J. Phys. D: Appl. Phys 47, 394017 (2014)

[173] A. D. Mallorqui, E. Alarcon-Llado, I. C. Mundet, A. Kiani, B. Demaurex, S. De Wolf, A. Menzel, M. Zacharias, and A. Fontcuberta i Morral, *Field-effect passivation on silicon nanowire solar cells*, Nano Res. 8 , 673-681 (2015)

[174] J. Svensson, N. Anttu, N. Vainorius, B. M. Borg, and L. E. Wernersson, *Diameter-dependent photocurrent in InAsSb nanowire infrared photodectors*, Nano Lett. 13, 1380-1385 (2013)

[175] T. Burgess, P. Caro, Y. Wang, B. H. Badada, H. E. Jackson, L. M. Smith, Y. Guo, H. H. Tan, C. Jagadish, and P. Caroff, *Zn3As2 Nanowires and Nanoplatelets: Highly Efficient*

Infrared Emission and Photodetection by an Earch Abundant Material, Nano Lett. 15, 378-385 (2015)

[176] M. Robson, K. M. Azizur-Rahman, D. Parent, P. Wojdylo, D. A. Thompson, and R. R. LaPierre, *Multispectral absorptance from large-diameter InAsSb nanowire arrays in a single epitaxial growth on silicon*, Nano Futures 1, 035001 (2017)

[177] R. R. Lapierre, M. Robson, K. M. Azizur-Rahman, and P. A. Kuyanov, *A review of III-V nanowire infrared photodetectors and sensors*, J. Phys. D: Appl. Phys. 50, 123001 (2017)

[178] D. Saxena, S. Mokkapati, P. Parkinson, N. Jiang, Q. Gao, H. H. Tan, and C. Jagadish, *Optically pumped room-temperature GaAs nanowire lasers*, Nat. Photonics 7, 963-968 (2013)

[179] B. Mayer, D. Rudolph, J. Schnell, S. Morkötter, J. Winnerl, J. Treu, K. Müller, G. Bracher, G. Abstreiter, and G. Koblmüller, *Lasing from individual GaAs-AlGaAs core-shell nanowires up to room temperature*, Nat. Commun. 4, 2931 (2013)

[180] J. Tatebayashi, S. Kako, J. Ho, Y. Ota, S. Iwamoto, and Y Arakawa, *Room-temperature lasing in a single nanowire with quantum dots*, Nat. Photonics 9, 501-505 (2015)

[181] T. Burgess, D. Saxena, S. Mokkapati, Z. Li, C. R. Hall, J. A. Davis, Y. Wang, L. M. Smith, L. Fu, and P. Caroff, *Doping-enhanced radiative efficiency enables lasing in unpassivated GaAs nanowires*, Nat. Commun. 7, 11927 (2016)

[182] E. Bermudez-Urena, G. Tutuncuoglu, J. Cuerda, C. L. C. Smith, J. Bravo-Abad, S. I. Bozhevolnyi, A. Fontcuberta i Morral, F. J. Garcia-Vidal, and R. Quidant, *Plasmonic Waveguide-Integrated Nanowire Laser* Nano Lett. 17, 747-754 (2017)

[183] J. Claudon, J. Bleuse, N. S. Malik, M. Bazin, P. Jaffrennou, N. Gregersen, C. Sauvan, P. Lalanne, and J. M. Gerard, *A highly efficient single-photon source based on a quantum dot in a photonic nanowire*, Nat. Photonics 3, 116 (2010)

[184] M. Heiss, Y. Fontana, A. Gustafsson, G. Wüst, C. Magen, D. D. O'Regan, J. W. Luo, B. Ketterer, S. Conesa-Boj, A. V. Kuhlmann, J. Houel, E. Russo-Averchi, J. R. Morante, M. Cantoni, N. Marzari, J. Arbiol, A. Zunger, R. J. Warburton, and A. Fontcuberta i Morral, *Self-assembled quantum dots in a nanowire system for quantum photonics*, Nat. Mater. 14, 400-406 (2015)

[185] J. Deng, Y. Su, D. Liu, P. Yang, B. Liu, and C. Liu, *Nanowire Photoelectrochemistry*, Chem. Rev. 119, 9221-9259 (2019)

[186] C. Jia, Z Lin, Y. Huang, and X. Duan, *Nanowire Electronics: From Nanoscale to Macroscale*, Chem. Rev 119, 9074-9135 (2019)

[187] P. Krogrstrup, N. L. B. Ziino, W. Chang, S. M. Albrecht, M. H. Madsen, E. Johson, J. Nygard, C. M. Marcus, and T. S. Jesperson, *Epitaxy of semiconductor-superconductor nanowires*, Nat. Mater. 14, 400-406 (2015)

[188] S. R. Plissard, I. van Weperen, D. Car, M. A. Verheijen, G. W. G. Immink, J. Kammhuber, L. J. Cornelissen, D. B. Szombati, A. Geresdi, S. M. Frolov, L. P. Kouwenhoven, and E. P. A. M. Bakkers, *Formation and electronic properties of InSb nanocrosses*, Nat. Nanotechnol. 8, 859-864 (2013)

[189] D. Car, J. Wang, M. A. Verheijen, E. P. A. M. Bakkers, and S. R. Plissard, *Rationally Designed Single-Crystalline Nanowires Networks*, Adv. Mater. 26, 4875-4879 (2014)

[190] S. Gazibegovic, D. Car, H. Zhang, S. C. Balk, J. A. Logan, M. W. A. de Moor, M. C. Cassidy, R. Schmits, D. Xu, G. Wang, P. Krogstrup, R. L. M. Op het Veld, K. Zuo, Y. Vos, J. Shen, D. Bouman, B. Shojaei, D. Pennachio, J. S. Lee, P. J. van Veldhoven, S. Koelling, M. A. Verheijen, L. P. Kouwenhoven, C. J. Palmstrom, and E. P. A. M. Bakkers, *Epitaxy of advanced nanowire quantum devices*, Nature 548, 434-438 (2017)

[191] J. H. Kang, M. Galicka, P. Cacman, and H. Shtrikman, *Wurtzite/Zinc-Blende 'K'-shape InAs Nanowires with Embedded Two-Dimensional Wurtzite Plates*, Nano Lett. 17, 531-537 (2017)

[192] L. Güniat, P. Caroff, and A. Fontcuberta i Morral, *Vapor Phase Growth of Semiconductor Nanowires: Key Developments and Open Questions*, Chem. Rev. 119, 8958-8971 (2019)

[193] M. Friedl, K. Cerveny, P. Weigele, Gozde Tütüncüoglu, S. Marti-Sanchez, C. Huang, T. Patlatiuk, H. Potts, Z. Sun, M. O. Hill, L. Güniat, W. Kim, M. Zamani, V. G. Dubrovskii, J. Arbiol, L. J. Lauhon, D. M. Zumbühl, and A. Fontcuberta i Morral, *Template-Assisted Scalable Nanowire Networks*, Nano Lett. 18, 2666-2671 (2018)

[194] F. Krizek, J. E. Sestoft, P. Aseev, S. Marti-Sanchez, S. Vaitiekenas, L. Casparis, S. A. Khan, Y. Liu, T. Stankeveic, A. M. Whiticar, A. Fursina, F. Boekhout, R. Koops, E. Uccelli, L. P. Kouwenhoven, C. M. Marcus, J. Arbiol, and P. Krogstrup, *Field effect enhancement in buffered quantum nanowire networks*, Phys. Rev. Mat. 2, 093401 (2018)

[195] S. Vaitiekenas, A. M. Whiticar, M. T. Deng, F. Krizek, J. E. Sestoft, C. J. Palmstrom, S. Marti-Sanchez, J. Arbiol, P. Krogrstrup, L. Casparis and C. M. Marcus, *Selective-Area-Grown Semiconductor-Superconductor Hybrids: A Basis for Topological Networks*, Phys. Rev. Lett. 121, 147701 (2018)

[196] L. Desplanque, A. Bucamp, D. Troadec, G. Patriache, and X Wallart, *In-plane InSb nanowires grown by selective area molecular beam epitaxy on semi-insulating substrate*, Nanotechnology 29, 305705 (2018)

[197] J. S. Lee, S. Choi, M. Pendharkar, D. J. Pennachio, B. Markman, M. Seas, S. Koelling, M. A. Verheijen, L. Casparis, K. D. Petersson, I. Petkovic, V. Schaller, M. J. W. Rodwell, C. M. Marcus, P. Krogrstrup, L. P. Kouwenhoven, E. P. A. M. Bakkers, and C. J. Palmstrom, *Selective-area chemical beam epitaxy of in-plane InAs one-dimensional channels grown on InP(001), InP(111)B, and InP(011) surfaces*, Phys. Rev. Materials 3, 084606 (2019)

[198] H. S. Karlsson, R. Viselga, and U. O. Karlsson, *Electron accumulation at the InAs(110) cleavage surface*, Surf. Sci. 402-404, 590-594 (1998)

[199] T. Bryllert, L. E. Wernersson, L. Froberg, and L. Samuelson, *Vertical high-mobility wrap-gated InAs nanowire transistor*, IEEE Electron Device Lett. 27, 323-325 (2006)

[200] T. Tanaka, K. Tomioka, S. Hara, J. Motohisa, E. Sano, and T. Fukui, *Vertical Surrounding Gate Transistors Using Single InAs Nanowires Grown on Si Substrates*, Appl. Phys. Express 3, 025003 (2010)

[201] C. Blömers, T. Grap, M. I. Lepsa, J. Moers, S. Trellenkamp, D. Grützmacher, D. Lüth, and T. Schäpers, *Hall effect measurements on InAs nanowires*, Appl. Phys. Lett 101, 152106 (2012)

[202] A. Konar, J. Mathew, K. Nayak, M. Bajaj, R. K. Pandey, S. DharaK. V. R. M. Murali, and M. M. Deshmukh, *Carrier Transport in High Mobility InAs Nanowire Junctionless Transistors*, Nano Lett. 15, 1684-1690 (2015)

[203] H. Potts, M. Friedl, F. Amaduzzi, K. Tang, G. Tütüncüoglu, F. Matteini, E. Alarcon-Llado, P. C. P. McIntyre, and A. Foncuberta i Morral, *From Twinning to Pure Zincblende Catalyst-Free InAs(Sb) Nanowires*, Nano Lett. 16, 637-643 (2016)

[204] H. J. Joyce, C. J. Docherty, Q. Gao, H. H. Tan, C. Jagadish, J. Lloyd-Hughes, L. M. Herz, and M. B. Johnston, *Electronic properties of GaAs, InAs and InP nanowires studied by terahertz spectroscopy*, Nanotechnology 24, 214006 (2013)

[205] J. L. Boland, F. Amaduzzi, S. Sterzl, H. Potts, L. M. Herz, A. Fontcuberta i Morral, and M. B. Johnston, *High Electron Mobility and Insights into Temperature-Dependent Scattering Mechanisms in InAsSb Nanowires*, Nano Lett. 18, 3703-3710 (2018)

[206] T. C. Harman, H. L. Goering, and A. C. Beer, *Electrical properties of n-type InAs*, Phys. Rev. 104, 1562-1564 (1956)

[207] J. J. Hou, F. Wang, N. Han, F. Xiu, S. Yip, M. Fang, H. Lin, T. F. Hung, and J. C. Ho, *Stoichiometric Effect on Electrical, Optical, and Structural Properties of Composition-Tunable In x Ga 1- x As Nanowires*, ACS Nano 6, 9320-9325 (2012)

[208] D. C. Tsui, H. L. Stormer, and A. C. Gossard, *Two-Dimensional Magnetotransport in the Extreme Quantum Limit*, Phys. Rev. Lett. 48, 1559-1562 (1982)

[209] K. von Klitzing, *The quantized Hall effect*, Rev. Mod. Phys. 48 519-531 (1986)

[210] H. L. Stormer, *Nobel Lecture: Thre fractional quantum Hall effect*, Rev. Mod. Phys. 71, 875-889 (1999)

[211] J. Shabani, M. Kjaergaard, H. J. Suominen, Y. Kim, F. Nichele, K. Pakrouski, T. Stankevic, R. M. Lutchyn, P. Krogrstrup, R. Feidenhans'l, S. Kraemer, C. Nayak, M. Troyer, C. M. Marcus, and C. J. Palmstrom, *Two-Dimensional epitaxial superconductor-semiconductor heterostructures: A platform for topological superconducting networks*, Phys. Rev. B 93, 155402 (2016)

[212] M. Kjaergaard, F. Nichele, H. J. Suominen, M. P. Nowak, M. Wimmer, A. R. Akhmerov, J. A. Folk, K. Flensberg, J. Shabani, C. J. Palmstrom, and C. M. Marcus, *Quantized conductance doubling and hard gap in a two-dimensional semiconductor-superconductor heterostructure*, Nat. Commun. 7, 12841 (2016)

[213] F. Nichele, A. C. C. Drachmann, A. M. Whiticar, E. C. T. O'Farrell, H. J. Suominen, A. Fornieri, T. Wang, G. C. Gardner, C. Thomas, A. T. Hatke, P. Krogstrup, M. J. Manfra, K. Flensberg, and C. M. Marcus, *Scaling of Majorana Zero-Bias Conductance Peaks*, Phys. Rev. Lett. 119, 136803 (2017)

[214] H. J. Suominen, M. Kjaergaard, A. R. Hamilton, J. Shabani, C. J. Palmstrom, C. M. Marcus, and F. Nichele, *Zero-Energy Modes from Coalescing Andreev States in a Two-Dimensional Semiconductor-Superconductor Hybrid Platform*, Phys. Rev. Lett. 119, 176805 (2017)

[215] M. Gonshorek, J. F. Carlin, E. Feltin, M. A. Py, and N. Grandjean, *High electron mobility lattice-matched AlInN/GaN field-effect transistor heterostructures*, Appl. Phys. Lett. 89, 062106 (2006)

[216] J. A. Del Alamo, *The high-electron mobility transistor at 30: Impressive accomplishments and exciting prospects*, 2011 International Conference on Compound Semiconductor Manufacturing Technology, CS MANTECH 2011 (2011)

[217] V. Umansky, M. Heiblum, Y. Levinson, J. Smet, J. Nübler, and M. Dolev, *MBE growth of ultra-low disorder 2DEG with mobility exceeding 35x10 6 cm2/Vs*, J. Cryst. Growth 311, 1658-1661 (2009)

[218] M. J. Manfra, *Molecular Beam Epitaxy of Ultra-High-Quality AlGaAs/GaAs Heterostructures: Enabling Physics in Low-Dimensional Electronic Systems*, Annu. Rev. Condens. Matter. Phys. 5, 347-373 (2014)

[219] J. L. Boland, S. Conesa-Boj, P. Parkinson, G. Tütüncüoglu, F. Matteini, D. Rüffner, A. Casadei, F. Maduzzi, F. Jabeen, C. L. Davies, H. J. Joyce, L. M. Herz, A. Fontcuberta i Morral, and M. B. Johnston, *Modulation Doping of GaAs/AlGaAs Core-Shell Nanowires With Effective Defect Passivation and High Electron Mobility*, Nano Lett. 15, 1336-1342 (2015)

[220] J. L. Boland, G. Tütüncüoglu, J. Q. Gong, S. Conesa-Boj, C. L. Davies, L. M. Herz, A. Fontcuberta i Morral, and M. B. Johnston, *Towards higher electron mobility in modulation doped GaAs/AlGaAs core shell nanowires*, Nanoscale 9, 7839-7846 (2017)

[221] S. Funk, M. Royo, I. Zardo, D. Rudolph, S. Morkötter, B. Mayer, J. Becker, A. Bechtold, S. Matich, M. Döblinger, M. Bichler, G. Koblmüller, J. J. Finley, A. Bertoni, G. Goldoni, and G. Abstreiter, *High Mobility One- and Two-Dimensional Electron Systems in Nanowire-Based Quantum Heterostructures*, Nano Lett. 13, 6189-6196 (2013)

[222] K. Tomioka, M. Yoshimura, and T. Fukui, *A III-V nanowire channel on silicon for high-performance vertical transistors*, Nature 488, 189-192 (2012)

[223] D. Leonard, M. Krishnamurthy, C. M. Reaves, S. P. Denbaars, and P. M. Petroff, *Direct formation of quantum-sized dots from uniform coherent islands of InGaAs on GaAs surfaces*, Appl. Phys. Lett. 63, 3203 (1993)

[224] W. P. Gillin, K. P. Homewood, L. K. Howard, and M. T. Emeny, *Thermal interdiffusion in InGaAs/GaAs strained quantum wells as a function of doping density*, Superlattices Microstruct. 9, 39-42 (1991)

[225] O. M. Khreis, K. P. Homewood, W. P. Gillin and K. E. Singer, *Intermixing in GaAsSb/GaAs single quantum wells*, J. Appl. Phys. 84, 4017-4019 (1998)

[226] O. M. Khreis, K. P. Homewood, and W. P. Gillin, *Interdiffusion in InGaAs/GaAs: The effect of growth conditions*, J. Appl. Phys. 84, 232-236 (1998)

[227] M. Albani, R. Bergamaschini, M. Salvalaglio, A. Voigt, L. Miglio, and F. Montalenti, *Competition Between Kinetics and Thermodynamics During the Growth of Faceted Crystal by Phase Field Modeling*, Phys. Status Solidi B 256, 1800518 (2019)

[228] N. Moll, A. Kley, E. Pehlke, and M. Scheffler, *GaAs equilibrium crystal shape from first principles*, Phys. Rev. B 54, 8844 (1996)

[229] M. Albani, L. Ghisalberti, R> Begamaschini, M. Friedl, M. Salvalaglio, A. Voigt, F. Montalenti, G. Tütüncüoglu, A. Fontcuberta i Morral, and L. Miglio, *Growth kinetics and morphological analysis of homoepitaxial GaAs fins by theory and experiment*, Physsical Review Materials 2, 093404 (2018)

[230] S. Morkötter, N. Jeon, D. Rudolph, B. Loitsch, D. Spirkoska, E. Hoffmann, M. Döblinger, S. Matich, J. J. Finley, L. J. Lauhon, G. Abstreiter, and G. Koblmüller, *Demonstration of*

Confined Electron Gas and Steep-Slope Behavior in Delta-Doped GaAs-AlGaAs Core-Shell Nanowire Transistors, Nano Lett. 15, 3295-3302 (2015)

[231] Z. Sun, O. Hazut, B. C. Huang, Y. P. Chiu, C. S. Chang, R. Yerushalmi, L. J. Lauhon, and D. N. Seidman, *Dopant Diffusion and Activation in Silicon Nanowires Fabricated by ex Situ Doping: A correlative Study via Atom-Probe Tomoagraphy and Scanning Tunneling Spectroscopy*, Nano Lett. 16, 4490-4500 (2016)

[232] Z. Sun, O. Hazut, R. Yerushalmi, L. J. Lauhon, and D. N. Seidman, *Criteria and considerations for preparing atom-probe tomography specimens of nanomaterials utilizing an encapsulation methodology*, Ultramicroscopy 184, 225-233 (2018)

[233] O. C. Hellman, J. A. Vandenbroucke, J. Rüsing, D. Isheim, and D. N. Seidman, *Analysis of Three-Dimensional Atom-Probe Data by the Proximity Histogram*, Microsc. Micoranal. 6, 437-7444 (2000)

[234] O. Gül, D. J. van Woerkom, I. van Weperen, D. Car, S. R. Plissard, E. P. A. M. Bakkers and L. P. Kouwenhoven, *Towards high mobility InSb nanowire devices*, Nanotechnology 26, 215202 (2015)

[235] J. W. Harrison and J. R. Hauser, *Alloy scattering in ternary III-V compounds*, Phys. Rev. B 13, 5347 (1976)

[236] M. I. D'Yakonov and V. I. Perel, *Spin Orientation of Electrons Associated with the Interband Absorption of Light in Semiconductors*, Sov. Phys. JETP 33, 1053 (1971)

[237] C. W. J. Beenakker and H. van Houten, *Boundary scattering and weak localization of electrons in a magnetic field*, Phys. Rev. B 38, 3232 (1988)

[238] C. Kurdak, A. M. Chang, and T. Y. Chang, *Quantum interference effects and spin-orbit interaction in quasi-one-dimensional wires and rings*, Phys. Rev. B 46, 6846 (1992)

[239] B. Al'tshuler and B Aronov, *Magnetoresistance of thin films and of wires in a longitudinal magnetic field*, JETP Lett. 33, 499 (1981)

[240] I. van Weperen, B. Tarasinski, D. Eeltink, V. S. Pribiag, S. R. Plissard, E. P. A. M. Bakkers, L. P. Kouwenhoven, and M. Wimmer, *Spin-orbit interaction in InSb nanowires*, Phys. Rev. B 91, 201413(R) (2015)

[241] M. J. Carballido, C. Kloeffel, D. M. Zumbühl, and D. Loss, *Low-symmetry nanowire cross-sections for enhanced Dresselhaus spin-orbit interaction*, Phys. Rev. B 103, 195444 (2021)

[242] F. Dettwiler, J. Fu, S. Mack, P. J. Weigele, J. C. Egues, D. D. Awschalom, and D. M. Zumbühl, *Stretchable Persistent Spin Helices in GaAs Quantum Wells*, Phys. Rev. X 7, 031010 (2017)

[243] D. Grundler, *Large Rashba Splitting in InAs Quantum Wells due to Electron Wave Function Penetration into the Barrier Layers*, Phys. Rev. Lett. 84, 6074 (2000)

[244] R. Wang, R. S. Deacon, J. Yao, C. M. Lieber, and K. Ishibashi, *Electrical modulation of weak-antilocalization and spin-orbit interaction in dual gated Ge/Si core/shell nanowires*, Semicond. Sci. Technol. 32, 094002 (2017)

[245] D. B. Suyatin, C. Thelander, M. T. Björk, I. Maximov, and L. Samuelson, *Sulfur passivation for ohmic contact formation to InAs nanowires*, Nanotechnology 18, 105307 (2007)

[246] S. birner, T. Zibold, T. Andlauer, T. Kubis, M. Sabathil, A. Trellakis, and P. Vogl, *nextnano: General Purpose 3-D Simulations*, IEEE Transactions on Electron Devices 54, 2137-2142 (2007)

[247] K. Popper, *Conjectures and Refutations: The Growth of Scientific Knowledge*, London and New York: Basic Books (1962)

[248] A. Kitaev, *Unpaired Majorana fermions in quantum wires*, Phys.-Usp. 44, 131 (2001)

[249] Image taken from Stack Overflow, user *electronpusher*, https://math.stackexchange.com/questions/2258389/how-can-a-mug-and-a-torus-be-equivalent-if-the-mug-is-chiral

[250] V. Mourik, K. Zuo, S. M. Frolov, S. R. Plissard, E. P. A. M. Bakkers, and L. P. Kouwenhoven, *Signatures of Majorana Fermions in Hybrid Superconductor-Semiconductor Nanowire Devices*, Science 336, 1003 (2012)

[251] P. Yu, J. Chen, M. Gomank, G. Badawy, E. P. A. M. Bakkers, K. Zuo, V. Mourik, and S. M. Frolov, *Non-Majorana states yield nearly quantized conductance in proximatized nanowires*, Nature Physics 17, 482-488 (2021)

[252] N. Read and D. Green, *Paired states of fermions in two dimensions with breaking of parity and time-reversal symmetries and the fractional quantum Hall effect*, Phys. Rev. B 61, 10267 (2000)

[253] E. F. Talantsev, K. Iida, T. Ohmura, T. Matsumoto, W. P. Crump, N. M. Strickland, S. C. Wimbush, and H. Ikuta, *p-wave superconductivity in iron-based superconductors*, Scientific Reports 9, 14245 (2019)

[254] F. Nichele, A. C. C. Drachmann, A. M. Whiticar, E. C. T. O'Farrell, H. J. Suominen, A. Fornieri, T. Wang, G. C. Gardner, C. Thomas, A. T. Hatke, P. Krogstrup, M. J. Manfra, K. Flensberg, and C. M. Marcus, *Scaling of Majoran Zero-Bias Conduction Peaks*, Phys. Rev. Lett 119, 136803 (2017)

[255] A. Kitaev, *Unpaired Majorana fermions in quantum wires*, Phys.-Usp. 44, 131 (2001)

[256] J. Alicea, Y. Oreg, G. Refael, F. von Oppen, and M. P. A. Fisher, *Non-Abelian statistics and topological quantum information processing in 1D wire networks*, Nature Physics, 7, 412-417 (2011)

[257] D. I. Pikulin, J. P. Dahlhaus, M. Wimmer, H. Schomerus, and C. W. J. Beenakker, *A zero-voltage conductance peak from weak antilocalization in a Majorana nanowire*, New Journal of Physics 14, 125011 (2012)

[258] S. R. Plissard, I. van Weperen, D. Car, M. A. Verheijen, G. W. G. Imminik, J. Kammhuber, L. J. Cornelissen, D. B. Szombati, A. Geresdi, S. M. Frolov, L. P. Kouwenhoven, and E. P. A. M. Bakkers, *Formation and electronic properties of InSb nanocrosses*, Nature Nanotechnology 8, 859-864 (2013)

[259] H. Schmid, M. Borg, K. Moselund, L. Gignac, C. M. Breslin, J. Bruley, D. Cutaia, and H. Riel *Template-assisted selective epitaxy of III-V nanoscale devices for co-planar heterogeneous integration with Si*, Appl. Phys. Lett. 106, 233101 (2015)

[260] P. Aseev, G. Wang, L. Binci, A. Singh, S. Marti-Sanchez, M. Botifoll, L. J. Stek, A. Bordin, J. D. Watson, F. Boekhout, D. Abel, J. Gample, K. van Hoogdalem, J. Arbiol, L. P. Kouwenhoven, G. de Lange, and P. Caroff, *Ballistic InSb Nanowires and Networks via Metal-Sown Selective Area Growth*, Nano Lett. 19, 9102-9111 (2019)

[261] C. P. Scheller, T. M. Liu, G. Barak, A. Yacoby, L. N. Pfeiffer, K. W. West, and D. M. Zumbühl, *Possible Evidence for Helical Nuclear Spin Order in GaAs Quantum Wires*, Phys. Rev. Lett. 112, 066801 (2014)

[262] T. Patlatiuk, C. P. Scheller, D. Hill, Y. Tserkovnyak, G. Barak, L. N. Pfeiffer, K. W. West, and D. M. Zumbühl, *Evolution of the quantum Hall bulk spectrum into chiral edge states*, Nat. Commun. 9, 3692 (2018)

[263] T. Patlatiuk, C. P. Scheller, D. Hill, Y. Tserkovnyak, J. C. Egues, G. Barak, A. Yacoby, L. N. Pfeiffer, K. W. West, and D. M. Zumbühl, *Edge-State Wave Functions from Momentum-Conserving Tunneling Spectroscopy*, Phys. Rev. Lett. 125, 087701 (2020)

[264] L. C. Camenzind, L. Yu, P. Stano, J. D. Zimmerman, A. C. Gossard, D. Loss, and D. M. Zumbühl, *Hyperfine-phonon spin relaxation in a single-electron GaAs quantum dot*, Nat. Commun. 9, 3454 (2018)

[265] S. Amasha, K. Maclean, I. P. Radu, D. M. Zumbühl, M. A. Kastner, M. P. Hanson, and A. C. Gossard, *Electrical Control of Spin Relaxation in a Quantum Dot*, Phys. Rev. Lett. 100, 046803 (2008)

[266] D. M. Zumbühl, J. B. Miller, C. M. Marcus, K. Campman, and A. C. Gossard, *Spin-Orbit Coupling, Antilocalization, and Parallel Magnetic Fields in Quantum Dots*, Phys. Rev. Lett. 89, 276803 (2002)

[267] F. N. M. Froning, L. C. Camenzind, O. A. H. van der Molen, A. Li, E. P. A. M. Bakkers, D. M. Zumbühl, and F. R. Braakman, *Ultrafast hole spin qubit with gate-tunable spin-orbit switch functionality*, Nat. Nanotechnol. 16, 308-312 (2021)

[268] C. Reeg, D. Loss, and J. Klinovaja, *Metallization of a Rashba wire by a superconducting layer in the strong-proximity regime*, Phys. Rev. B 97, 165425 (2018)

[269] T. Dittrich, P. Hänggi, G. L. Ingold, B. Kramer, G. Schön, and W. Zwerger, *Quantum Transport and Dissipation*, Wiley-VCH (1998)

[270] R. M. Lutchyn, J. D. Sau, and S. Das Sarma, *Majorana fermions and a topological phase transition in semiconductor-superconductor heterostructures*, Phys. Rev. Lett. 105, 077001 (2010)

[271] Y. Oreg, G. Refael, and F. von Oppen, *Helical liquids and Majorana bound states in quantum wires*, Phys. Rev. Lett. 105, 177002 (2010)

[272] J. Schliemann, J. C. Egues, and D. Loss, *Nonballistic Spin-Field-Effect Transistor*, Phys. Rev. Lett. 90, 146801 (2003)

[273] A. Manchon, H. C. Koo, J. Nitta, S. M. Frolov, and R. A. Duine, *New perspectives for Rashba spin-orbit coupling*, Nature Mater. 14, 871-882 (2015)

[274] S. P. Ramanandan, P. Tomic, N. P. Morgen, A. Giunto, A. Rudra, K. Ensslin, T. Ihn, and A. Fontcuberta i Morral, *Coherent Hole Transport in Selective Area Grown Ge Nanowire Networks*, Nano Lett. XXXX, XXX, XXX-XXX (2022)

[275] G. Bergmann, *Weak Anti-localization - An Experimental Proof for the Destructive Interference of Rotated Spin 1/2*, Solid State Communications 42, 815-817 (1982)

[276] H. Rauch, A. Zeilinger, G. Badurek, A. Wilfing, W. Bauspiess, and U. Bonse, *Verification of Coherent Spinor Rotation of Fermions*, Phys. Lett. 54A, 425-427 (1975)

[277] D. C. Marinescu, P. J. Weigele, D. M. Zumbühl, and J. C. Egues, *Closed-Form Weak Localization Magnetoconductivity in Quantum Wells with Arbitrary Rashba and Dresselhaus Spin-Orbit Interactions*, Phys. Rev. Lett. 122, 156601 (2019)

[278] P. J. Weigele, D. C. Marinescu, F. Dettwiler, J. Fu, S. Mack, J. C. Egues, D. D. Awschalom, and D. M. Zumbühl, *Symmetry breaking of the persistent spin helix in quantum transport*, Phys. Rev. B 101, 035414 (2020)

12 Curriculum Vitae

Kristopher Cerveny

Education

2002 - 2008 Bachelor of arts in linguistics and philisophy, State University of New York at Albany, USA

2013 - 2017 Bachelor of science in physics, University of Basel, Switzerland

2017 - 2018 Master of Science in physics, University of Basel, Switzerland

2018 - 2022 PhD in physics, University of Basel, Switzerland

Publications

M. Friedl, K. Cerveny, P. Weigele, G. Tütüncüoglu, S. Marti-Sanchez, C. Huang, T. Patlatiuk, H. Potts, Z. Sun, M. O. Hill, L. Güniat, W. Kim, M. Zamani, V. G. Dubrovskii, J. Arbiol, L. J. Lauhon, D. M. Zumbühl, and A. Fontcuberta i Morral, *Template-Assisted Scalable Nanowire Networks*, Nano Lett. **18**, 2666-2671 (2018)

M. Friedl, K. Cerveny, C. Huang, D. Dede, M. Samani, M. O. Hill, N. Morgan, W. Kim, L. Güniat, J. Segura-Ruiz, L. J. Lauhon, D. M. Zumbühl, and A. Fontcuberta i Morral, *Remote Doping of Scalable Nanowire Branches*, Nano Lett. **20**, 3577-3584 (2020)